Numerical Studies on Control of Flow Around a Circular Cylinder

January 2015

Hiroshi Naito

A Thesis for the Degree of Ph.D. in Engineering

Numerical Studies on Control of Flow Around a Circular Cylinder

January 2015

Graduate School of Science and Technology
Keio University

Hiroshi Naito

要旨

円柱周り流れの制御に関する数値的研究

鈍頭物体周りの流れで生じる種々の問題を解決するため，これまで様々な制御手法が提案され，研究されてきた．しかしこれらの制御手法はそれぞれ使用可能な環境が限定されており，またそのパフォーマンスにも未だ改善の余地が残る．本論文では鈍頭物体として最も単純な形状である円柱を取り扱い，その流れ場に対する以下の二種類の制御に関する数値的研究を行った．特に本論文ではエネルギー散逸に着目をし，受動的制御におけるその役割，および制御効果とエネルギー散逸の間の関係を明らかにした．

一つ目の研究では，直接数値シミュレーション（DNS）およびラージエディシミュレーション（LES）を用いて多孔質体表面適用による円柱周りの流れ場の制御に関する調査を行った．まず予備的調査として，レイノルズ数 Re = 1000 における DNS により空隙率，透過率の最適な組み合わせを求めた．次いでそれらの値を用いて三次元 DNS を行った．また，異なるレイノルズ数および異なる多孔質体厚さにおける数値シミュレーションを行った．その結果，流れ場の三次元性および変動成分は多孔質体により抑制されており，この制御効果は多孔質体が厚く，レイノルズ数が高いほどより顕著になることが分かった．最も効果的であったケースでは渦放出が完全に抑制され，先行研究の実験結果と同様な流れ場が再現された．さらに，多孔質体表面のすべり速度および多孔質体内部でのエネルギー散逸過程が，流れ場の変化のメカニズムに対して重要な役割を担っていることを明らかにした．

二つ目の研究では，このエネルギー散逸による制御機構を踏まえ，円柱周りの流れ場のエネルギー散逸の最小化を目的とした能動制御を二次元 DNS により調査した．まず，理論解析により流体場のエネルギー散逸と円柱壁面上の物理量を関係づける恒等式を導出し，導出した式を評価関数として取り扱い，準最適制御理論を用いたエネルギー散逸抑制のための新たな制御スキームを構築した．制御効果を最適化するため，制御インターバルに関するパラメータスタディを行い，過去に提案された制御スキームとの比較を行った．その結果，レイノルズ数 Re = 100 の場合には既存の準最適制御に対する優位性は見られなかったものの，Re = 1000 の場合にはエネルギー散逸がより抑制されていることが分かった．また，抵抗係数やエネルギー効率においても他の制御スキームに対する優位性を示すことが分かった．さらに得られた制御入力はセンサーを用いないプレデターミンド制御や三次元流れの制御においても高い制御効果を有することが示された．

Abstract
Numerical Studies on Control of Flow Around a Circular Cylinder

In order to solve problems occurring in a flow around a bluff body, various control methods have been proposed and investigated. However, each of those control methods can be used only in limited circumstances, and still leaves room for improvement in performances. This thesis deals with a circular cylinder as simplest bluff body, and describes the following two numerical investigations on control of flow around a circular cylinder. Especially, this thesis focuses on the energy dissipation, and reveals the role of the energy dissipation in a passive control and relationship between the control effect and the energy dissipation.

In the first study, control of a flow around a circular cylinder having a porous surface has been investigated by means of the direct numerical simulation (DNS) and the large eddy simulation (LES). The best set of permeability and porosity is determined by a two-dimensional parametric study at the Reynolds number of $Re = 1000$. Subsequently, the control effects are investigated in detail using a three-dimensional DNS at $Re = 1000$. Numerical simulations at different Reynolds numbers and with different thicknesses of porous surface are also performed. It is found that the porous surface suppresses flow fluctuations near the cylinder and this control effect becomes prominent at higher Reynolds numbers and with thicker porous surfaces. In the most effective case, the vortex shedding is completely suppressed and the flow field is found to be similar to that in a previous experimental study. Moreover, the slip velocity on the porous surface and the energy dissipation process inside the porous media are found to play an important role for the flow modifications.

In the second study, taking into account this control mechanism by the energy dissipation, a control minimizing the energy dissipation in a flow around a circular cylinder has been examined using a two-dimensional DNS. First, a relationship between the energy dissipation in the domain and a quantities defined on the cylinder surface is derived. By implementing the derived relationship into the cost function, the energy dissipation is minimized using the suboptimal control theory. In order to maximize the control performance, parametric studies on the control time interval is performed and the best control results are compared with previously proposed suboptimal controls. Although the present scheme does not improve the control performance at $Re = 100$, but shows a better performance in the energy dissipation at $Re = 1000$. It is also found that the present control shows a greater amount of drag reduction with a better energy efficiency. Furthermore, the obtained control input shows better control effects when it is applied to a predetermined control without sensors and the control of a three-dimensional flow.

Acknowledgments

Without the support of many people this thesis would not have been possible.

I would like to express my deepest appreciation to my wonderful supervisor, Professor Koji Fukagata. Owing to his exact comments, tender tutorials and warm encouragement, I could have the most amazing 7 years in my life. Professor Shinnosuke Obi gives various help concerning not only research but also my student life and job as an assistant. I would like to express my gratitude to his generosity. Professor Akiko Matsuo is also gratefully acknowledged for her helpful comments. Constructive advice given by Professor Hiromichi Kobayashi is also beneficial for my research. I also thank Dr. Keita Ando who gives insightful suggestions and kind support for my job.

The investigation of control using porous media is motivated by the experimental study by the group of Railway Technical Research Institute. I especially thank Dr. Takehisa Takaishi for giving valuable information.

I had great experiences through working as an assistant at Keio university. Especially, the time shared with Professor Kenji Yasuoka, Professor Naomichi Ogihara and Professor Kenjiro Takemura is invaluable.

I enjoyed a happy student life with the members of Obi·Fukagata·Ando laboratory. Particularly, I appreciate Kazutaka Nakayama, Yosuke Anzai, Yuki makihahra, and Dr. Simon J. Illingworth who have shared time in the same research group.

Financial support from Keio University Global COE program "Center for Education and Research of Symbiotic, Safe and Secure System Design" is gratefully acknowledged.

Also, I would like to thank my parents for their encouragement.

January 2015

Contents

List of Figures

List of Tables

Nomenclature

Symbol	description
a, b	Ergen numbers
C_D	drag coefficient
C_f	friction coefficient
C_L	lift coefficient
C'_L	root mean square of lift coefficient
C_p	pressure coefficient
D	cylinder diameter
d	thickness of porous surface
Da	Darcy number
d_p	particle diameter assumed inside porous media
$\mathbf{e_x}$	basis vector in stream wise direction
$\boldsymbol{F}$	force acting on a cylinder
F_{DF}	frictional force acting on cylinder
F_{DP}	pressure force acting on cylinder
J_1	cost function given by pressure drag
J_2	cost function given by difference between actual pressure and target pressure
$\boldsymbol{K}$	frictional force inside porous media
k	permeability
$K_{\|k\|}$	$\|k\|$-th order modified Bessel function of the second kind
$\mathbf{n}$	unit normal vector
N_r	number of grid point in radial direction
N_z	number of grid point in spanwise direction
N_θ	number of grid point in circumferential direction
p	pressure
$< \boldsymbol{p} >$	macroscopic pressure inside porous media
p_t	total pressure
q_i	Fréchet differentials of velocity components
R	cylinder radial
Re	Reynolds number
$\mathbf{s}$	strain rate tensor
$\mathbf{s}'$	strain-rate tensor composed by deviation velocity
St	Strouhal number
T	time scale of flow field
t	nondimensional time

$\boldsymbol{u}$, $\mathbf{u}$	velocity vector
$< \boldsymbol{u} >$	macroscopic velocity inside porous media
u_r	velocity component in radial direction
$\mathbf{u_s}$	velocity vector on the surface
$\mathbf{u}'$	deviation velocity vector
u_θ	velocity component in circumferential direction
U_∞	uniform velocity
V	domain under consideration
W_a	upper bound of actuation power
W_{id}	ideal lowest actuation power
γ_a	lower bound of energy efficiency
γ_{id}	ideal highest energy efficiency
Δ_{min}	minimum grid width in radial direction
Δt	time interval of computation
Δt_c	control interval
ϵ	energy dissipation in flow field
η_i	function consisting q_i in Fourier space
ν	kinematic viscosity
ν_t	turbulent viscosity assumed in sub grid scale component
Π	function consisting ψ in Fourier space
ρ	descent parameter for minimization
ϕ	porosity
ϕ_c	control input
$\phi_{c_{max}}$	control amplitude
ψ	Fréchet differentials of pressure
Ω	volume of porous media
ω_x	streamwise vorticity
ω_z	spanwise vorticity
∂V_1	cylinder surface
∂V_2	external boundary
$\partial \Omega$	porous surface
$\frac{\mathscr{D}f}{\mathscr{D}\phi}$	Fréchet differential of a function f

Chapter 1

Introduction

1.1 Flow control around a circular cylinder

Blunt shaped instruments or obstacles, such as automobiles, buildings and tubes of heat exchangers are present everywhere. These instruments and obstacles play various roles in our life. In many cases, they are forced by fluids or they make use of fluids energy.

Fluid flows are disturbed by the presence of a bluff body. When the Reynolds number is sufficiently small, the flow is kept as a steady creep flow. However, when the Reynolds number exceeds the critical value, the boundary layer begins to separate, and the vortex shedding occurs. In such complex flow states, the fluids lose a significant amount of energy due to the viscous energy dissipation, which makes large pressure gap between the upstream surface and the downstream surface; thus a huge drag acts on the body. Also, the unsteadiness and the dissymmetry of the flow fields yield force fluctuations and aerodynamic noise.

These characteristics produce critical problems on the aspects of performance and safety of instruments. Taking a high-speed train for instance, a large drag prevents further speed-up and energy savings, and the huge force fluctuation would spoil stability performance and possibly yield breakage of the instruments in the worst case. Also, the aerodynamic noise induced from the high-speed train has been one of the biggest issues in the environmental aspect for a few decades.

Although there are many ways to solve or mitigate flow-induced problems, control of fluid flow is the most direct way. Recent progresses in numerical simulations, technologies of micro-electrical-mechanical systems (MEMS) and control theories have led growing interests in flow controls. The targets of flow control fall into internal flows and external flows. While controls of internal flows, such as flows inside a channel and a pipe, generally aim to reduce the frictional drag (Kasagi *et al.* 2009, Kim & Bewley 2007), controls of external flows are further divided into controls of a spatial developing boundary layer (e.g., Kametani & Fukagata 2011, 2012), which also aim at reduction of frictional drag, and controls of flow around an object. In particular, controls of flow around a bluff body have been paid much attention due to their great environmental impact.

Various control methods of flow around a bluff body have been investigated as summarized in Fig. 1.1 (Choi *et al.* 2008). Control methods are mainly classified into passive controls and active controls. Passive controls are feasible, since sensing and actuation are not required. Representative controls are a splitter plate behind an object (Roshko 1955, Bearman 1965, Anderson & Szewczyk 1997, Hwang *et al.* 2003, Kwon & Choi 1996, Ozono 1999), a small secondary cylinder (Dalton *et al.* 2003, Sakamoto & Haniu 1994, Strykowski & Screenivasan 1990, Tang & Aubry 2000), some geometric modifications such as rough surface (Shih *et al.* 1993), dimples (Bearman & Harvey 1993), spiral lines (Lee & Kim 1997, Zdravkovich 1981), trailing edge segmentations (Tanner 1972, Rodriguez 1991, Petrusma & Gai 1994), and wavy geometries (Tombazis & barman 1997, Bearman & Owen 1998), to name a few. Although passive controls are feasible, the adaptability in variating circumstances and the control effects are often inferior to those of active controls.

Active controls require actuation, and these controls are again classified into two categories: open-loop controls, which do not require sensing, and closed-loop (feedback) control, which require sensing. Owing to large control effects and feasibility of open-loop controls, a number of studies have been conducted using, e.g., rotating surface (Baek & Sung 1998, Choi *et al.* 2002, Dennis *et al.* 2000, Filler *et al.* 1991, Poncet 2002, 2004, Shiels & Leonard 2001, Tokumaru & Dimotakis 1991), oscillations (Konstantinidis *et al.* 2005, Nehari *et al.* 2004) and blowing/suction (Arcas & Redekopp 2004, Delaunay & Kaiktsis 2001, Leu & Ho 2000, Lin *et al.* 1995, Sevilla & Martinez-Bazán 2004, Yao & Sandham 2002, Fujisawa *et al.* 2004, Jeon *et al.* 2004, Lin *et al.* 1995, Williams *et al.* 1992). Open-loop controls basically have better control effects than passive controls, but energy efficiency is inferior to that of feedback controls.

Feedback controls are of great interest because of their adaptability and high energy performance. There are many successful controls such as the linear feedback control with a single sensor (Berger 1967, Ffowcs Williams & Zhao 1989, Roussopoulos 1993, Park *et al.* 1994, Huang 1996, Zhang *et al.* 2004), optimal controls (He *et al.* 2000, Protas & Styczek 2002), suboptimal controls (Min & Choi 1999, Jeon & Choi 2010), controls using a reduced order model (Gilles 1998, Graham *et al.* 1999, Bergmann *et al.* 2005, Siegel *et al.* 2006) and controls based on inviscid models (Li & Aubry 2003, Protas 2004).

These three categories have advantages and disadvantages respectively, and an individual control belonging to each category has limited control performance and limited situational adaptability. The splitter plate, for instance, prevents vortex interaction by placing in the wake, and eliminates vortex shedding. This control method works effectively even at higher Reynolds numbers if a sufficiently long plate is used. Such a long plate, however, can not be placed in any configurational circumstances, and this control method depends on the main stream direction. Another intelligible example is the linear feedback control using single sensor. This control scheme achieves complete suppression of vortex shedding at quite low Reynolds numbers, but this control has not yet led to complete suppression at higher Reynolds numbers due to difficulty to capture the complex flow features. Thus, each of control method can be used only in limited circumstances, and still leaves room for improvement of the performances. Therefore, further investigations of flow control are still required to adjust to various situations and objectives, and to improve control performances.

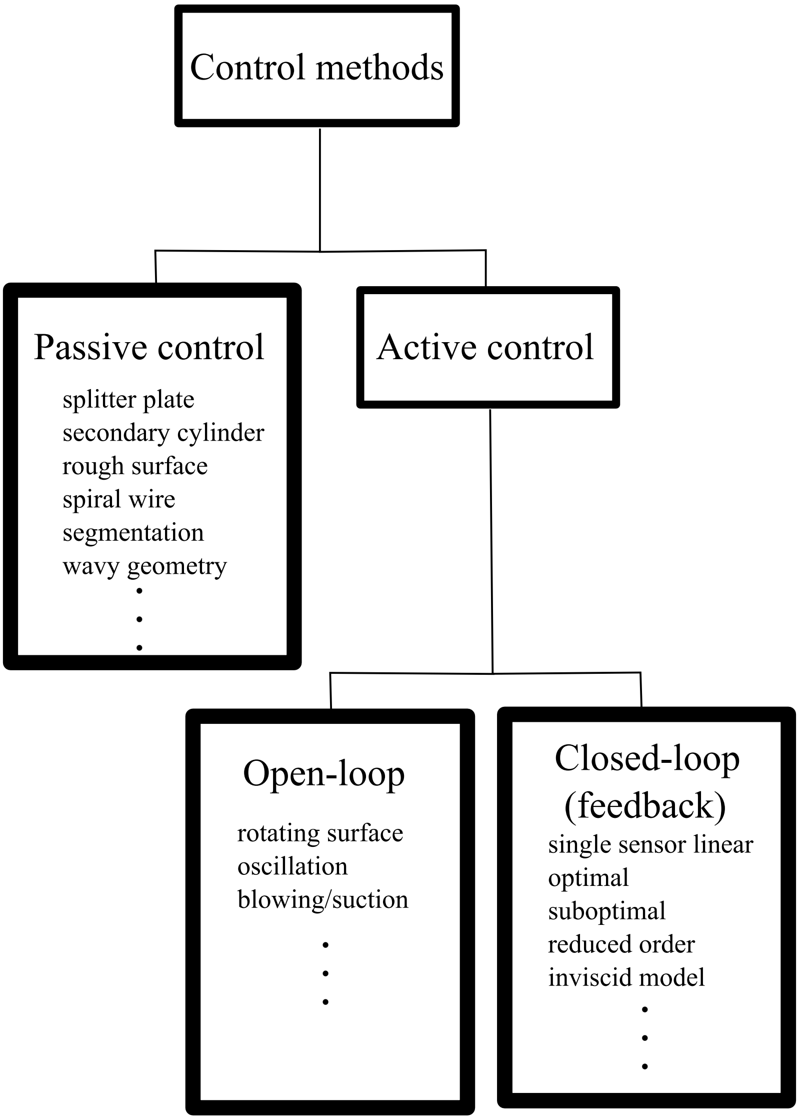

Fig 1.1: Classification of control methods .

1.2 Porous media as a control device

Recently, Sueki *et al.* (2010) studied the control effect of porous media on the flow around a circular cylinder aiming at noise reduction of the pantograph used for bullet trains. They achieved significant noise reduction in their wind tunnel experiment. The PIV measurement at $Re = 1.3 \times 10^5$ reveals that the shear layer above the porous surface can completely be stabilized. Although the mechanism of flow stabilization is not always clear, their results at least suggest that the porous media is an effective passive control device for suppression of vortex shedding.

Porous media has some advantages as a control device. First, since this control method is within passive control category, actuators and sensors are not required. Second, the means of installation is simply to surround the porous media around controlled objects, and hence its installation to real applications is relatively easy. Third, while some of control methods suppressing vortex shedding require wide configuration spaces (e.g., splitter plate and secondary cylinder), the configuration space for this control is localized just adjacent to the controlled objects. Also, as invoked from its two-dimensionally isotropic configuration, this control does not have directional priority. Furthermore, this control is effective even for higher Reynolds number flows (at least effective up to $Re = 1.3 \times 10^5$ as shown in the experimental results).

These advantages suggest practical usability and requirement of further investigation. Toward the use of porous media in industrial applications, one should further accumulate the knowledge about its effect on the flow, including the dependency to various design parameters and the detailed mechanism of flow modification. This thesis focuses on porous media as a control device, and documents comprehensive results given by numerical simulation and some consideration. Detailed background of control by porous surface is shown in Chap. 3.

1.3 Flow control in an energy aspect

As already mentioned, active feedback controls have some advantages in return for difficulty of installation of sensors and actuators. Since control algorithm is determined arbitrarily, an user can give suitable control input depending on control objectives, and hence control efficiency is basically better than open-loop controls. Although rapid progresses in MEMS technologies have accelerated practical implementation of control hardwares, how feedback control algorithm should be constructed is still a disputable problem for flow control.

Most of studies on feedback control laws have been devoted for two main categories. The first category is empirically and intuitively derived laws, and another category is controls focused on instability. A good example is control law used in Park *et al.* (1994). They introduced a simple feedback law whose input (blowing and suction on the local surface of a circular cylinder) is given proportional to a velocity at local downstream point. In some cases, this control achieves suppression of vortex shedding, and thereby drag reduction is obtained. However complete suppression is attained only at quite lower Reynolds number, $Re = 60$ (just adjacent to the critical Reynolds number). At higher Reynolds number, the control cannot capture complex fluid features and therefore complete suppression is no longer achieved. Similar to this example, the laws in this category have advantage of simplicity, while have disadvantage of poor robustness.

The category focused on instability of fluid is more systematic way of control. This category includes not only laws based on instability theory but also laws based on systemized fluid flow. Controls in this category merely aim at 'stabilization' of systems. As past studies revealed, 'stabilization' leads drag reduction, suppression of lift force fluctuation as well as noise reduction, therefore these controls are worth it. However, resultant control effects are somehow posteriori and vague. Generally speaking, objectives of control are more physical requirements (drag reduction, suppression of lift fluctuation and noise reduction are only a few examples among various control objectives), thus control algorithm should directly treat physical properties of fluids.

Investigation of feedback control is motivated not only by how better control effects are obtained, but also by how the results can be utilized for open-loop controls and passive controls. This argument and above two paragraphs imply requirement of new systematic law and new physical visions for flow control. With this motivation, this thesis treats an active feedback control, which is mathematically solid and gives a new physical vision.

As will be shown in the results of control by porous surface (Chap.3), the energy dissipation of fluid in the wake of the cylinder is suppressed by augmenting the energy dissipation inside the porous media . It was also found that the fluctuation of flow field, thus aerodynamic noise, are mitigated by this energy mechanism. Motivated by this energy aspect, this thesis attempts a control from an energy perspective. Relevant studies and detailed background are documented in the beginning of Chap. 4.

1.4 Target of control

Our final goal is to apply control methods to general industrial applications. However, since newly invented control methods are not always effective for any obstacles, we need to investigate the detailed effects and the mechanism by more simple cases. Among infinite number of geometry variations being categorized in a bluff body, a circular cylinder has been paid great interest because it has a simple geometry and some important flow features as a bluff body such as stagnation points, transition of boundary layers, separations and vortex shedding. This thesis also treats a circular cylinder as the target of control. Although it is almost impossible to directly apply the same control method attempted in this thesis to general industrial applications, results are investigated not only macroscopically but also in detail with the practical intention: not only macroscopic quantity such as drag and lift but also other detailed flow modification such as shift of separation points, instantaneous flow structure modification and its mechanism are investigated. One of the contributions of this thesis is to give some general knowledge for general cases by providing the details of the controlled results.

1.5 Objectives and organization

The objectives of this thesis are summarized as follows.

- To investigate the effects and its mechanism of porous surface by numerical simulations.
- To construct an energy based feedback control law and investigate its effects by numerical simulations.
- To give general knowledges for more complex applications by focusing on the flow fields in detail throughout both studies.

First, the flow around a circular cylinder having a porous surface is investigated by means of direct numerical simulation (DNS) and large eddy simulation (LES). A parametric test for two-dimensional (2D) flow at the Reynolds number of $Re = 1000$ is performed as the first step. Subsequently, three-dimensional (3D) DNS is conducted at $Re = 1000$ and details of flow modification are analyzed. Furthermore, numerical simulations are performed also at different Reynolds numbers, $Re = 100$ (2D), 3900 (LES), and 1.0×10^5 (LES) in order to investigate the Reynolds number dependency. The mechanism of flow modification is clarified by focusing on the energy dissipation process.

Taking into account the results obtained in the study of control porous media, reduction of the energy dissipation in a flow around a circular cylinder is attempted using suboptimal control theory. Since the energy dissipation rate is a quantity defined as a volume integral, it cannot directly be measured by sensors placed on the cylinder surface; namely, the energy dissipation rate itself cannot be used as the cost function to be minimized. Therefore, the mathematical relationship (i.e., identity) between the energy dissipation in an infinitely large volume and the surface quantities is firstly derived, so that the cost function can be expressed by the surface quantities only. Using the identity derived, the control law minimizing the cost function is derived following the suboptimal control procedure of Min & Choi (1999). The performance of the present suboptimal control is evaluated by two-dimensional numerical simulations of flows around a circular cylinder. The performance of a predetermined (i.e., open-loop) control and the the localized predetermined control are also examined using the control input profile obtained by the suboptimal control to examine the possibility toward its practical implementation. Furthermore, the dependency on control amplitude and effects in three-dimensional flow are also investigated.

This thesis is outlined as follows. Details of the numerical models and computational procedures used are presented in Chapter 2. Chapter 3 describes the investigation of flow around a circular cylinder controlled by porous surface. Chapter 4 presents the details of the feedback control focused on the energy dissipation. Finally, concluding remarks are derived in Chapter 5.

Chapter 2

Numerical procedure

2.1 Numerical models

Throughout this thesis, flow around a circular cylinder will be mainly focused on as control target. We assume a circular cylinder is at rest in uniform flow as simplistically depicted in Fig. (2.1).

The governing equations are the incompressible Navier-Stokes equations

$$\frac{\partial \boldsymbol{u}}{\partial t} + \nabla \cdot (\boldsymbol{u}\boldsymbol{u}) = -\nabla p + \frac{1}{Re}\nabla^2 \boldsymbol{u}. \tag{2.1}$$

and the continuity equation

$$\nabla \cdot \boldsymbol{u} = 0\,, \tag{2.2}$$

where all the variables are made dimensionless by the uniform velocity U_∞ and the cylinder diameter D. The Reynolds number Re is defined using kinematic viscosity ν as

$$Re = \frac{U_\infty D}{\nu}. \tag{2.3}$$

This thesis covers four different Reynolds numbers to investigate dependency of control to confirm validity of numerical model (Chap. 3) and investigate dependency of control on the Reynolds number (Chap. 3 and Chap. 4): two-dimensional laminar state case, $Re = 100$, and transitional state cases, in which boundary layer is two-dimensional and shear layer is three-dimensional, $Re = 1000, 3900$ and 1.0×10^5. DNS may always be the best choice if the computer resource allows. For the present purpose, however, DNS at higher Reynolds numbers is disproportionately heavy. Therefore, we adopted LES at higher Reynolds numbers: Dynamic Smagorinsky Model (DSM) (Germano 1991) at Re = 3900, and Constant Smagorinsky Model (CSM) (Smagorinsky 1963) at $Re = 1.0 \times 10^5$. Although the better choice of SGS model may be DSM, CSM is used at $Re = 1.0 \times 10^5$ in order to save the computational cost by considering the finding by Breuer (2000) that the superiority of DSM over CSM is not clear at $Re \simeq 10^5$.

The simulation code is based on the DNS code for a turbulent pipe flow of Fukagata and Kasagi (2002) and adapted here to the flow around a cylinder. For low Reynolds number cases (Re = 100, 1000, and 3900), the energy-conservative finite difference method on the cylindrical coordinate system is used for the spatial discretization. In the highest Reynolds number case ($Re = 1.0 \times 10^5$), however, the QUICK scheme (Leonard 1979) is used for the advection term to avoid artificial transition due to dispersion error. As for temporal integration, the low-storage third order Runge-Kutta/Crank-Nicolson (RK3/CN) scheme (Spalart *et al.* 1991) is used with a higher-order fractional step method for the velocity-pressure coupling (Dukowicz & Dvinsky 1992). The pressure Poisson equation is solved by using the Fast Fourier Transform (FFT) in the azimuthal (θ) and axial (z) directions and the tridiagonal matrix algorithm (TDMA) in the radial (r) direction. A uniform velocity, U_∞, is imposed at the inlet boundary ($0 \le |\theta| \le \frac{3}{4}\pi$), and the convective velocity condition is used at the outlet boundary ($\frac{3}{4}\pi \le |\theta| \le \pi$).

The present simulations use a staggered grid system. Velocities are computed on the cylinder surface and pressure is computed at center of cell Fig. 2.2(a), while the diagonal components of the strain rate tensor are defined at the cell center and the non-diagonal components are defined at the corners. The number of computational cells used is shown in Table 2.1. The size of computational domain, the size of computational cells, and the Kolmogorov length scale computed from the obtained velocity fields are summarized in Table 2.2. Although at Re = 1000 (DNS) the spanwise cell size is about 8 times larger than the Kolmogolov scale, we have confirmed that the cell size is sufficiently small to reproduce the statistics we focus on here: for instance, change in the mean drag coefficient $\overline{C_D}$ in the solid case was less than 1% when Δz was reduced to half. The grid geometry in the solid case at $Re = 100$ and 1000 is shown in Fig. 2.3. Figure 2.3(a) represents whole computational domain, and Fig. 2.3(b) shows its zoom up view near the cylinder.

The present simulation is validated by comparing the major mean flow properties with the literature (Henderson 1995, Norberg 2003, Norberg 2001, Williamson & Roshko 1990, Henderson & Karniadakis 1995, Gerrard 1965, Kravchenko & Moin 2000, Norberg 1987a, Schewe 1983). The time averaged drag coefficient $\overline{C_D}$, the root-mean-square (RMS) of lift coefficient C'_L, the Strouhal number St, and the base pressure C_{pb} are compared in Table 2.3. The present results at $Re = 100 - 3900$ are in fair agreement with the literature. One can notice that numerical simulations (Henderson (1995) and Henderson & Karniadakis (1995) at $Re = 1000$, Kravchenko and Moin (2000) at $Re = 3900$, and the present one), tend to give larger values of $-C_{pb}$ than those in experiments (Williamson & Roshko (1990) and Gerrard (1965) at $Re = 1000$, Williamson & Roshko (1990) and Norberg (1987b) at $Re = 3900$), which are consistent among different experiments. Although totally unclear, this difference may be due to tiny imperfections still remaining in numerical simulations (e.g., grid resolution or computational domain size), that in experiments (e.g., free-stream turbulence or surface roughness), or both. At $Re = 1.0 \times 10^5$, the Strouhal number St is in good agreement with the literature, but difference amounts to about 20% in $\overline{C_D}$, C'_L and C_{pb}. A possible reason for this difference is overestimation of the subgrid scale dissipation in the present LES. The detailed mathematical description is shown in Appendix.

Table 2.1: Number of computational cells used in the present simulations.

Reynolds number (method)	$N_r \times N_\theta \times N_z$
$Re = 100$ (2D)	$220 \times 256 \times 1$
$Re = 1000$ (3D, DNS)	$220 \times 256 \times 64$
$Re = 3900$ (LES)	$200 \times 256 \times 64$
$Re = 1.0 \times 10^5$ (LES)	$300 \times 512 \times 64$

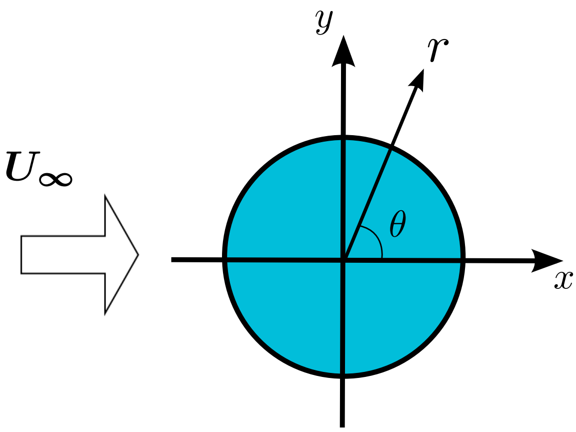

Fig 2.1: Flow around a circular cylinder.

(a)

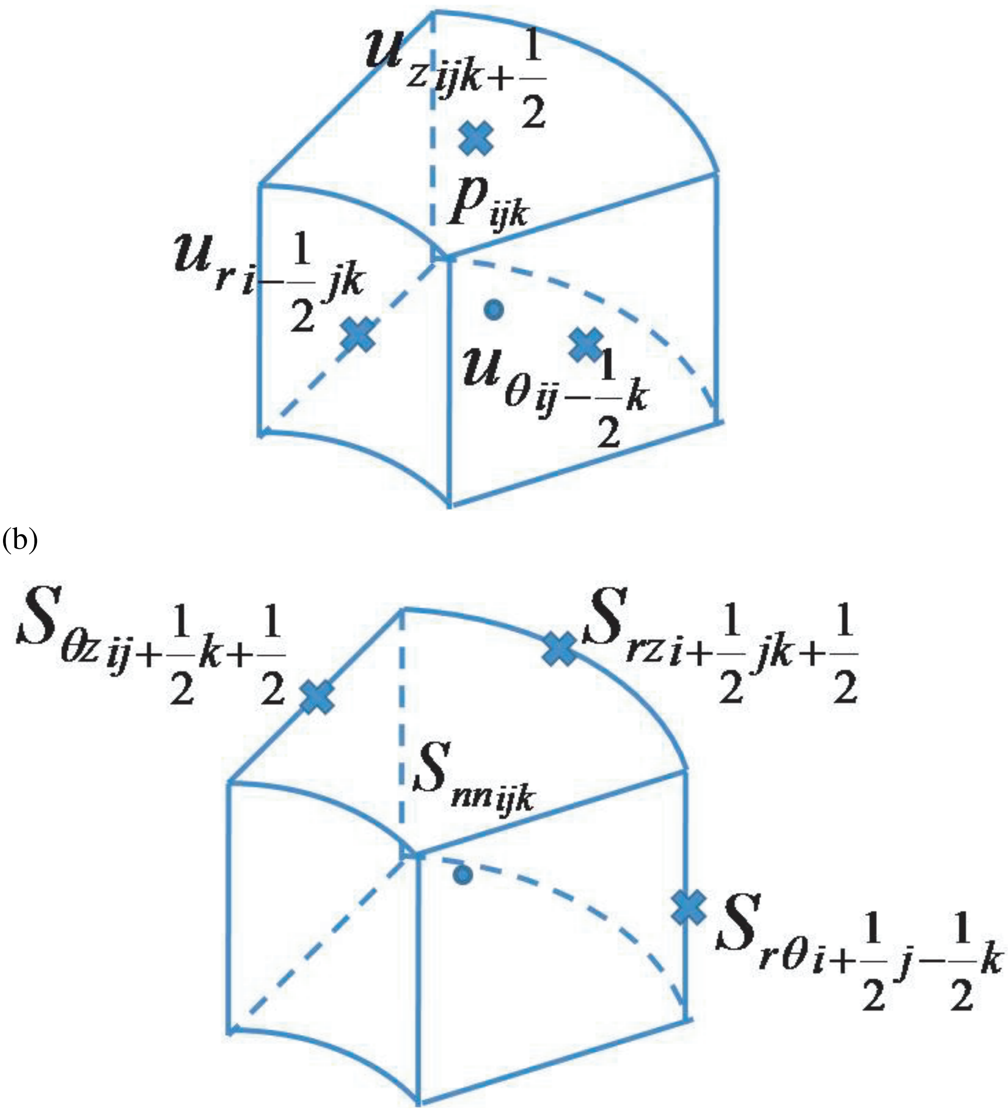

Fig 2.2: Definition point of each variable : (a) velocity and pressure; (b) strain rate tensor.

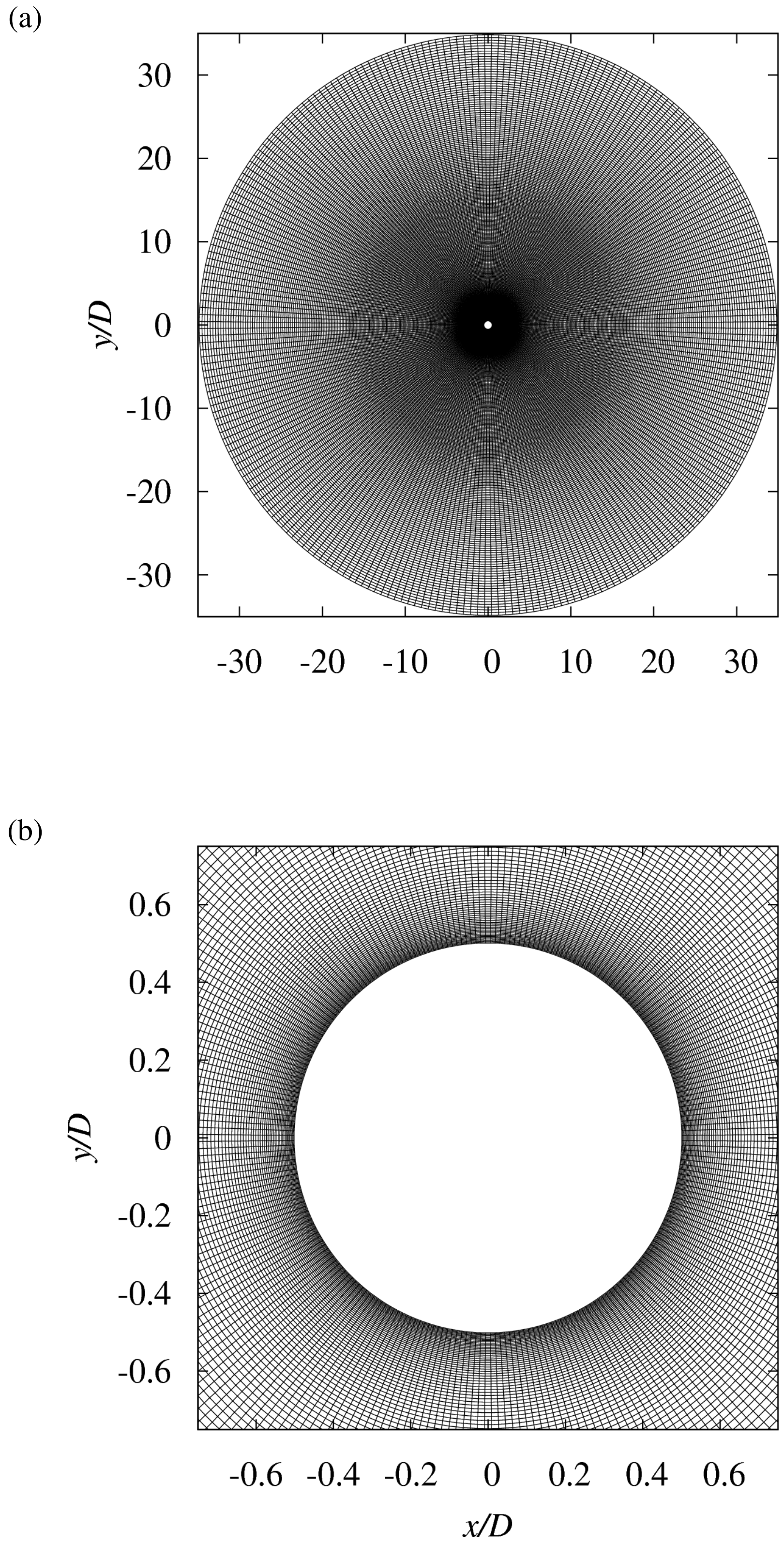

Fig 2.3: Grid geometry (solid surface case at Re = 100 and 1000): (a) whole region; (b) near the cylinder.

Table 2.2: Computational conditions.

Reynolds number (method)	L_r/D	L_z/D	$\Delta r_{min}/D$	$\Delta z/D$	r_{i+1}/r_i	η_k/D
Re = 100 (2D)	35	–	1.0×10^{-2}	–	1.019	–
Re = 1000 (3D, DNS)	35	2π	1.0×10^{-2}	1.0×10^{-1}	1.019	1.27×10^{-2}
Re = 3900 (LES)	15	π	1.5×10^{-3}	5.0×10^{-2}	1.029	2.88×10^{-3}
$Re = 1.0 \times 10^5$ (LES)	15	2	5.0×10^{-4}	3.0×10^{-2}	1.022	3.24×10^{-4}

Table 2.3: Computed flow properties.

	$\overline{C_D}$	C_L'	S_t	$-C_{pb}$
Re = 100				
Present	1.33	0.23	0.165	0.72
Reference	1.34^a	0.23^b	0.165^c	$0.74^{a,d}$
Re = 1000				
Present (3D)	1.09	0.21	0.21	0.92
Reference	1.20^e, 1.52^a	$0.21^{c,e}$	0.21^c	0.75^f, 0.81^d, 1.12^e, 1.69^a
Re = 3900				
Present	1.07	0.25	0.21	1.02
Reference	1.04^g	0.27^h	$0.21^{c,g}$	0.80^f, 0.87^i, 0.94^g
$Re = 1.0 \times 10^5$				
Present	1.46	0.99	0.183	1.73
Reference	1.21^j	0.29^j, 0.73^k	0.185^c, $0.20^{j,k}$	1.35^i, 1.57^k

a: Henderson (1995) b: Norberg (2003) c: Norberg (2001)
d: Williamson & Roshko (1990) e: Henderson & Karniadakis (1995) f: Gerrard (1965)
g: Kravchenko & Moin (2000) h: Kim & Choi (2005) i: Norberg (1987a)
j: Schewe (1983) k: Norberg (1987b)

Chapter 3

Passive control using porous media

3.1 Previous numerical studies

Before proceeding to the central parts, some of the previous numerical studies related to control by porous media should be introduced so that necessity of this work is embossed.

Bruneau & Mortazavi (2004) investigated the effect of porous media on flows around a square cylinder by means of two-dimensional numerical simulation. The Reynolds number was $Re = 3000$ and 30000. They assumed that the top and bottom layers of the square cylinder were made of porous material. It was found that the drag, the lift fluctuation, and the global enstrophy were reduced as compared to the case of solid cylinder.

Bruneau & Mortazavi (2006) also studied the effect of porous media on flows around a circular cylinder at the same Reynolds numbers, i.e., $Re = 3000$ and 30000. They assumed porous media of a uniform thickness around a circular cylinder and obtained reduction of lift force fluctuations and global enstrophy. Their computation, however, is two-dimensional despite that three-dimensionality should be taken into account at such high Reynolds numbers. In fact, the Reynolds number assumed in Bruneau and Mortazavi ($Re = 30000$) is relatively close to that in Sueki's experiment ($Re = 10^5$), but the resultant flow modification observed in these two are quite different. Thus, it is necessary to revisit this flow by properly taking into account the three-dimensionality effects.

This study is a comprehensive study rather than a supplemental one, which covers these lacked parts. The key mechanism of the flow modification will be revealed by extensively conducting numerical simulation and intensively analyzing the obtained data

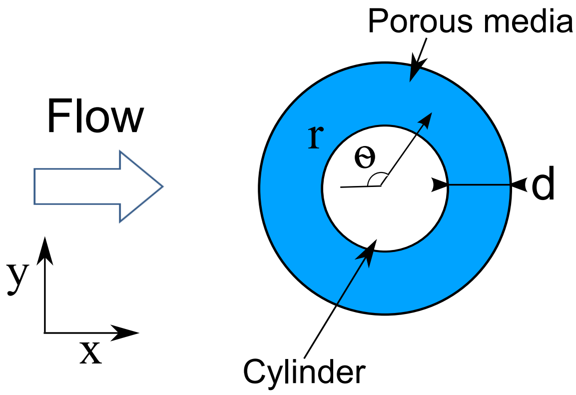

Fig 3.1: Flow configuration.

as shown in the following sections.

3.2 Macroscopic model for porous surface

We assume a circular cylinder in a uniform flow, as shown in Fig. 3.1. The cylinder is assumed to have a porous surface of uniform thickness and uniform permeability.

Various methods have been proposed for the computation of flow in porous media:

1. direct method, in which every complex geometry of porous media is resolved (Martys & Chen (1996));

2. method of boundary condition, which uses an artificial boundary condition mimicking the effect of porous surface (Jiménez *et al.* 2001);

3. macroscopic flow model, which uses a volume-averaged equation in the porous media (Bruneau & Mortazavi 2004, 2006).

The first method is considered most accurate, but not suited for examining the effects of various parameters on the flow due to its relatively high computational cost. The second method cannot be used in the present study since the relationship between the boundary condition and the flow information outside the porous layer is unknown. Therefore, the last method is adopted in the present study.

In contrast to the Brinkman-Navier-Stokes equation used by Bruneau and Mortazavi (2004, 2006), we use the macroscopic momentum equation by Hsu and Cheng (1990), i.e.,

$$\frac{\partial \langle \boldsymbol{u} \rangle}{\partial t} + \nabla \cdot \left(\frac{\langle \boldsymbol{u} \rangle \langle \boldsymbol{u} \rangle}{\phi} \right) = -\nabla \langle p \rangle + \frac{1}{Re} \nabla^2 \langle \boldsymbol{u} \rangle + \boldsymbol{K} \,, \tag{3.1}$$

where $\langle \cdot \rangle$ denotes the macroscopic velocity inside the porous media and $\boldsymbol{K}$ is the internal frictional drag given by

$$\boldsymbol{K} = -\frac{\phi}{ReDa} \langle \boldsymbol{u} \rangle - \frac{b}{\sqrt{a}} \frac{1}{\sqrt{Da}} \frac{\langle \boldsymbol{u} \rangle \, | \langle \boldsymbol{u} \rangle \, |}{\sqrt{\phi}} \,. \tag{3.2}$$

Equation (3.1) is derived under the assumption that the porous media is made of mono-dispersed spheric particles. With this assumption, the frictional force inside the porous media is modeled by accounting for Oseen's correction. The Darcy number $Da = k/D^2$ is the permeability k made dimensionless by using the cylinder diameter D. The permeability is related to the porosity ϕ and the particle diameter d_p by

$$k = \frac{\phi^3 d_p^2}{a(1-\phi)^2} \,, \tag{3.3}$$

where a and b are the Ergun constants. Although these constants vary slightly with porosity and structure of porous media, we assume these values to be $a = 150$ and $b = 1.75$ as obtained by Ergun (1952).

The Brinkman-Navier-Stokes equation used in the previous studies (Bruneau & Mortazavi 2004, 2006) is a classical model: the shear structure inside the porous media is neglected. In contrast, the model used in the present study includes such effect in its derivation.

In order to verify the validity of the present porous model, pressure coefficients on the external surface are compared with the experiments of Sueki *et al.* (2010) in fig. 3.2. The Reynolds numbers for the solid surface case and the porous surface case are $Re = 9.2 \times 10^4$ and $Re = 1.3 \times 10^5$, respectively. The thickness of the porous surface is 29% of whole cylinder radius. In the comparison between the solid case and the porous case of experiments, the pressure distribution is increased and smoothed by the porous surface. This effect is clearly observed in the present simulation results. At the front

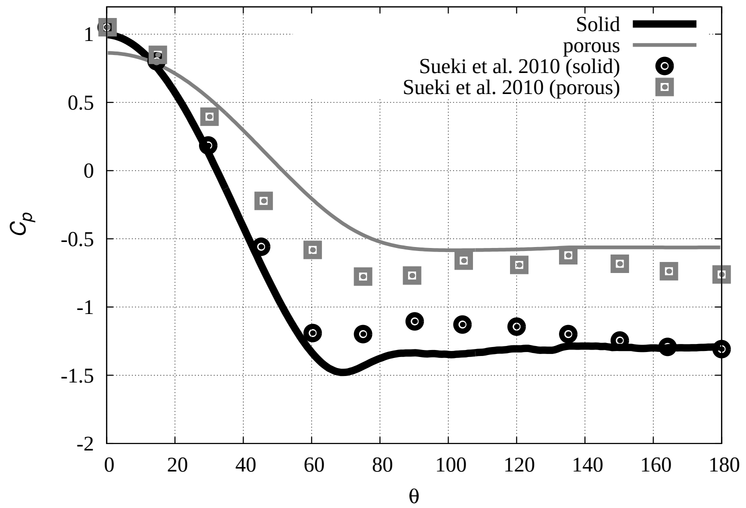

Fig 3.2: Comparison with the experiment of Sueki *et al.* , $Re = 9.2 \times 10^4$ for solid surface and $Re = 1.3 \times 10^5$ for porous surface.

stagnation point, the pressure coefficients of the experiments shows 1, while that of the present simulation shows a little smaller than 1. This is considered due to the zero velocity on the static pressure probe installed in the experiments. Given the difference between the solid cases of the experiment and the present simulation, the present porous model is considered to realize the modification appropriately.

Throughout the present study, the surrounding porous media are assumed to have uniform thickness d, permeability k, and porosity ϕ. Two different thicknesses are considered: 20% and 50% of the cylinder radius (i.e., $d = 0.2R$ and $d = 0.5R$).

Table 3.1 shows the number of grid of the simulations of the porous surface cases. The number in the radial direction is increased in the porous cases simply because the resolution in the pure fluid region is kept constant and the grid is extended inside the porous region.

3.3 Parametric study

In order to find the effective porous properties the parametric study is performed. According to Eqs. (3.1)–(3.3), two out of three parameters, i.e., ϕ, k (or Da), and d_p, are

Table 3.1: Number of computational cells of porous surface cases.

Reynolds number (method)	Surface	$N_r \times N_\theta \times N_z$
Re = 100 (2D)	Solid	$220 \times 256 \times 1$
	Porous $d = 0.2R$	$230 \times 256 \times 1$
	Porous $d = 0.5R$	$245 \times 256 \times 1$
Re = 1000 (3D, DNS)	Solid	$220 \times 256 \times 64$
	Porous $d = 0.2R$	$230 \times 256 \times 64$
	Porous $d = 0.5R$	$245 \times 256 \times 64$
Re = 3900 (LES)	Solid	$200 \times 256 \times 64$
	Porous $d = 0.2R$	$210 \times 256 \times 64$
	Porous $d = 0.5R$	$225 \times 256 \times 64$
$Re = 1.0 \times 10^5$ (LES)	Solid	$300 \times 512 \times 64$
	Porous $d = 0.2R$	$375 \times 512 \times 64$
	Porous $d = 0.5R$	$425 \times 512 \times 64$

independent. Here Da and ϕ as the parameters to be varied is chosen. Note that changing ϕ under a given Da is equivalent to changing d_p. The parametric study is performed by two-dimensional simulation at $Re = 1000$ in order to save computational cost.

Although the parametric study should be performed by three-dimensional computation in a strict sense, two-dimensional computation is used by the following reason. As mentioned in Choi *et al.* (2008), the effects of flow around a bluff body has a boundary-layer control aspect and a direct-wake control aspect. Since the boundary layer of the present target flows are still two dimensional laminar states, appropriate effects of the aspect of the boundary-layer control are expected to be obtained through two-dimensional computations. As for the direct-wake control aspects, if an effect to displace the spanwise phase is expected, two-dimensional computation is inadequate. In the present case, however, such an effect is not expected due to the assumed two-dimensional configuration. Thus, two-dimensional computation is considered appropriate for the present parametric study.

There are many parameters involved in the present problem and it is impossible to cover all the combinations. Thus, the values similar to those used in the experiment (Sueki *et al.* 2010) is basically assumed. In total 446 cases are simulated in the ranges of $1.0 \times 10^{-3} \leq Da \leq 1.0$ and $0.8 \leq \phi \leq 0.95$.

The mean drag coefficient $\overline{C_D}$ and the RMS lift coefficient C_L' are computed as

$$\overline{C_D} = \frac{\overline{F_x}}{\frac{1}{2}\rho U_\infty^2 D L_z} , \qquad C_L' = \frac{\sqrt{\overline{(F_y{}')^2}}}{\frac{1}{2}\rho U_\infty^2 D L_z} , \tag{3.4}$$

where F_x and F_y denote the force components in the streamwise and the perpendicular directions, respectively. The force acting on the cylinder $\boldsymbol{F}$ is calculated by integrating Eq. (3.1):

$$\boldsymbol{F} = \oint_{\partial\Omega} p\boldsymbol{n} ds + \oint_{\partial\Omega} \boldsymbol{\tau} \cdot \boldsymbol{n} ds + \int_{\Omega} \boldsymbol{K} dv , \tag{3.5}$$

where $\boldsymbol{n}$ is the unit vector normal to the porous surface $\partial\Omega$. The first and second terms are the pressure and viscous contributions; the third term is an additional contribution due to the resistance in the porous media.

(a)

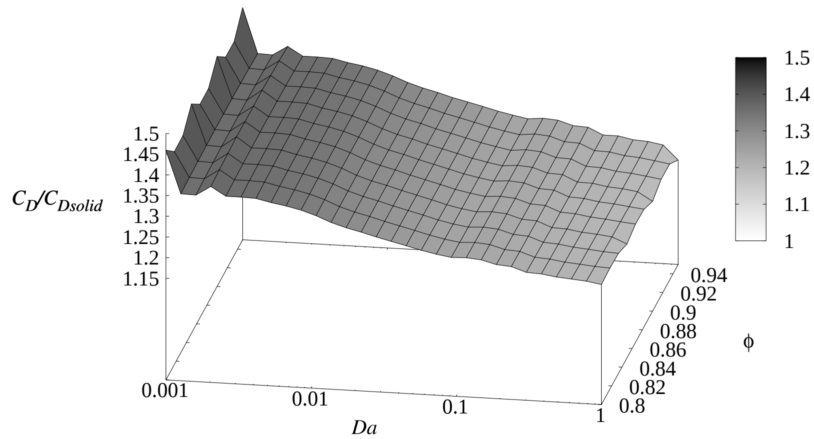

(b)

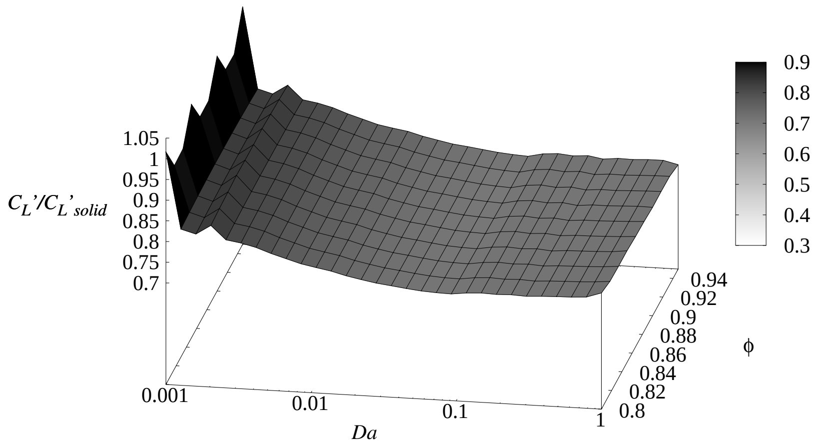

Fig 3.3: Mean drag and lift fluctuations $\overline{C_D}$ and C_L' normalized by the values of solid case, computed under different values of Darcy number Da and dimensionless particle diameter d_p (Re = 1000, d = 0.2R, 2D simulation): (a) $\overline{C_D}$; (b) C_L'.

(a)

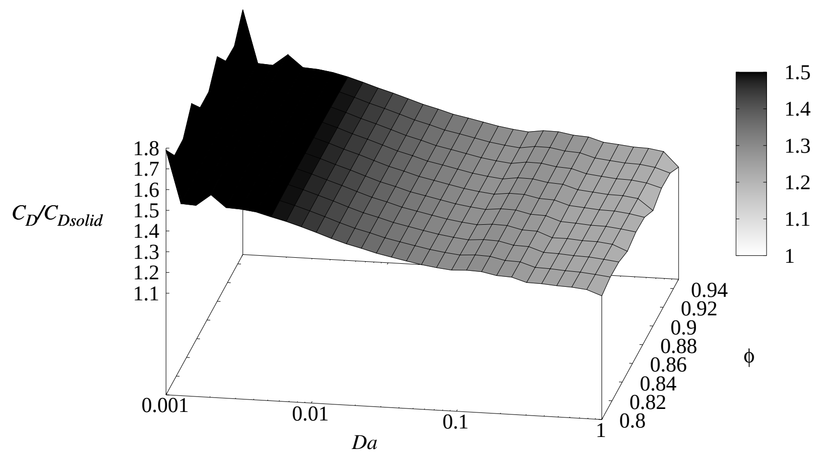

(b)

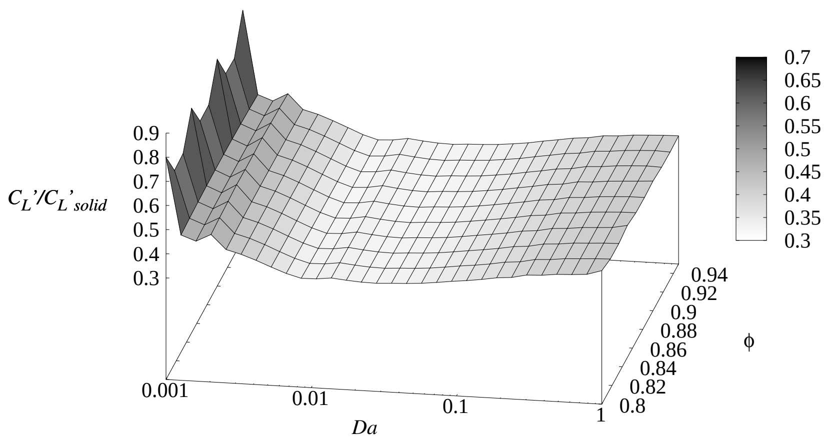

Fig 3.4: Mean drag and lift fluctuations $\overline{C_D}$ and C'_L normalized by the values of solid case, computed under different values of Darcy number Da and dimensionless particle diameter d_p (Re = 1000, d = 0.5R, 2D simulation): (a) $\overline{C_D}$; (b) C'_L.

Figure 3.3 shows the results of the case of thin porous surface ($d = 0.2R$). Both the mean drag and lift fluctuations are more sensitive to the Darcy number than the porosity. This is simply due to the difference in the parameter ranges considered here: while Da is varied in three decades, ϕ is always on the same order of magnitude. In all cases, $\overline{C_D}$ is increased and C_L' is decreased as compared to the solid case.

The results of thick porous surface case ($d = 0.5R$) is represented in Fig. 3.3. In this case, $\overline{C_D}$ becomes larger and C_L' becomes smaller than the thin surface case. Within the present parameter range, the maximum suppression of lift fluctuations (i.e., 78% reduction) is obtained in the case of $Da = 2.0 \times 10^{-2}$ and $\phi = 0.95$. Since our main focus is suppression of lift fluctuations, which is closely related to noise reduction, we select these values to be used in the study presented in the following sections.

3.4 Flow modification at $Re = 1000$

At $Re = 1000$, the boundary layer is laminar, but the wake is three-dimensional (Zdrakovich). Here, we present the flow modification by porous media at $Re = 1000$ obtained by three-dimensional simulations. The thickness of porous layer is either 20% (Case A) or 50% (Case B) of the total cylinder radius R.

3.4.1 Instantaneous flow structure

Before investigating the modification in detail, we quickly overview some instantaneous fields to see how the flow field is modified by the porous media.

Figure 3.5 shows an instantaneous three-dimensional vortical structure in each case. In the solid case, developing shear layer in the vicinity of the surface shows complex three-dimensionality and the wake region is strongly disturbed. Such three-dimensionality is suppressed in Case B; namely, vortex shedding is more synchronized in the spanwise direction.

More concrete discussion of three-dimensionality can be done by looking at the spanwise differential of the streamwise velocity fluctuations $\overline{(\frac{\partial u_x'}{\partial z})^2}$ shown in Fig. 3.6. The effect of three-dimensionality suppression can be seen clearly; $\overline{(\frac{\partial u_x'}{\partial z})^2}$ is suppressed by the porous surface, and the effect is remarkable especially in Case B. Cross-sectional Integrations ($\int_\Omega \overline{(\frac{\partial u'_x}{\partial z})^2} ds$) in Solid case, Case A and Case B are 1.40, 0.63, and 0.23, respectively, which again suggest the suppression of three-dimensionality by the porous surface.

An instantaneous field of spanwise vorticity,

$$\omega_z = \frac{\partial v}{\partial x} - \frac{\partial u}{\partial y} = \frac{1}{r}\frac{\partial (r u_\theta)}{\partial r} - \frac{1}{r}\frac{\partial u_r}{\partial \theta} , \tag{3.6}$$

in a cross-section is depicted in Fig. 3.7. It is obvious that the shear in the vicinity of cylinder is relaxed by the porous layer and the spanwise vorticity in the near wake is weakened. The small-scale structure due to streamwise vortices observed in the solid case is also suppressed in the porous case, which confirms that the vortex shedding in the porous case is more two dimensional than that in the solid case.

An instantaneous pressure field at the same time instant as Fig. 3.7 is shown in Fig. 3.8. It indicates that the pressure gradient near the stagnation point is reduced in the porous case due to the non-zero velocity on the porous surface. The pressure gradient in the shear layer and the pressure drop in the wake are also apparently weakened.

(a)

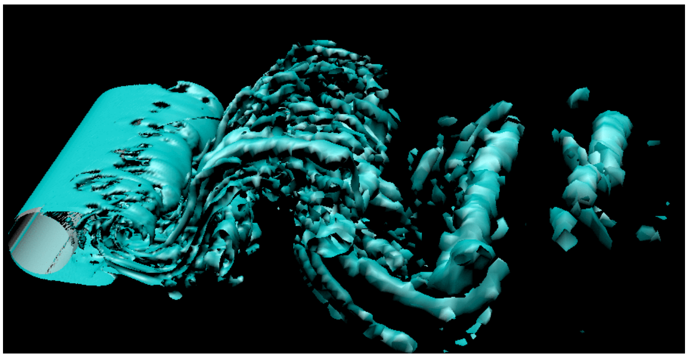

(b)

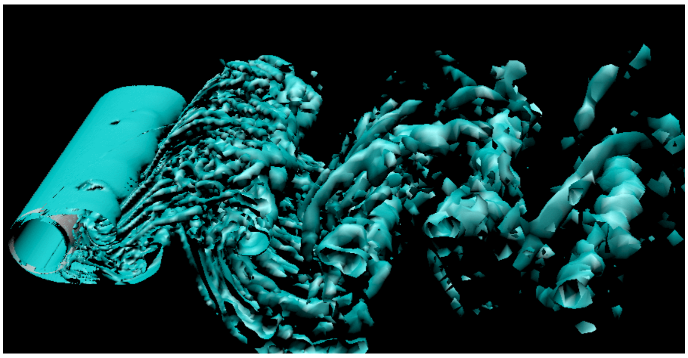

(c)

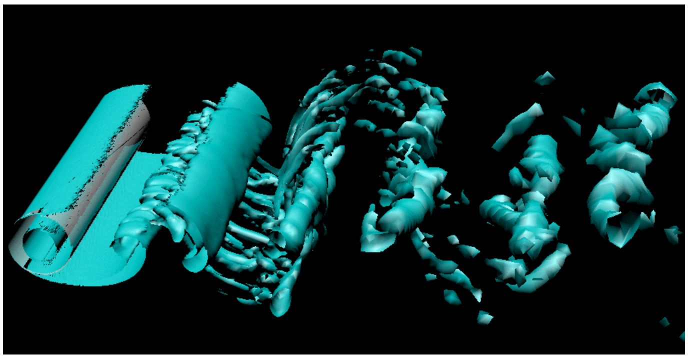

Fig 3.5: Vortical structure (Re = 1000, 3D DNS), $\|\Omega\|^2 - \|S\|^2$ = 0.8: (a) solid case; (b) Case A; (c) Case B.

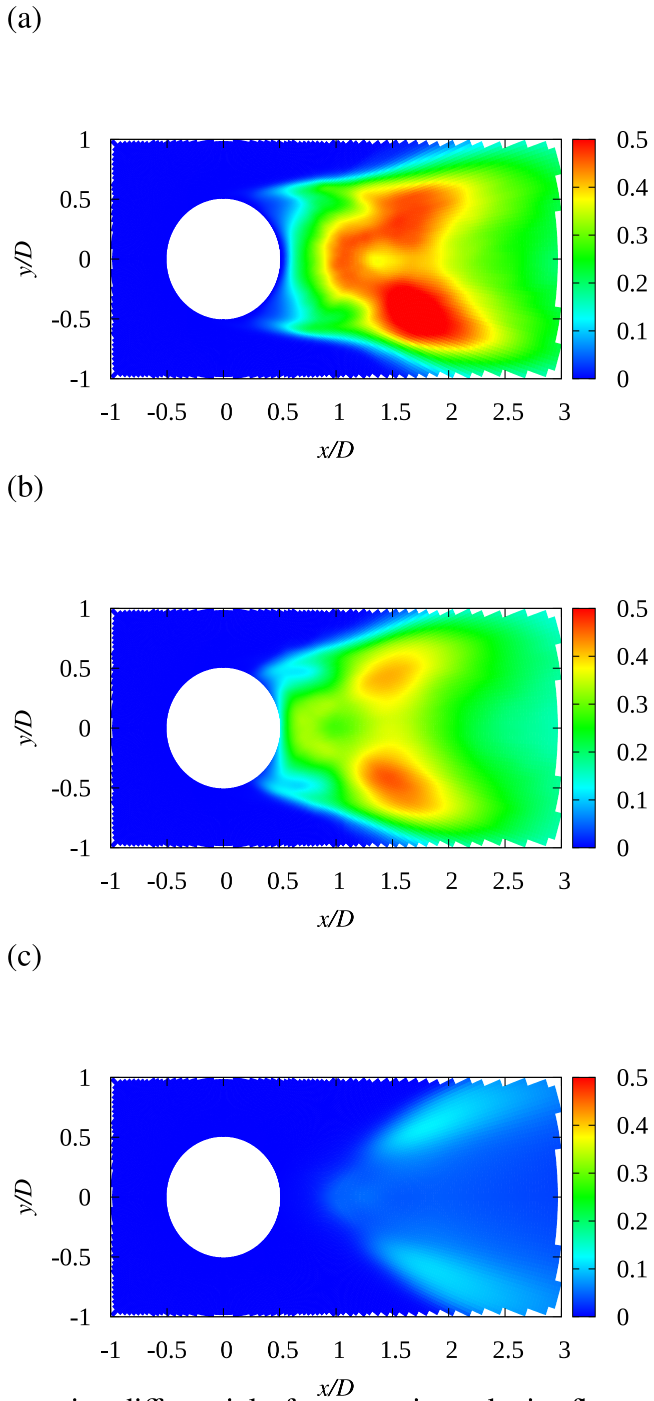

Fig 3.6: spanwize differential of streamwise velocity fluctuation $\overline{(\partial u'_x/\partial z)^2}$ (Re = 1000, 3D DNS): (a) solid case; (b) Case A; (c) Case B.

(a)

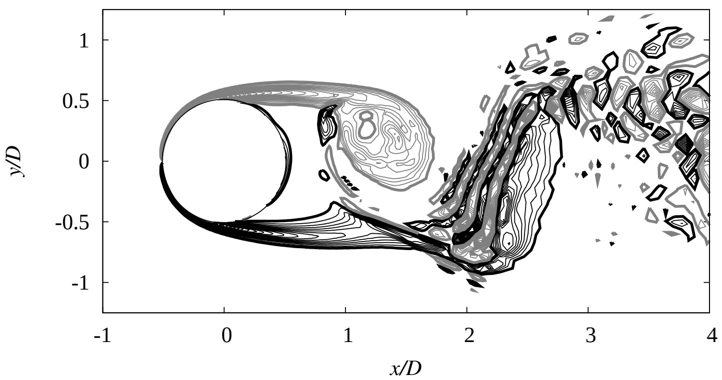

(b)

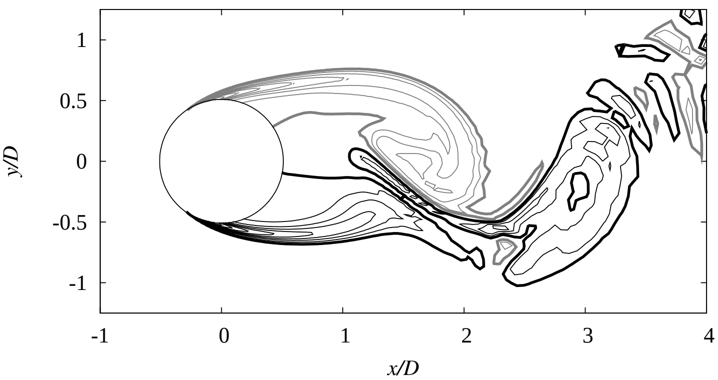

Fig 3.7: Instantaneous vorticity field, ($Re = 1000$, 3D DNS): (a) solid case; (b) Case B. Contour lines: $-15 \leq \omega_z \leq 15$ with increment of 0.6; black, $\omega_z > 0$; gray, $\omega_z < 0$; thick lines, $\omega_z = \pm 0.6$.

3.4.2 Drag, lift force and quantities near the surface

Figure 3.4.2 shows the time traces of drag and lift coefficients. The time t is made dimensionless by using U_∞ and D, and $t = 0$ denotes an instant after the flow reaches its statistically steady state. The drag is increased in both Case A and Case B. On the other hand, the lift force fluctuation is increased in Case A and slightly decreased in Case B. The mean drag ($\overline{C_D}$) in each case is 1.09 (Solid), 1.68 (Case A) and 1.90 (Case B), and the RMS lift fluctuations (C'_L) is 0.21 (Solid), 0.39 (Case A) and 0.17 (Case B), respectively. The reduction rate in C'_L (i.e., 19% in Case B) is much smaller than that observed in the two-dimensional simulation (i.e., 78%) presented in the previous section. In the two dimensional simulation, the vortex shedding is, of course, always synchronized in

(a)

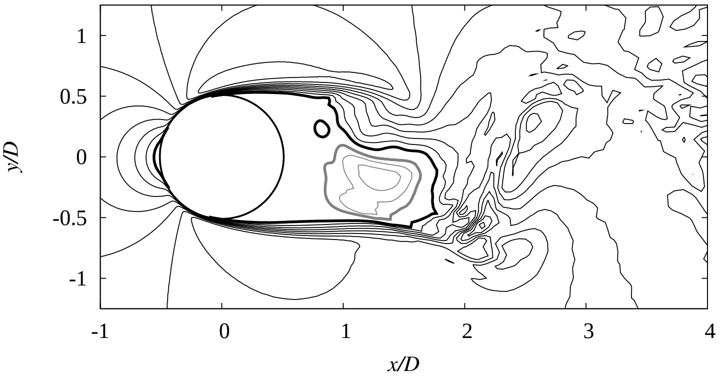

(b)

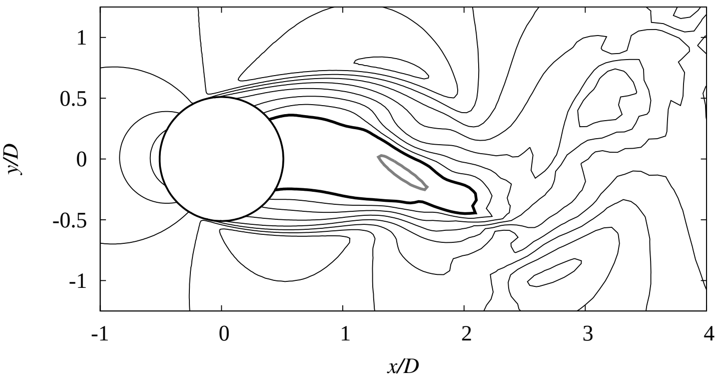

Fig 3.8: Instantaneous pressure field, (Re = 1000, 3D DNS): (a) solid case; (b) Case B. Contour lines: $-1.5 \leq p \leq 1.5$ with increment of 0.15; black, $p > 0$; gray, $p < 0$; thick lines, $p = \pm 0.15$.

the spanwise direction; thus, C'_L is directly related to the "local" lift force fluctuations. In contrast, in the three-dimensional case, the vortex shedding at different spanwise locations has phase difference; thus, C'_L, which is averaged over the span, is much smaller than the amplitude of local lift force fluctuations at a single spanwise location. When the porous media is applied, the vortex shedding becomes more two-dimensional as observed above, which works to increase C'_L; at the same time the shed vortex becomes weaker, which works to reduce C'_L. The larger reduction rate obtained in the two-dimensional simulation can thus be explained by absence of the former effect to increase C'_L.

Figure 3.10 shows different constitutions to the total drag: the pressure contribution C_{Dp}, the frictional contribution C_{Df}, and the drag inside the porous media C_{Dk}. In all cases, C_{Dp} is dominant and C_{Df} is much smaller than the other components; C_{Df} becomes even smaller in porous cases. For thicker porous layer, C_{Dk} becomes larger: in Case B, C_{Dk} amounts to 30% of the total drag.

Figures 3.11(a) and (b) show the distributions of the pressure coefficient C_p and the friction coefficient C_f on the cylinder surface, defined respectively as

$$C_p = \frac{\overline{p}_w - p_\infty}{\frac{1}{2}\rho U_\infty^2}\,, \qquad C_f = \frac{\tau_w}{\frac{1}{2}\rho U_\infty^2}\,, \tag{3.7}$$

where $\overline{p}_w$, p_∞ and τ_w denote the mean wall pressure, the free-stream pressure, and the mean wall-shear stress, respectively. The stagnation pressure is found to be lower than unity in porous cases due to the non-zero velocity on the porous surface. The lower pressure in Case B suggests that the velocity at the stagnation point is higher than that in Case A. Although the pressure distribution on a solid cylinder usually has a local minimum point in the Reynolds number range studied here, as can be found in literature (e.g., Zdrakovich)), such a local minimum is absent in the porous cases. The higher pressure on the front side ($40° \leq \theta \leq 80°$) results in the increase of C_{Dp} of porous cases. The smaller C_{Dp} in Case B than Case A is due to the higher pressure on the rear side ($100° \leq \theta \leq 180°$). As for the friction, C_f in the porous cases is much smaller than that in the solid case due to the slip velocity on the porous surface.

(a)

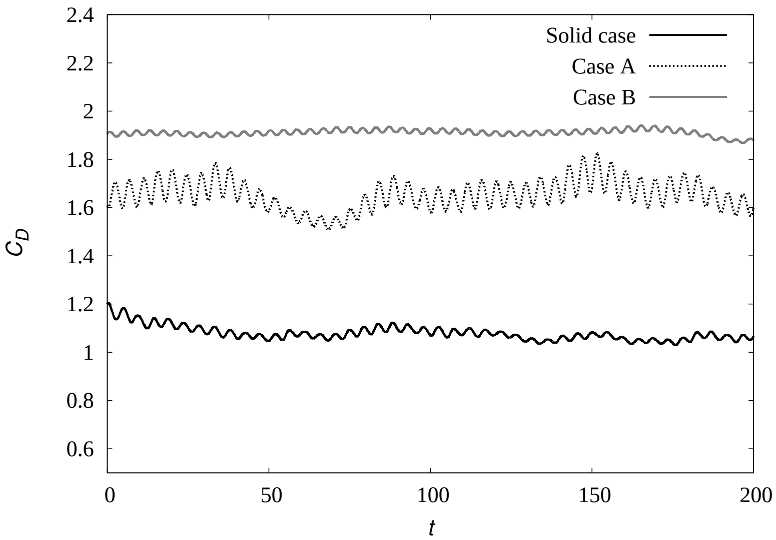

(a)

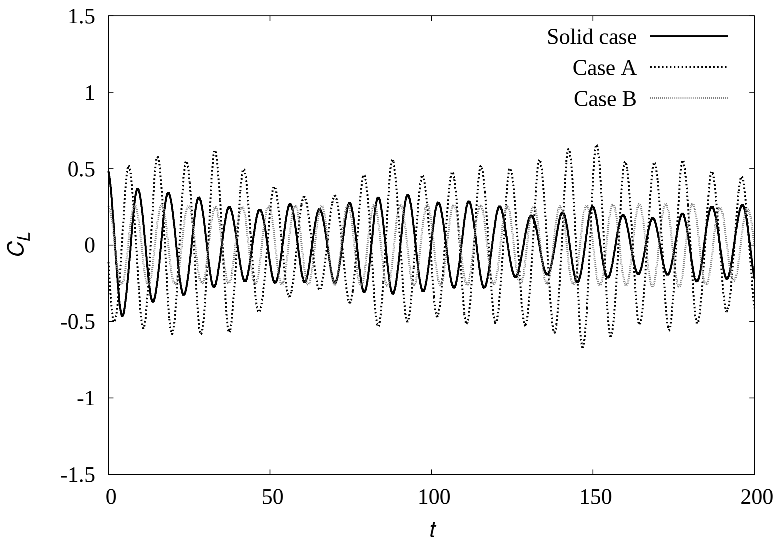

Fig 3.9: Time traces of drag and lift coefficients (Re = 1000, 3D DNS): (a) drag coefficient C_D; (b) lift coefficient C_L.

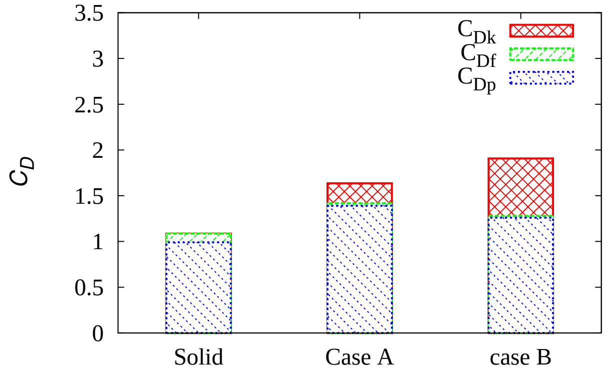

Fig 3.10: Composition of mean drag coefficient (Re = 1000, 3D DNS).

The distribution of RMS pressure coefficient C'_p, defined as

$$C'_p = \frac{\sqrt{\overline{p'^2}}}{\frac{1}{2}\rho U_\infty^2}, \tag{3.8}$$

is shown in Fig. 3.11(c). The pressure fluctuation is increased in Case A and decreased in Case B. Although the local maximum in Case B has a magnitude comparable to that in the solid case, its location is shifted backward. Because the lift force is calculated by $\int p \sin\theta d\theta$, such backward shift leads to the suppression of the lift fluctuation.

Figure 3.12 illustrates the mean azimuthal velocity profiles near the cylinder surface. It is clear that the surface velocity is non-zero in Cases A and B. Due to this slip velocity, the friction on the porous surface is reduced as observed in Fig. 3.11(b). The azimuthal velocity inside the porous media of Case B looks “fully developed” away from the wall and back flow is observed near the solid surface. In contrast, Case A shows spatially developing azimuthal velocity profiles with smaller amount of back flow. The velocity distribution indicates that the flux in the porous media is larger in Case B.

Figure 3.13 shows the distribution of mean wall-normal velocity on the porous surface. The fluid is sucked in the front half, which reduces the pressure at the stagnation point as observed in Fig. 3.11(b), and blown in the rear half. The outward wall-normal velocity takes its maximum value around 92° in Case A and 113° in Case B.

(a)

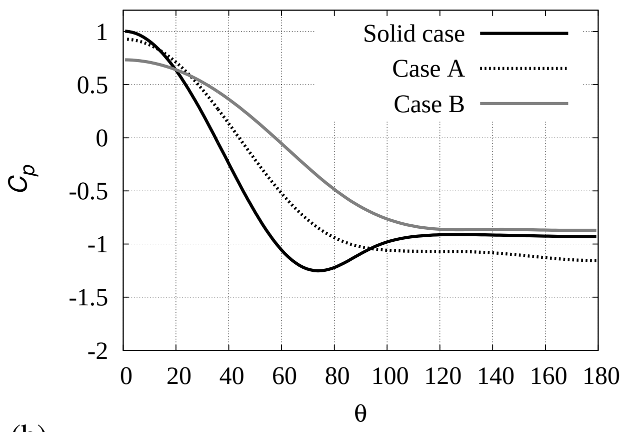

(b)

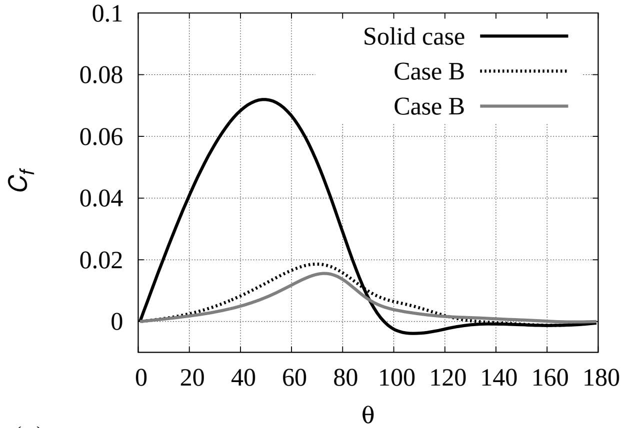

(c)

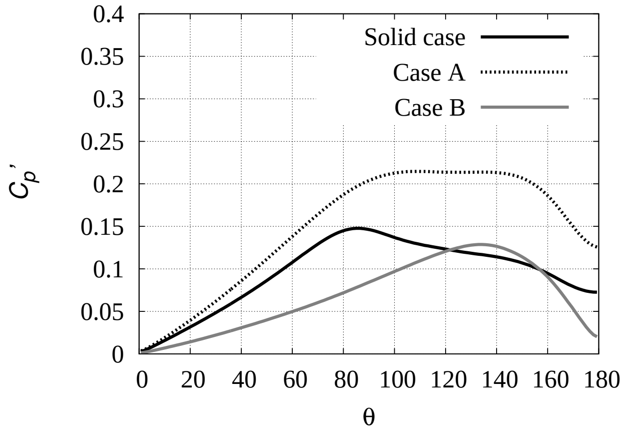

Fig 3.11: Local force distribution on the surface (Re = 1000, 3D DNS): (a) pressure coefficient (C_p); (b) friction coefficient (C_f); (c) RMS of pressure coefficient (C_p').

(a)

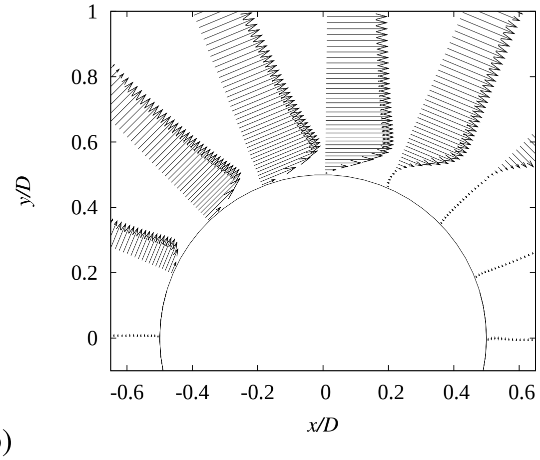

(b)

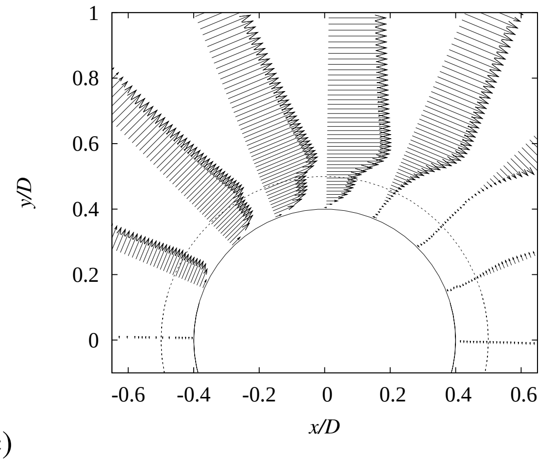

(c)

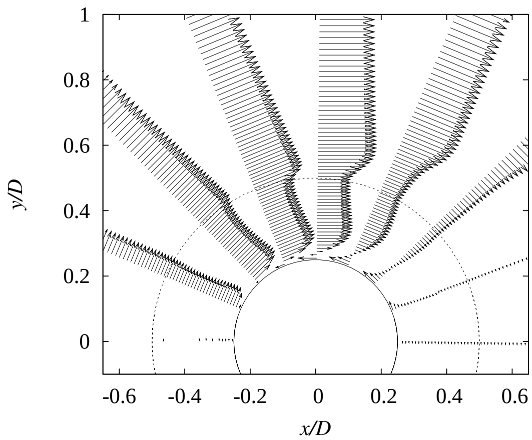

Fig 3.12: Mean circumferential velocity profiles (*Re* = 1000, 3D DNS): (a) solid case; (b) Case A; (c) Case B. Solid line, surface of solid cylinder; dotted line, porous surface.

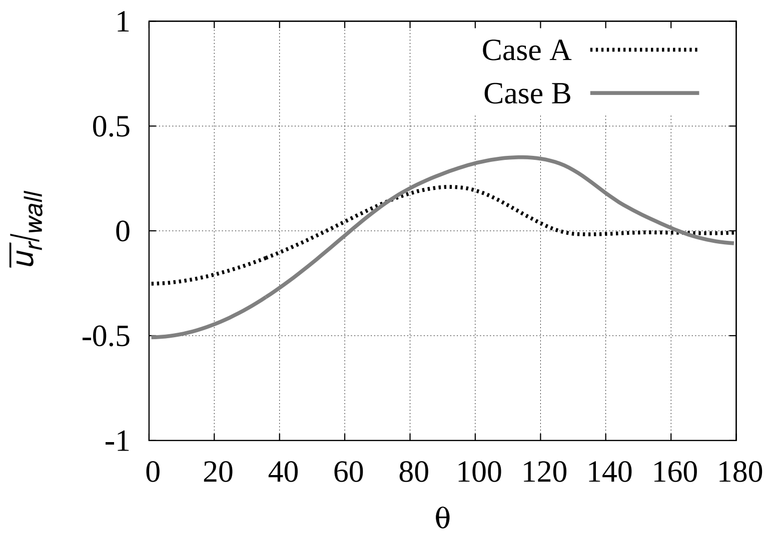

Fig 3.13: Mean wall-normal velocity on the porous surface (*Re* = 1000, 3D DNS)

3.4.3 Statistics in the downstream wake

Figure 3.14(a) shows the mean streamwise velocity in the downstream wake. The momentum deficit in the porous case is smaller than that in the solid case in the near wake, but larger in the far wake. The smaller deficit in the near wake is the direct consequence of modification near the surface observed above. However, the increase of deficit in the far wake cannot be explained simply by the modification near the surface. According to the mean pressure distribution in the downstream wake, as shown in Fig. 3.16, the mean pressure field is found to be modified globally; in particular, the mean streamwise pressure gradient the porous case is increased in the region of $6 < x/D < 10$ as compared to the solid case. This larger pressure gradient is considered to cause the larger momentum deficit in the far wake (Fig. 3.14(a)) through the acceleration of flow toward the upstream direction.

The mean lateral velocity, shown in Fig. 3.14(b), is largely modified at $x/D = 1$. This can be attributed to the change in the length of recirculation region, as will be shown below (Fig. 3.17). Although the lateral velocity is considerably smaller than the streamwise velocity, slightly stronger outward motion in the far wake can be noticed in the porous case. Note that some dissymmetry observed in the far wake seems to be due to the insufficient integration time. Computation with twice as long integration time ($TU_\infty/D = 400$) as the original one ($TU_\infty/D = 200$) has been computed, but dissymmetry was still observable. Since the value of mean lateral velocity itself is very small in the far wake, an extraordinarily long integration time may be needed in order to obtain a profile which looks completely antisymmetric.

The component of theReynolds stress, $\overline{u'u'}$, is shown in Fig.3.15(a). Near the cylinder two peaks corresponding to vortices are clearly seen. Case A represents the largest peak at $x/D = 1$, but at $x/D = 1$ al cases become almost identical and decay gradually in the downstream.

Figure 3.15(b) shows $\overline{v'v'}$ component. Similaly to the $\overline{u'u'}$ component, Case A shows a relatively large value at $x/D = 1$. While the solid case and Case A show the large deficits in the far downstream region, the deficit of Case B is suppressed slightly and shows larger $\overline{v'v'}$.

As for the Reynolds shear stress $\overline{u'v'}$, the near field profiles show the same tendency as that of $\overline{u'u'}$ and $\overline{v'v'}$ components.

Figure 3.17 shows the mean streamwise velocity on the centerline. Compared to the solid case, the recirculation region is found to be shortened in the porous cases; moreover, the velocity inside the recirculation region is much reduced in Case B. Recall that the mean lateral velocity is largely modified at $x/D = 1$. At that location, the velocity gradient $\partial\overline{u}/\partial x$ is negative in solid case, positive in Case A, and slightly positive in Case B. Due to the continuity, $\partial\overline{v}/\partial y$ takes the sign opposite to $\partial\overline{u}/\partial x$, which is consistent with the observations in Fig. 3.14 (b). In contrast, at $x/D = 2$, i.e., downstream of the recirculation region, $\partial\overline{u}/\partial x$ is positive in all cases with a similar magnitude. Therefore, the difference in lateral velocity profiles is small. Similarly, the positive $\partial\overline{v}/\partial y|_{y=0}$ observed in the far wake of Case B can be explained by the increase of streamwise momentum deficit, i.e., $\partial\overline{u}/\partial x < 0$ in the region of $x/D > 4$.

In order to discuss the modification from the viewpoint of vorticity, the RMS vorticity distributions at different locations are shown in Fig. 3.18. The spanwise vorticity ω_z is generated on the cylinder surface; therefore, $\omega_{z,rms} = \sqrt{\overline{\omega_z'^2}}$ is large near the cylinder and gradually smoothed in the downstream. On the other hand, the streamwise vorticity $\omega_x = \partial w/\partial y - \partial v/\partial z$ is generated by the reorientation from the spanwise vorticity ω_z; thus, the maximum value of $\omega_{x,rms} = \sqrt{\overline{\omega_x'^2}}$ is found at a bit downstream. The spanwise vorticity of porous case is smaller than that of the solid case due to the slip-velocity on the porous surface, while the profiles nearly collapse in the downstream region, $x/D \geq 4$. Observing the smaller streamwise vorticity in the porous case, the slightly higher value of $\omega_{z,rms}$ in the far wake of the porous case can be attributed to the smaller amount of reorientation of spanwise vortices to the streamwise ones.

(a)

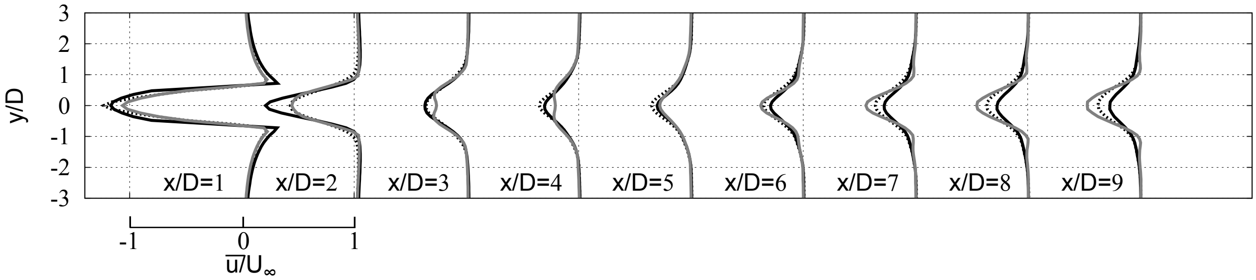

(b)

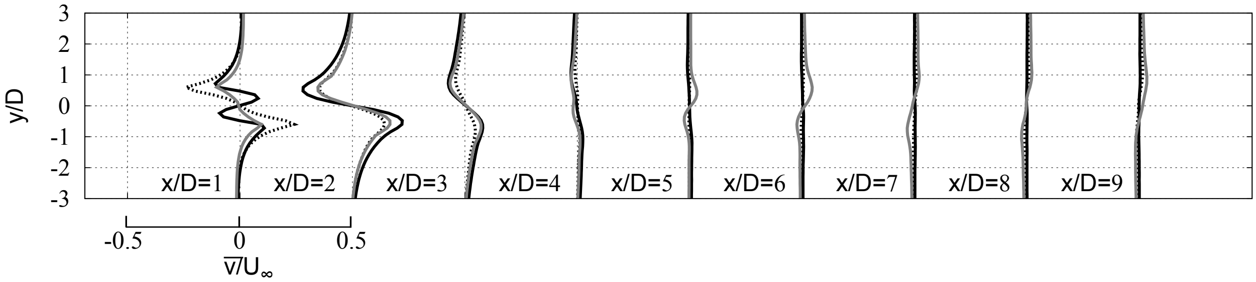

Fig 3.14: Mean velocity profiles (Re = 1000, 3D DNS): (a) mean streamwise velocity; (b) mean lateral velocity. Black solid line, solid case; black dotted line, Case A; gray solid line, Case B.

(a)

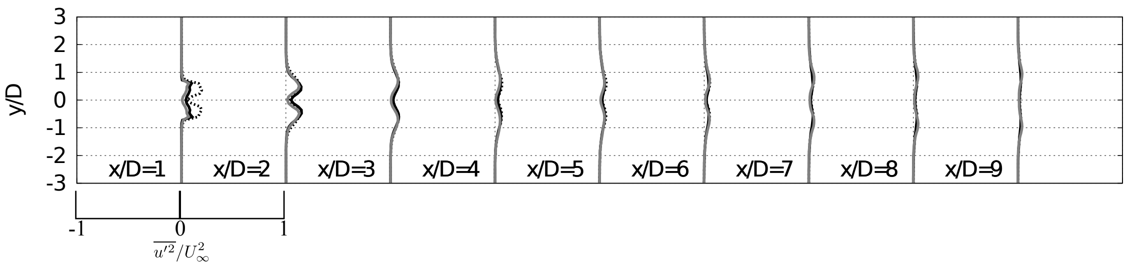

(b)

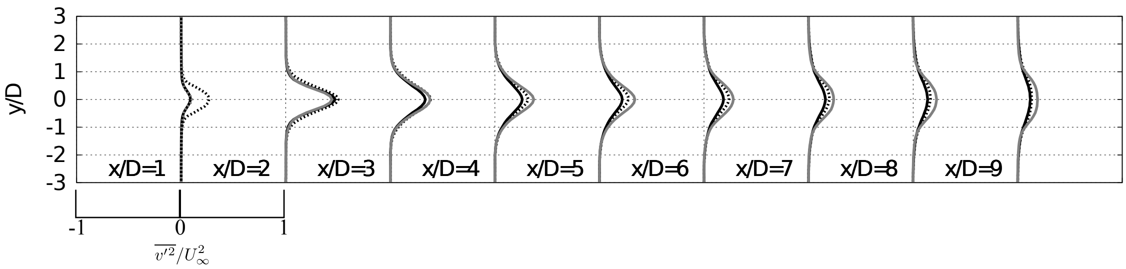

(c)

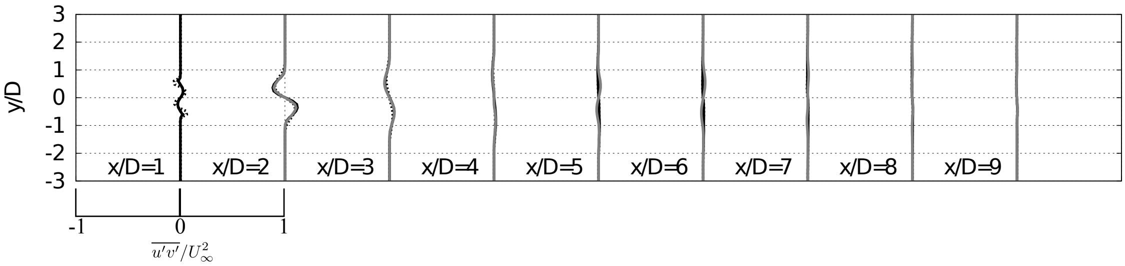

Fig 3.15: Profiles of Reynolds stress (Re = 1000, 3D DNS): (a) $u'u'$; (b) $v'v'$; (c) $u'v'$. Black solid line, solid case; black dotted line, Case A; gray solid line, Case B.

(a)

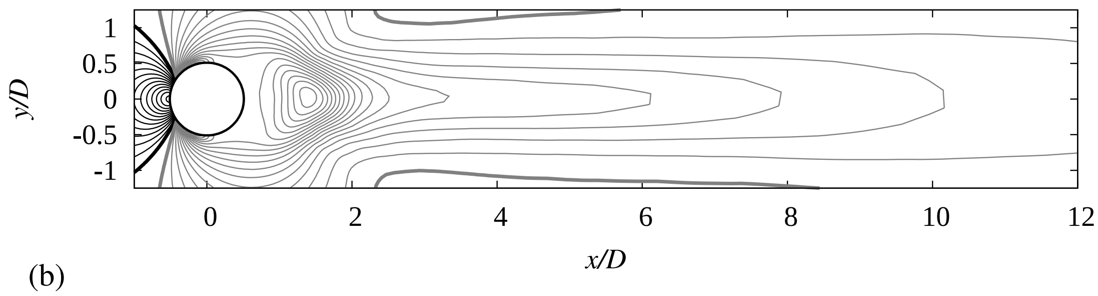

(b)

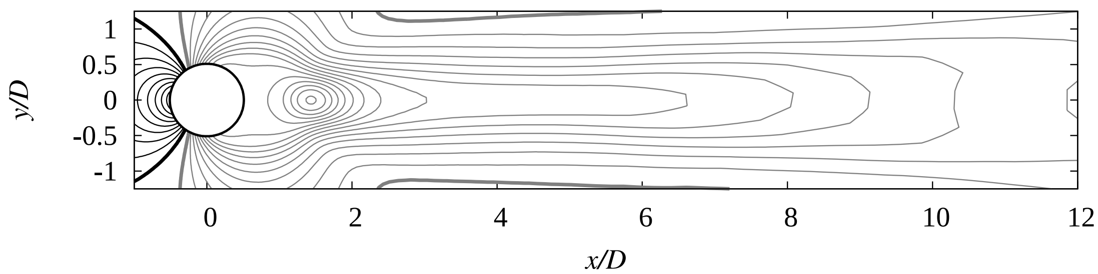

Fig 3.16: Mean pressure field (Re = 1000, 3D DNS): (a) solid case; (b) Case B. Contour lines: $-1.5 \le \overline{p} \le 1.5$ with increment of 0.075; black, $\overline{p} > 0$; gray, $\overline{p} < 0$; thick lines, $\overline{p} = \pm 0.075$.

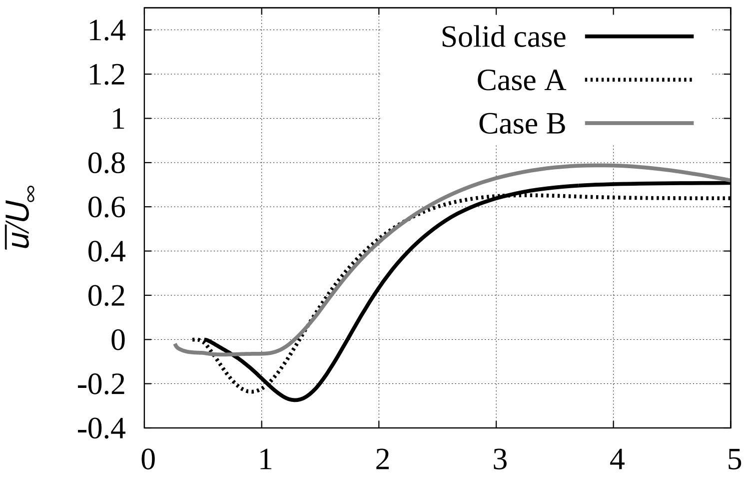

Fig 3.17: Mean streamwise velocity on the centerline, i.e., $y/D = 0$ (Re = 1000, 3D DNS).

(a)

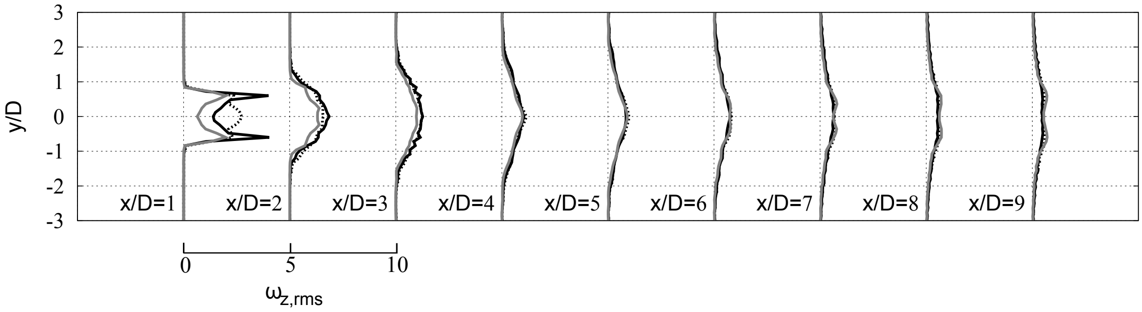

(b)

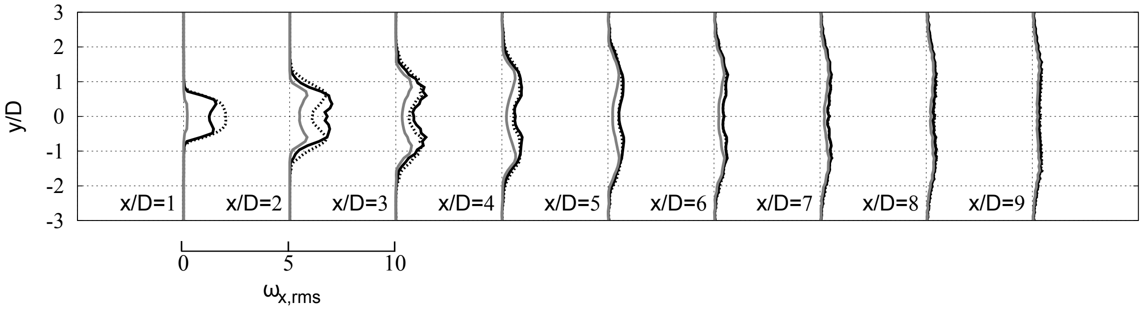

Fig 3.18: RMS vorticity: (a) spanwise component; (b) streamwise component (Re = 1000, 3D DNS). Black solid line, solid case; black dotted line, Case A; gray solid line, Case B.

3.5 Reynolds number dependency

So far, we have discussed the effects of porous media at a fixed Reynolds number, i.e., $Re = 1000$. In this section, the dependency of porous media effect on the Reynolds number is investigated. We look at the results at: $Re = 100$, where the wake is completely two-dimensional; $Re = 3900$, a higher Reynolds number, at which previous studies are available for comparison; and $Re = 1.0 \times 10^5$, which is close to the Reynolds number in the experimental study by Sueki *et al.* (2010).

The drag coefficient $\overline{C_D}$ and the RMS lift coefficient C_L' are shown in Table 3.2 and their ratios to the solid values are plotted in Fig. 3.19 as functions of Reynolds number. Except for the two-dimensional regime, i.e., $Re = 100$, the amount of drag increase becomes smaller with the Reynolds number. The drag increase in Case B is larger than Case A at lower Reynolds number and smaller at higher Reynolds number. The lift fluctuations also decrease with Reynolds number except for Case A in the two-dimensional regime. The high value of C'_L at $Re = 1000$ can be attributed to the recirculation region moved closer to the cylinder surface. The reduction of C'_L is more effective at higher Reynolds number and the lift fluctuation is completely suppressed at $Re = 1.0 \times 10^5$ in Case B.

Here we back to Eq.(3.2) and look at the force ratio between the first term and the second term, since the first term contains the Reynolds number. Figure 3.20(a)(b) represent the ratio of the forces contributing to the drag, and the ratio of the forces contributing to the RMS of lift, respectively. For both figures, it is shown that the contribution of the second term becomes dominating when the Reynolds number is large. Since the classical Brinkman model does not contains velocity square terms such as the second term of the present porous media model (3.2), the results using the classical model would show completely another results.

Figure 3.21 shows instantaneous vorticity fields at $Re = 1.0 \times 10^5$. In the porous case (Case B), the vortex shedding is completely suppressed and the shear layers are nearly symmetric. This is similar to the experimental observation of Sueki *et al.* (2010).

The power spectral density (PSD) of lift coefficient C'_L in each case is compared in Fig. 3.22 together with that in literature (Schewe (1983), $Re = 1.3 \times 10^5$). Although the Reynolds numbers are slightly different, the Strouhal number in the present solid case, i.e., $St = fD/U_\infty = 0.18$, is in fair agreement with that of Schewe's, i.e., $St = 0.20$. Furthermore, the shape near the peak is similar: the slope in the low frequency side is slow and that in the high frequency side is steep. The result of Schewe has another small energy peak near $St = 0.6$ which is not present in our result. This peak seems to correspond to the eigenfrequency of the balance used for the force measurement, i.e., 385Hz, which is reported in their paper. Modification by the porous surfaces can be clearly observed. In Case A, the power is significantly reduced and the Strouhal number is slightly increased. In case B, the power is nearly zero over all frequencies, which confirms that the lift fluctuation is completely suppressed.

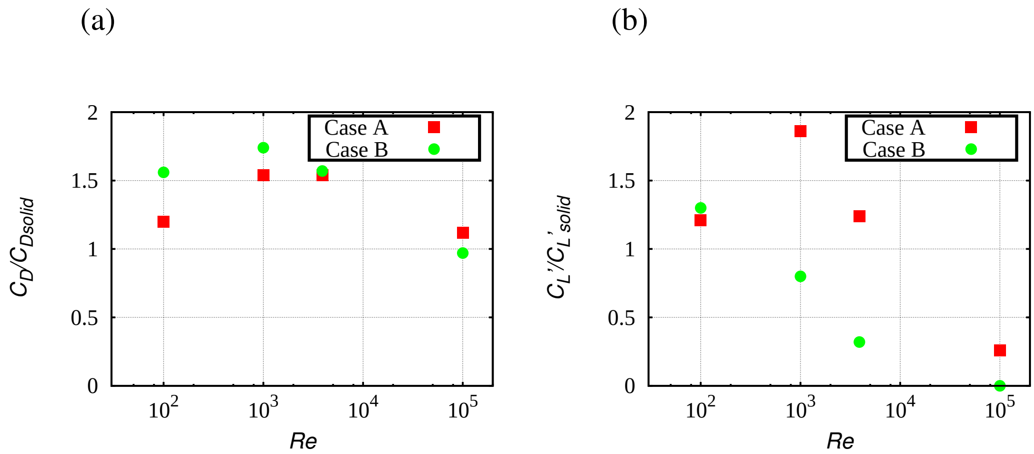

Fig 3.19: Reynolds number dependency: (a) mean drag coefficient $\overline{C_D}$; (b) RMS of lift coefficient C'_L.

Figure 3.23 shows the mean surface pressure distribution at different Reynolds numbers. As has been observed in Sec. IV, the porous surface removes the local minimum and flatten the distribution. At Re = 100, the modification is similar to, but much weaker than that at Re = 1000 (Fig. 3.11(a)). At Re = 3900, the distribution is more flattened and the base pressure C_{pb} in Case B is even higher than that at lower Reynolds number. At $Re = 1.0 \times 10^5$, the pressure distribution becomes even more flattened.

Figure 3.23 also compares the RMS surface pressure fluctuations at different Reynolds numbers. The modification at Re = 100 is similar to, but weaker than that observed at Re = 1000 (Fig. 3.11(c)). The pressure fluctuation becomes to smaller at higher Reynolds number, and eventually almost vanishes at $Re = 1.0 \times 10^5$ (Case B).

3.6 Mechanism of flow modification

We have observed in Sec. IV that several quantities closely related to flow oscillations in the downstream wake, such as wall-shear, surface pressure fluctuations, and resultant lift fluctuations are suppressed by porous surface. In Sec. V, we have also seen that the effect becomes more significant at higher Reynolds numbers and with thicker porous layer. Here, we attempt to consistently explain the mechanism of flow modification from two aspects: the dissipation of kinetic energy and the slip velocity on the porous surface.

(a) (b)

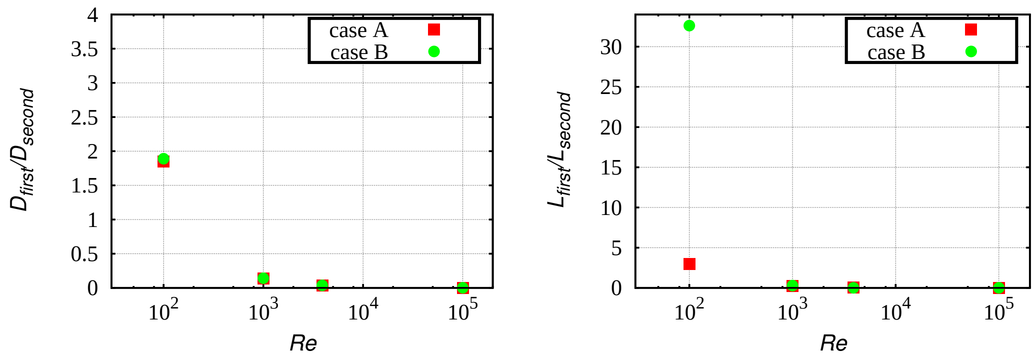

Fig 3.20: Composition of friction force inside the porous media: (a) drag; (b) RMS of lift force.

The dissipation outside the cylinder is expressed as

$$\varepsilon = \frac{\|\nabla \boldsymbol{u}\|^2}{Re} \tag{3.9}$$

in the non-dimensional form. The dissipation inside the porous media is easily obtained by multiplying the macroscopic velocity $\langle \boldsymbol{u} \rangle$ to Eq. (3.1) as

$$\varepsilon = \frac{\|\nabla \langle \boldsymbol{u} \rangle \|^2}{Re} + \langle \boldsymbol{u} \rangle \cdot \boldsymbol{K} \ , \tag{3.10}$$

where the second term accounts for the internal friction.

Figure 3.24 shows the instantaneous energy dissipation fields at $Re = 3900$. Dissipation in the porous media is found to be extremely large as compared to that in the boundary layer, detached shear layer, and wake. By this energy dissipation process, the fluid that passes through the porous media loses large amount of its energy before being ejected from the downstream side. The fluid constantly ejected from the porous surface forms a stable low-energy (low-speed and low-pressure) fluid region.

In Sec. III, we have seen that the shear and vorticity on the surface are weakened by the slip velocity. That means, the detached eddies destabilizing the flow are also weakened.

These two mechanisms consistently explain the dependencies mentioned above. The Reynolds number dependency can be explained by the diffusivity. At lower Reynolds number, the low energy fluids ejected from the porous surface is immediately diffused to wider area and convected away by high-speed flows. At higher Reynolds number,

Table 3.2: Reynolds number dependency of the computed flow properties.

Reynolds number	Surface	$\overline{C_D}$	C'_L
$Re = 100$	Solid	1.33	0.23
	Case A	1.59	0.28
	Case B	2.07	0.30
$Re = 1000$	Solid	1.09	0.21
	Case A	1.68	0.39
	Case B	1.90	0.17
$Re = 3900$	Solid	1.07	0.25
	Case A	1.65	0.31
	Case B	1.69	0.08
$Re = 1.0 \times 10^5$	Solid	1.46	0.99
	Case A	1.63	0.26
	Case B	1.42	0.00

in contrast, the ejected low-energy fluid forms a large low-energy fluid region before diffusing. Note that the turbulent diffusion is also considered to be suppressed in the stabilized wake. Thus, the porous media works better at higher Reynolds number.

Figure 3.25 shows the distribution of total pressure coefficient (i.e., a pressure coefficient built on the total pressure $p_t = p + \rho \boldsymbol{u}^2/2$) in the solid case and Case B at different Reynolds numbers. Although the difference between the solid and porous cases is small at $Re = 100$, a stronger low pressure area can be observed in porous cases. The difference becomes clearer as the Reynolds number increases. At $Re = 3900$, a very low energy region is observed in the solid case, while it is recovered in Case B. This recovery is likely due to the low energy fluid ejected from the porous surface. At $Re = 1.0 \times 10^5$, the low energy region in the porous case is expanded further downstream.

As for the dependency to the porous media thickness, we have seen that the mass flow rate inside the porous media is larger for thicker porous layer. As a result of this, the amount of low-energy fluid ejected from the porous surface and the low-energy region in the wake become larger.

One might consider that the effect is similar to so-called base bleeding. The above-

(a)

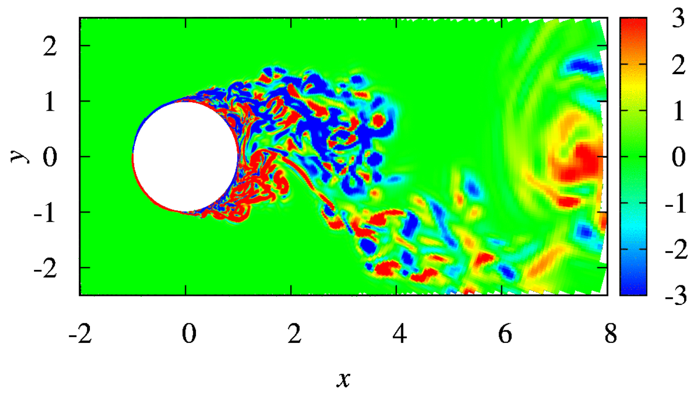

(b)

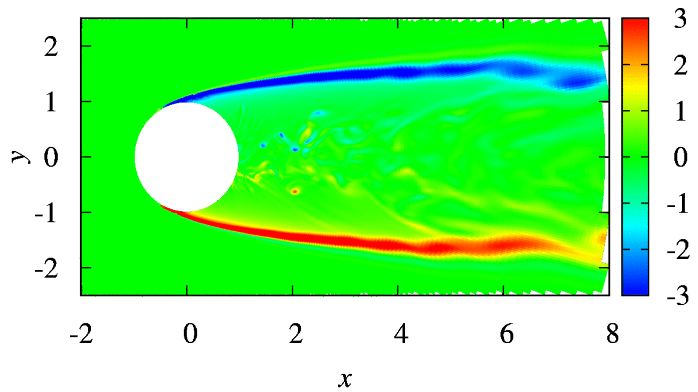

Fig 3.21: Instantaneous vorticity field (Re = 1.0×10^5, LES): (a) solid case; (b) Case B.

mentioned mechanisms, however, are not the same as the case of base bleeding. In order to demonstrate it, we conducted a numerical simulation of a solid case, but with the mean radial velocity on the surface obtained in Case B. The Reynolds number is 3900. This condition mimics the porous surface but does not account for the slip velocity and the energy dissipation inside the porous media. The computed drag coefficient is 1.36 and the RMS of lift coefficient is 0.27. The C_L' is rather increased in contrast to the huge suppression in Case B. Figure 3.26 shows the instantaneous vorticity field. The flow structure is apparently different from Case B: for instance, the shear region is spread to lateral direction. This result implies that the slip velocity on the porous surface and

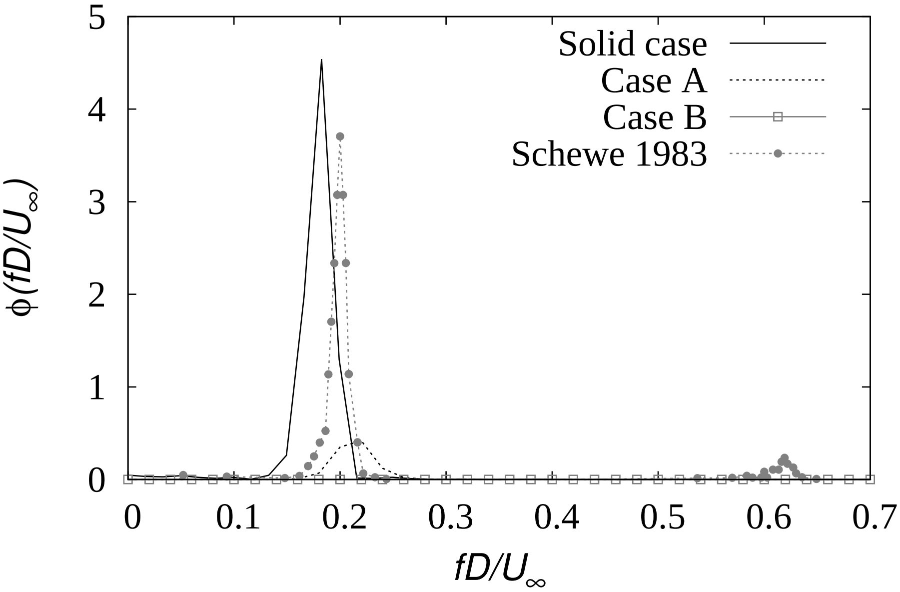

Fig 3.22: Power spectral density of lift fluctuations (Re = 1.0×10^5).

the energy dissipation process play very important role for the flow modification by the porous media.

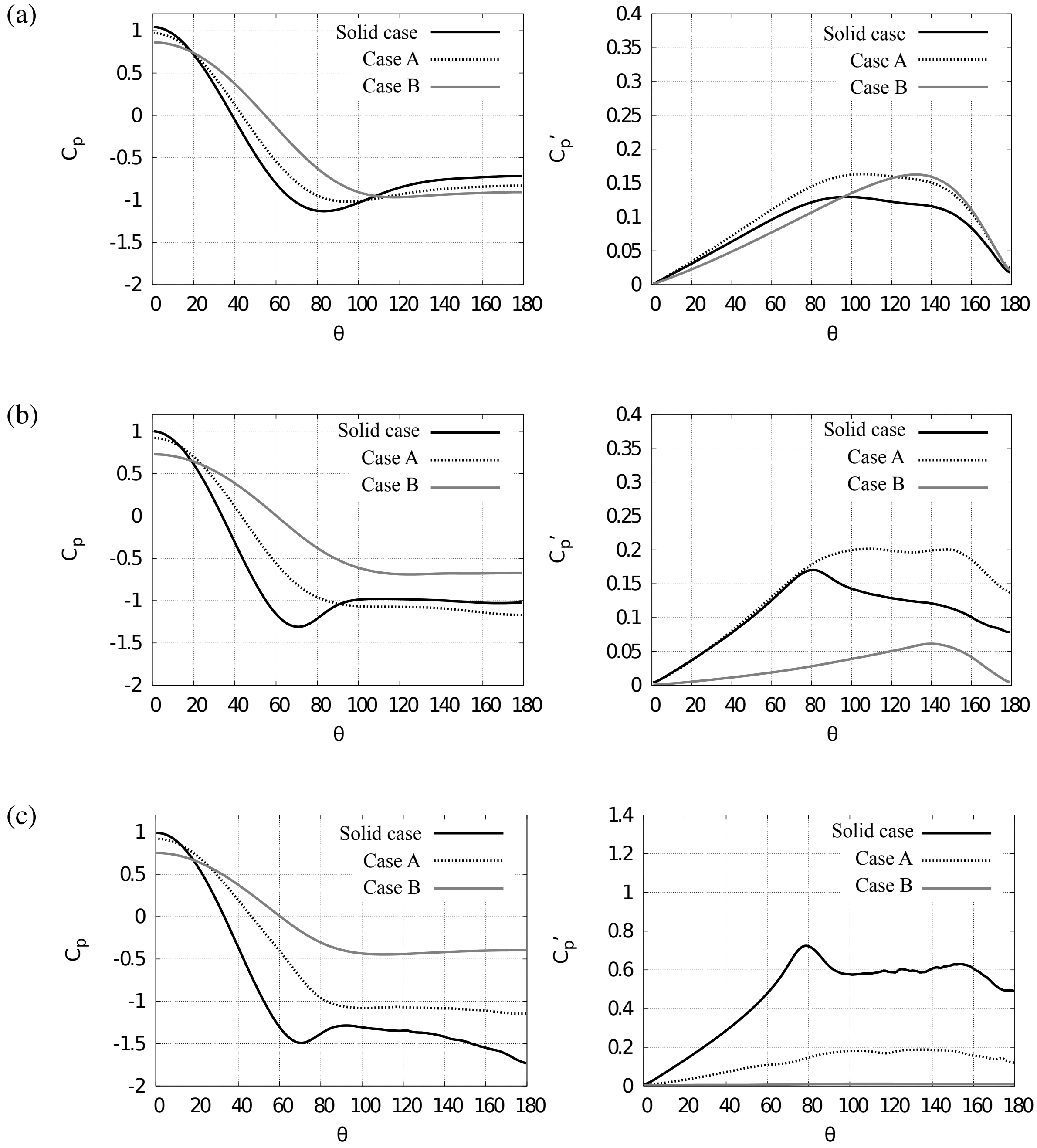

Fig 3.23: Mean ($\overline{C_p}$, left) and RMS (C'_p, right) pressure coefficients on the cylinder surface: (a) $Re = 100$; (b) $Re = 3900$; (c) $Re = 1.0 \times 10^5$.

(a)

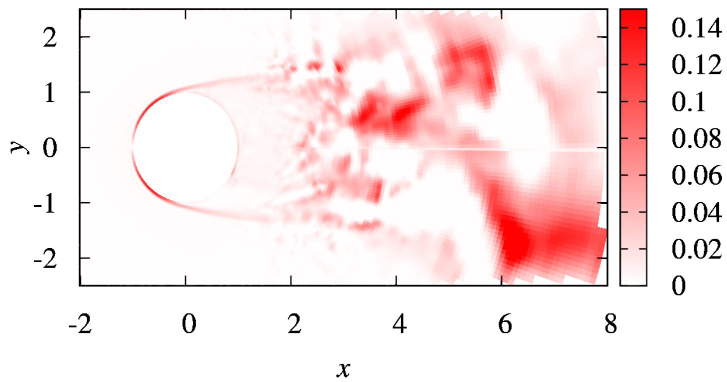

(b)

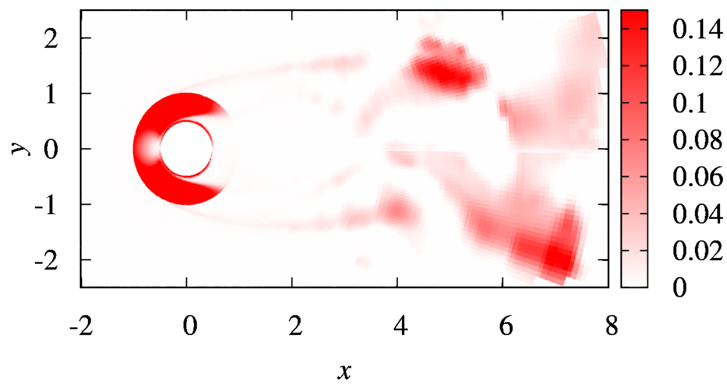

Fig 3.24: Energy dissipation ε at Re = 3900 (LES): (a) solid case; (b) Case B.

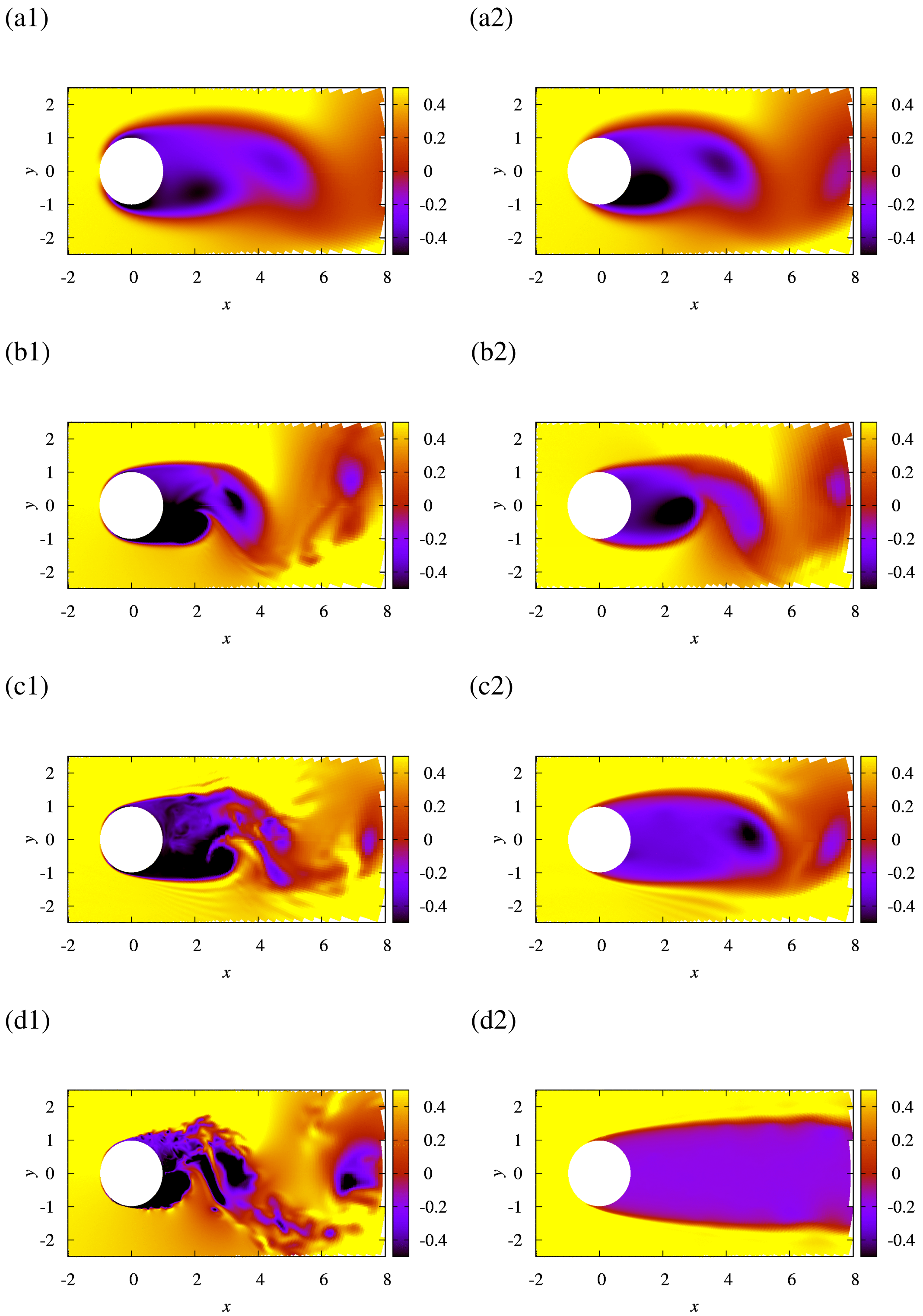

Fig 3.25: (Color online) Instantaneous distribution of total pressure coefficient (a) Re = 100; (b) Re = 1000; (c) Re = 3900; (d) Re = 1.0×10^5. (a1)-(c1) solid case; (a2)-(d2) Case B.

(a)

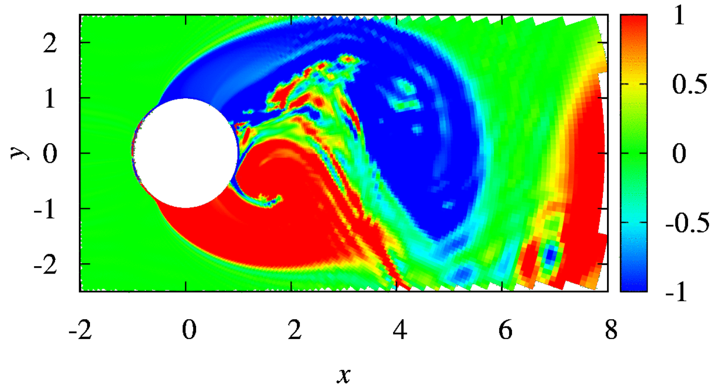

(b)

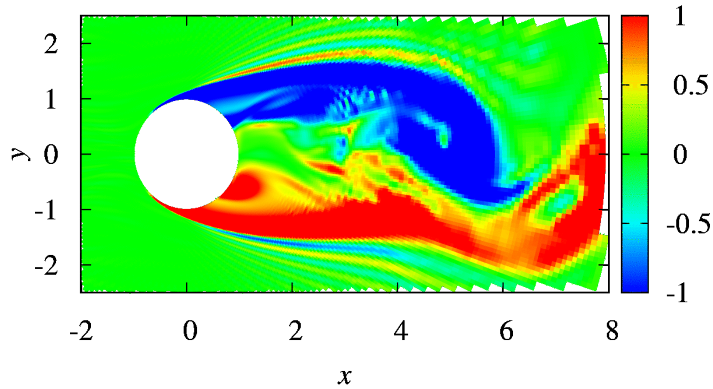

Fig 3.26: (Color online) Vorticity distribution at $Re = 3900$ (LES): (a) solid case with wall-normal velocity; (b) Case B.

3.7 Summary and Conclusions

Flow around a circular cylinder having porous surface of uniform thickness, permeability and porosity has been investigated by means of DNS and LES. Parametric study using two-dimensional computation at $Re = 1000$ defines the most effective set of porous media properties. With these properties, detailed flow modification is studied at $Re = 100, 1000, 3900$ and 1.0×10^5. The porous surface is found to increase the drag regardless of the Reynolds number: the drag increase is more pronounced at lower Reynolds number. On the other hand, the porous surface has an effect to suppress the lift fluctuation: the effect is larger at higher Reynolds number.

At $Re = 1000$, it is shown that the unsteadiness of the flow field is suppressed by the porous media: the surface pressure fluctuation is suppressed and the vortical structure of shear layer becomes more two-dimensional as compared to the fully three-dimensional structure in the solid case. Such stabilization effect is found to be clearer at higher Reynolds number. Particularly at $Re = 1.0 \times 10^5$ the RMS of lift coefficient nearly vanishes and the flow field becomes symmetric as has been observed in the experimental study of Sueki (2010).

These flow modifications are explained in terms of slip velocity and fluid energy. The shear and the vorticity near the surface are weakened by the slip velocity. The fluid that enters into the porous media loses its energy due to strong dissipation and the resultant low-energy fluid is ejected from the downstream side of the porous surface. A stable shear layer is likely to be formed by the combination of these two effects.

In the present study, only four different Reynolds numbers are investigated: the case at $Re = 100$ represents the two-dimensional laminar flow regime, and other three cases at $Re = 1000$, 3900, and 1.0×10^5 are all in the subcritical regime. From the present results, however, we can at least conjecture the following effects at higher Reynolds numbers. First, growth of instability in the boundary and shear layers would be delayed by the porous surface; hence the critical Reynolds number for laminar-to-turbulent transition would be shifted up. Even in the fully turbulent regime, the wide low energy region would be created in the wake and the fluctuations of flow field would be eliminated. As for the thickness of porous layer, two different thicknesses were studied and found that the thicker porous layer is more effective in reducing the lift fluctuations. However, an important question is still open: “What is the critical thickness to eliminate the lift fluctuations?” More detailed investigation on the dependency on the Reynolds number and the thickness of porous layer is left as future work.

Chapter 4

Active feedback control based on energy dissipation

4.1 Background

The theoretical study by Fukagata *et al.* (2009) suggests that for flows in a straight or a constant-curvature duct, the state of the lowest total power (i.e., the summation of the pumping power and the actuation power) is achieved when the flow takes the Stokes flow profile. Although it has not been proved previously, we can hypothesize that the same should hold for external flows such as a flow around a circular cylinder. Although such a lower bound has not been proved for an external flow, such as a circular cylinder, it is still common that the energy dissipation rate should be the most proper quantity to be reduced by an active control. Intuitively speaking, the ultimate state may be a state with no energy dissipation, where all the strain will vanishes, leading to no frictional or pressure drag; the unsteadiness of flow and the associated aerodynamic noise will also vanish.

Among the recent studies, the study on drag reduction of flow around a circular cylinder using suboptimal control by Min & Choi (1999) is of great importance in the sense that a practical control law can be derived on a solid theoretical basis. Although the optimal control, which attempts to minimize or maximize a cost function in a relatively long time horizon, is theoretically more rigorous, it usually requires a high computational cost to iteratively solve the forward and the adjoint equations (Kim & Bewley 2007). In contrast, the suboptimal control attempts to minimize or maximize a cost function in a relatively short time horizon, by which the iterative computations are avoided.

As mentioned in the beginning, the objectives of of flow control are generally not only the stabilization of flow but also more physical requirements. In this thesis, the energy dissipation is especially focused on and attempted to reduce directly using the suboptimal control theory.

4.2 Identity between the energy dissipation in an infinite volume and the surface quantities

First, the mathematical relationship between the energy dissipation in an infinitely large volume and the surface quantities is derived.

We consider a uniform flow around a fixed circular cylinder of radius R, as shown in Fig. 2.1. The governing equations are the incompressible Navier-Stokes equation,

$$\frac{\partial \mathbf{u}}{\partial t} = -\nabla \cdot \left[\mathbf{u}\mathbf{u} + p\mathbf{I} - \frac{2}{Re}\mathbf{s} \right], \tag{4.1}$$

and the continuity equation,

$$\nabla \cdot \mathbf{u} = 0, \tag{4.2}$$

where $\mathbf{u}$ and p denote the velocity vectors and the pressure, respectively; $\mathbf{I}$ and $\mathbf{s}$ are the unit dyadic and the strain-rate tensor,

$$\mathbf{s} = \frac{1}{2}\left[\nabla\mathbf{u} + (\nabla\mathbf{u})^T \right]. \tag{4.3}$$

All quantities are made dimensionless by the fluid density ρ, the cylinder diameter, D, and the free-stream velocity, U_∞; the Reynolds number is defined as $Re = U_\infty D/\nu$, where ν denote the kinematic viscosity.

To derive the mathematical relationship, we consider a control volume as shown in Fig. 4.1. The cylinder is at rest in a uniform velocity of $\mathbf{U}_\infty = U_\infty \mathbf{e}_x$. We assume that the flow is controlled by a zero-net-flux blowing and suction continuously distributed over the surface; the surface velocity is $\mathbf{u}_s(\theta) = \phi(\theta)\mathbf{n}$. We also assume that the outer boundary, ∂V_2, is located infinitely far away from the cylinder surface, ∂V_1.

Consider the original problem. The cylinder is at rest in a uniform velocity of $\mathbf{U}_\infty = U_\infty \mathbf{e_x}$. The surface velocity is given by $\mathbf{u_s} = \phi_c \mathbf{n}$, where $\mathbf{n}$ is the unit normal vector.

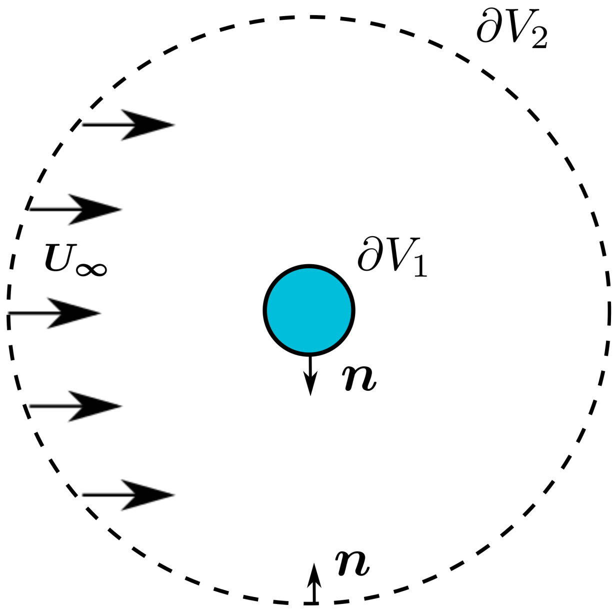

Fig 4.1: Flow configuration.

The key technic to derive the mathematical relationship is to introduce the deviation velocity from uniform velocity, i.e.,

$$\mathbf{u}' = \mathbf{u} - U_\infty \mathbf{e}_x. \tag{4.4}$$

Then the velocity deviation far from the cylinder is zero and the velocity de viation on the surface is

$$\mathbf{u}'_s = \mathbf{u}_s - U_\infty \mathbf{e}_x = \phi_c \mathbf{n} - U_\infty \mathbf{e}_x. \tag{4.5}$$

Note that the strain rate tensor based on the deviation velocity is identical to the original strain rate tensor, i.e.,

$$\mathbf{s}' = \mathbf{s}. \tag{4.6}$$

The energy equation for $\mathbf{u}'$ is derived by taking inner product between $\mathbf{u}'$ and Eq. (2.1) expressed by $\mathbf{u}'$, i.e.,

$$\frac{\partial\left(\frac{1}{2}\mathbf{u}' \cdot \mathbf{u}'\right)}{\partial t} = -\nabla \cdot \left[\frac{1}{2}(\mathbf{u}' \cdot \mathbf{u}')(\mathbf{u}' + U_\infty \mathbf{e}_x) + p\mathbf{u}'\right] + \frac{2}{Re}\mathbf{u}' \cdot \nabla \cdot \mathbf{s}'. \tag{4.7}$$

The global energy balance is obtained by integrating Eq. (4.7) in the volume. By using Gauss' divergence theorem and by noting $\mathbf{u}' = 0$ on ∂V_2, the integration of the first term in the right-hand-side becomes

$$
\begin{aligned}
&-\int_V \nabla\cdot\left[\frac{1}{2}(\mathbf{u}'\cdot\mathbf{u}')(\mathbf{u}'+U_\infty\mathbf{e}_x)+p\mathbf{u}'\right]dv \\
&=\int_{\partial V_1}\left[\frac{1}{2}(\phi^3-2\phi^2U_\infty\cos\theta)+(p\phi-pU_\infty\cos\theta)\right]ds.
\end{aligned}
\tag{4.8}
$$

By using some vector identities (Fukagata *et al.* 2009), the integration in the second term yields

$$
\begin{aligned}
&\int_V \mathbf{u}'\cdot\nabla\cdot\mathbf{s}'dv \\
&\quad=-\int_V \mathbf{s}':\mathbf{s}'dv-\int_{\partial V_1}\mathbf{n}\cdot\mathbf{s}'\cdot\mathbf{u}'ds \\
&\quad=-\int_V \mathbf{s}':\mathbf{s}'dv-\int_{\partial V_1}\mathbf{n}\cdot\mathbf{s}'\cdot(\phi\mathbf{n}-U_\infty\mathbf{e}_x)ds \\
&\quad=-\int_V \mathbf{s}:\mathbf{s}dv+\int_{\partial V_1}(\frac{1}{R}\phi^2)ds+U_\infty\int_{\partial V_1}\mathbf{n}\cdot\mathbf{s}\cdot\mathbf{e}_xds.
\end{aligned}
\tag{4.9}
$$

By rearranging the equations above, the global energy balance is expressed as

$$
\varepsilon=-\int_V\frac{\partial\left(\frac{1}{2}\mathbf{u}'\cdot\mathbf{u}'\right)}{\partial t}dv+U_\infty(F_{DP}+F_{DF}+F_{D\phi})+W_{id}, \tag{4.10}
$$

where the dissipation rate, ε, the pressure drag, F_{DP}, the friction drag, F_{DF}, and the additional drag due to the blowing and suction, $F_{D\phi}$, can be derived by taking an inner product of $\mathbf{e}_x$ and a volume integration of Eq. (2.1), as

$$
\varepsilon=\frac{2}{Re}\int_V\mathbf{s}:\mathbf{s}dv, \tag{4.11}
$$

$$
F_{DP}=\int_{\partial V_1}(-p\cos\theta)ds\ , \tag{4.12}
$$

$$
F_{DF}=\frac{2}{Re}\int_{\partial V_1}\mathbf{n}\cdot\mathbf{s}\cdot\mathbf{e}_xds \tag{4.13}
$$

and

$$
F_{D\phi}=\int_{\partial V_1}(-\phi^2\cos\theta)ds\ , \tag{4.14}
$$

respectively, and the ideal actuation power, W_{id}, are defined as

$$
W_{id}=\int_{\partial V_1}\left[(p+\frac{1}{2}\phi^2)\phi+\frac{2}{Re}\frac{1}{R}\phi^2\right]ds\ . \tag{4.15}
$$

The first term (i.e., the time derivative term) in Eq. (4.10) is exactly zero for a steady flow; it may also be neglected in general if we take a reasonable time-average, such as an average in one period of vortex shedding. Hence, the energy dissipation at the statistically steady (or quasi-steady) state, the reasonably time-averaged dissipation rate, $\overline{\varepsilon}$, is finally expressed by using the quantities on the surface only, as

$$\overline{\varepsilon} \;=\; U_\infty(F_{DP} + F_{DF}) + W_{id}, \tag{4.16}$$

Hence, the cost function which is identical to the energy dissipation in the process of minimization is given by

$$\begin{aligned} J \;=\; & \underbrace{U_\infty \int_{\partial V_1} -p\cos\theta ds}_{\text{pressure drag}} \\ & \underbrace{+U_\infty \frac{2}{Re}\int_{\partial V_1} \mathbf{n}\cdot\mathbf{s}\cdot\mathbf{e}_x ds}_{\text{friction drag}} \\ & \underbrace{-\int_{\partial V_1} \frac{1}{2}\phi_c^2\cos\theta ds}_{\text{additional drag due to blowing/suction}} \\ & \underbrace{+\int_{\partial V_1}\left[(p+\frac{1}{2}\phi_c^2)\phi_c + \frac{2}{Re}\frac{1}{R}\phi_c^2\right] ds}_{\text{actuation power}}. \end{aligned} \tag{4.17}$$

4.3 Suboptimal control

4.3.1 Control procedure

Since the suboptimal control theory by Min & Choi (1999) utilizes liniearization of governing equations through their temporal discretization, the control input depends on how they are discretized. In the present study, an explicit method is applied for the nonlinear term, and an implicit method is used for the linear terms. This discretization gives a temporally discretized form, i.e.,

$$\mathbf{u}^{n+1} + \Delta t_c \nabla p^{n+1} - \frac{\Delta t_c}{Re}\nabla^2 \mathbf{u}^{n+1} = \mathbf{E}^n, \tag{4.18}$$

where $\mathbf{E}^n$ denote explicit integrand and $\Delta t_c(\geq \Delta t)$ is an arbitrary control interval. The boundary condition is given as

$$
\begin{aligned}
u_r|_{r=R} &= \phi_c, \qquad u_r|_{r=\infty} = \cos\theta, \\
u_\theta|_{r=R} &= 0, \qquad u_\theta|_{r=\infty} = -\sin\theta.
\end{aligned}
\tag{4.19}
$$

In the following control law which minimizes the cost function (4.17) is derived by the following procedure of Min & Choi (1999).

The cost function J is minimized iteratively by using a gradient algorithm. Let the following relationship hold;

$$
{\phi_c}^{n+1^{l+1}} - {\phi_c}^{n+1^{l}} = -\rho \frac{\mathscr{D} J\left(\phi_c^{n+1^l}\right)}{\mathscr{D}\phi_c^{n+1}}, \tag{4.20}
$$

where

$$
\frac{\mathscr{D} J}{\mathscr{D}\phi_c}\tilde{\phi}_c = \lim_{h\to 0}\frac{J\left(\phi_c + h\tilde{\phi}_c\right) - J\left(\phi_c\right)}{h} \tag{4.21}
$$

is the fréchet differential and the superscripts n, l denote the control time step and the iteration step. The parameter ρ is negative for the present minimization cases, which is determined so as to satisfy given maximum input. Then, the following minimization process holds;

$$
J\left({\phi_c}^{n+1^{l+1}}\right) \approx J\left({\phi_c}^{n+1^{l}}\right) + \rho \frac{\mathscr{D} J\left(\phi_c^{n+1^l}\right)}{\mathscr{D}\phi_c^{n+1}}\left({\phi_c}^{n+1^{l+1}} - {\phi_c}^{n+1^{l}}\right), \tag{4.22}
$$

$$
J\left({\phi_c}^{n+1^{l+1}}\right) \approx J\left({\phi_c}^{n+1^{l}}\right) + \rho \left|\frac{\mathscr{D} J\left(\phi_c^{n+1^l}\right)}{\mathscr{D}\phi_c^{n+1}}\right|^2. \tag{4.23}
$$

Although the cost function is minimized through the iteration process, this is not practical for the actual use. But the effect of the iteration number of times is investigated by Choi *et al.* (1993), and it is shown that the cost function almost converges by only one iteration step. Therefore, present case allows one iteration. Thus the control input is given by

$$
\phi_c = -\rho \frac{\mathscr{D} J\left(\phi_c\right)}{\mathscr{D}\phi_c}. \tag{4.24}
$$

The gradient of a cost function J with respect to the control input ϕ_c, $\frac{\mathscr{D}J(\phi_c)}{\mathscr{D}\phi_c}$, is given by the following procedure. Let the J consist of a function denoted by $f(u_i, p)$

$$J = \int_0^{2\pi} f(u_i, p)|_{r=R} d\theta, \tag{4.25}$$

where u_i denotes the components of velocity vector. The fréchet differential of the cost function leads to

$$\begin{aligned} \frac{\mathscr{D}J(\phi_c)}{\mathscr{D}\phi_c}\tilde{\phi}_c &= \int_0^{2\pi} \left\{ \frac{\mathscr{D}f(\phi_c)}{\mathscr{D}\phi_c}\tilde{\phi}_c \right\}_{r=R} d\theta \\ &= \int_0^{2\pi} \left\{ \frac{\partial f}{\partial u_i} q_i + \frac{\partial f}{\partial p}\psi \right\}_{r=R} d\theta, \end{aligned} \tag{4.26}$$

where

$$q_i = \frac{\mathscr{D}u_i(\phi_c)}{\mathscr{D}\phi_c}\tilde{\phi}_c, \tag{4.27}$$

and

$$\psi = \frac{\mathscr{D}p(\phi_c)}{\mathscr{D}\phi_c}\tilde{\phi}_c. \tag{4.28}$$

The fréchet differential for u_i and p is solved analytically by using the discretized linear Navier-Stokes equation (4.18). The solutions are given in the Fourier space, i.e.,

$$\hat{q}_i(k) = \hat{\eta}_i(k)\hat{\tilde{\phi}}_c(k) \tag{4.29}$$

and

$$\hat{\psi}(k) = \hat{\Pi}(k)\hat{\tilde{\phi}}_c(k). \tag{4.30}$$

The functions $\hat{\eta}_i(k)$ and $\hat{\Pi}(k)$ are given respectively as

$$\hat{\Pi}_{k=0} = \hat{\Pi}_{r=R} = (const.), \tag{4.31}$$

$$\hat{\Pi}_{k\neq 0} = \frac{1}{\Delta t_c}\frac{1}{|k|}\frac{A}{B}\left(\frac{R}{r}\right)^{|k|}, \tag{4.32}$$

$$\hat{\eta}_{r,k=0} = \frac{K_1(mr)}{K1(mR)}, \tag{4.33}$$

$$\hat{\eta}_{r,k\neq 0} = \frac{A\,(R/r)^{|k|} + R|k|K_{|k|}(mr)}{Br}, \tag{4.34}$$

$$\hat{\eta}_{\theta,k=0} = 0\ , \tag{4.35}$$

$$\hat{\eta}_{\theta,k\neq 0} = \frac{i|k|}{k}\frac{-A(R/r)^{|k|} + \{R|k|K_{|k|}(mr) - mRrK_{|k|+1}(mr)\}}{Br}\ , \tag{4.36}$$

$$A = R|k|K_{|k|}(mR) - mR^2K_{|k|+1}(mR)\ , \tag{4.37}$$

$$B = 2|k|K_{|k|}(mR) - mRK_{|k|+1}(mR)\ , \tag{4.38}$$

$$m = \sqrt{\frac{Re}{\Delta t_c}}\ , \tag{4.39}$$

where k denote the wavenumber in the circumferential direction and $K_{|k|}(r)$ is the $|k|$-th order modified Bessel function of the second kind. Then, the inverse Fourier transform gives the convolution integral, i.e.,

$$q_i(\theta)|_{r=R} = \frac{1}{2\pi}\int_0^{2\pi} \eta_i(\theta-\tau)\tilde{\phi}_c(\tau)d\tau \tag{4.40}$$

and

$$\psi(\theta)|_{r=R} = \frac{1}{2\pi}\int_0^{2\pi} \Pi(\theta-\tau)\tilde{\phi}_c(\tau)d\tau. \tag{4.41}$$

The substitution of Eq. (4.40) and Eq. (4.41) into Eq. (4.42) yields

$$\begin{aligned}\frac{\mathscr{D}J(\phi_c)}{\mathscr{D}\phi_c}\tilde{\phi}_c &= \int_0^{2\pi}\frac{1}{2\pi}\int_0^{2\pi}\left\{\frac{\partial f}{\partial u_i}\eta_i(\theta-\tau) + \frac{\partial f}{\partial p}\Pi(\theta-\tau)\right\}_{r=R}\tilde{\phi}_c(\tau)d\tau d\theta \\ &= \int_0^{2\pi}\frac{1}{2\pi}\int_0^{2\pi}\left\{\frac{\partial f}{\partial u_i}\eta_i(\tau-\theta) + \frac{\partial f}{\partial p}\Pi(\tau-\theta)\right\}_{r=R} d\tau\tilde{\phi}_c(\theta)d\theta.\end{aligned} \tag{4.42}$$

Since Eq. (4.42) holds for an arbitrary $\tilde{\phi}_c(\tau)$, we obtain the following equation;

$$\frac{\mathscr{D}J(\phi_c)}{\mathscr{D}\phi_c} = \frac{1}{2\pi}\int_0^{2\pi}\left\{\frac{\partial f}{\partial u_i}\eta_i(\tau-\theta) + \frac{\partial f}{\partial p}\Pi(\tau-\theta)\right\}_{r=R} d\tau. \tag{4.43}$$

Applying (4.43) to the gradient of the cost function (4.17), we obtain

$$
\begin{aligned}
\frac{\mathscr{D}J}{\mathscr{D}\phi_c} = \frac{1}{2\pi}\int_0^{2\pi} \Bigg[& \underbrace{-\Pi(r,\tau-\theta)\cos\tau}_{\text{pressure drag}} \\
& + \underbrace{\frac{1}{Re}\frac{\partial}{\partial r}\{\eta_r(r,\tau-\theta)\cos\tau\} - \frac{1}{Re}\frac{\partial}{\partial r}\{\eta_\theta(r,\tau-\theta)\sin\tau\}}_{\text{friction drag}} \\
& \underbrace{-u_r\eta_r(r,\tau-\theta)\cos\tau}_{\text{additional drag due to blowing/suction}} \\
& + \underbrace{\{u_r\Pi(r,\tau-\theta) + p\eta_r(r,\tau-\theta)\} + \frac{3}{2}{u_r}^2\eta_r(r,\tau-\theta)}_{\text{actuation power}} \\
& \underbrace{-\frac{4}{Re}\frac{1}{R}u_r\eta_r(r,\tau-\theta)}_{\text{actuation power}} \Bigg]_{r=R} d\tau.
\end{aligned} \tag{4.44}
$$

As is clear from the equations above, the control input depends on the arbitrary control interval, Δt_c, which should be optimized to to obtain the best result. This point will be discussed in Sec. 4.5.1.

In the actual implementation, a temporal filter (i.e., an exponentially weighted moving average) is applied to the control input to avoid numerical instabilities, as $\phi_c^n = (7/10)\phi_c^F + (3/10)\phi_c^{n-1}$, where n is the time step and ϕ_c^F is the input obtained in Eq. (4.24).

4.4 Other controls for evaluation

In order to evaluate the performance of the present control law, suboptimal controls minimizing following cost functions J_1 and J_2 (Min & Choi 1999) are performed. J_1 is pressure drag acting on the cylinder, i.e.,

$$J_1 = \int_\partial -p\cos\theta R d\theta. \tag{4.45}$$

The cost function J_2 consists of difference between actual pressure and the potential pressure.

$$J_2 = \int_0^{2\pi} (p_t - p|_{r=R})^2 \, R d\theta, \tag{4.46}$$

In this study, these control laws are used to be compared with the present suboptimal control in terms of reduction of the energy dissipation rate. Hereafter, the control with the cost function J_1 and J_2 are referred to as 'J_2 -control' and 'J_2 -control', respectively.

4.4.1 Validation of suboptimal control procedure

The suboptimal control procedure in the numerical code is validated by comparing J_2-control with the past study (Min & Choi (1999)). The maximum input is set $\phi_{c_{max}} = 0.1$ and the Reynolds number is 100. Three different grid cases are tested, i.e., the present fine grid case (Case 1), a medium grid case (Case 2) and a coarse grid case (Case 3).

Figure 4.2 shows profiles of control input $u_r|_{r=R}(= \phi)_c$. Although it is difficult to compare accurately with each profiles since the control input is varying slowly, the profiles show fair agreements, such as the maximum blowing at the rear stagnation point ($\theta' = 0°$), local minimum on the top and bottom ($\theta' = 90°, 270°$) and the local maximum at the front stagnation point ($\theta' = 0°$).

In Fig. 4.3, the time evolutions of the drag coefficients in the case of $Re = 100$ and $\phi_{c_{max}} = 0.4$ are illustrated. Although there are discrepancies in the converged values between the present computations and the past one, the present control is considered working appropriately as shown in the time evolutional behavior such as abrupt drag decrease immediate after the control started at $t = 30T$ ($T = D/U_\infty$).

4.5 Results

4.5.1 Optimization of control model

As already alluded, the control performance depends on the arbitrary control interval Δt_c. Here, parametric studies are performed and the best Δt_c is obtained which maximize the control performance in terms of the energy dissipation.

The coefficient ρ in Eq. (4.24) is determined so as to have a given maximum amplitude,

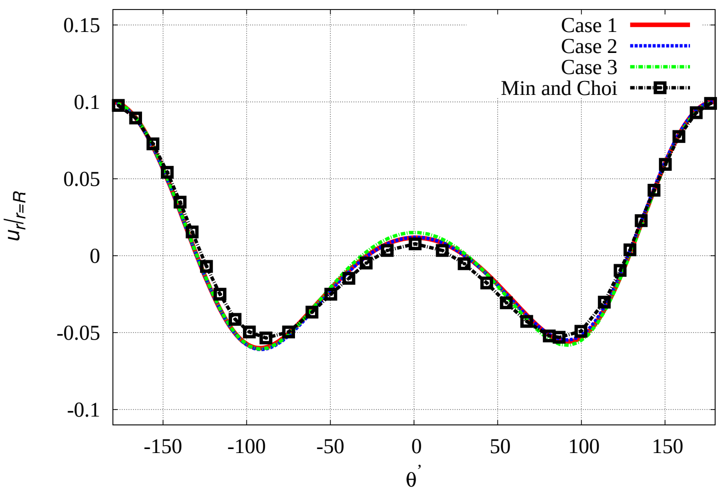

Fig 4.2: Comparison on the control input ($Re = 100$), $\phi_{c_{max}} = 0.1, \theta' = \pi - \theta$, case 1; $N_r \times N_\theta = 220 \times 256$, case 2; $N_r \times N_\theta = 125 \times 128$, case 3; $N_r \times N_\theta = 125 \times 64$.

$\phi_{\max}$. This amplitude is fixed to be $\phi_{\max} = 0.4$, where a complete suppression of vortex shedding is achieved by Min & Choi (1999). The Reynolds numbers are $Re = 100$ and $Re = 1000$. Although the actual flow at $Re = 1000$ should have three-dimensionality, two-dimensional simulations are performed to compare the control performance with $Re = 100$ cases in this step.

The dissipation rate is computed using Eq. (4.16) after the flow reaches its statistically steady state. For the computational domain of a finite size, a summation of the dissipation directly computed inside the computational domain, i.e., $(2/Re)\int_V(\mathbf{s} : \mathbf{s})dv$, and the energy flowing out from the outflow boundary should balance $\overline{\varepsilon}$ in Eq. (4.16). For the cases presented below, the error in this balance has been verified to be sufficiently small.

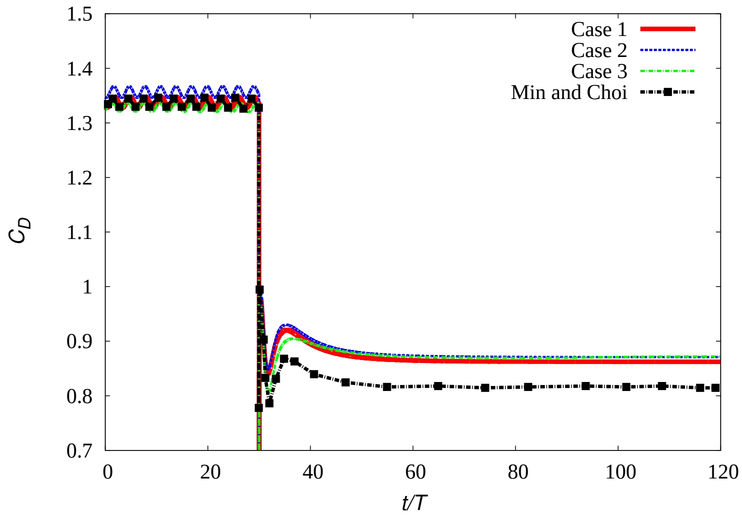

Fig 4.3: Comparison on the time traces of the drag coefficient (Re = 100), $\phi_{c_{max}} = 0.1, \theta' = \pi - \theta$, case 1; $N_r \times N_\theta = 220 \times 256$, case 2; $N_r \times N_\theta = 125 \times 128$, case 3; $N_r \times N_\theta = 125 \times 64$.

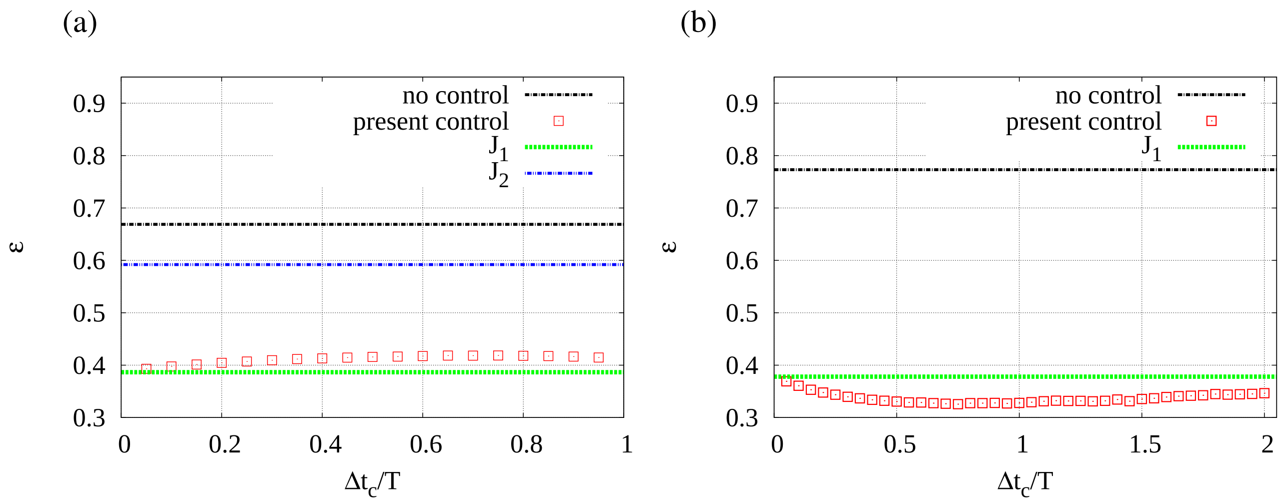

Fig 4.4: Parametric study: (a) Re = 100; (b) Re = 1000.

The control input given by Eqs.(4.44) (4.24) depends on the functions Π, η_r and η_θ. From Eq.(4.32), the function Π depends on Δt_c, and becomes larger by increasing Δt_c. Thus, in the limit $\Delta t_c \to 0$, the first term of Eq.(4.44) becomes dominative, and the control approaches the control of the cost function J_1. The contribution of Π becomes small when Δt_c becomes large, therefore the contributions of η_r and η_θ given by Eqs.(4.33)-(4.36) becomes relatively large. This means the increasing of the contribution of 'friction drag', 'additional drag due to the blowing/suction' and 'actuation power' terms in Eq.(4.44). However, the term of 'friction drag' corresponds to the term of 'pressure drag', which can be shown analytically in the formalization of Fourier transform. Therefore, increasing of Δt_c means increasing of the contribution of the 'additional drag due to the blowing/suction' and the 'actuation power' in the cost function (4.17). Briefly speaking, the total flow rate of blowing/suction of the control becomes smaller by increasing Δt_c.

The dissipation rate, $\bar{\varepsilon}$, computed for different values of $\Delta t_c/T$ at $Re = 100$ are shown in Fig. 4.4(a). Despite its larger drag reduction of the J_2-control, the energy dissipation is much larger than that of other controls due to the huge actuation power. When $\Delta t_c/T$ is small, $\bar{\varepsilon}$ takes a similar value to that of the control J_1, i.e., $\bar{\varepsilon} = 0.803$ at $Re = 100$ and $\bar{\varepsilon} = 0.355$ at $Re = 1000$. This is because the first term in Eq. (4.44) is dominant at $\Delta t_c/T \ll 1$; namely, the cost function is similar to that minimizing the pressure drag, i.e., Eq. (4.45). The dissipation rate at $Re = 100$ does not decrease for larger values of $\Delta t_c/T$; the statistics (not shown) suggest that the actuation power is increased as the increase of $\Delta t_c/T$, while the drag and the flow pattern are nearly unchanged. At $Re = 1000$, the simulation of the control J_2 does not conserve the energy balance noted above. But from the results at $Re = 100$, the effect of the control J_2 is expected to show higher energy dissipation than the control J_1 case due to its large actuation power. Contrast to $Re = 100$, an obvious reduction of dissipation rate is observed as the increase of $\Delta t_c/T$. The minimum value obtained at $\Delta t_c/T = 0.75$ corresponds to 13.2% reduction compared to the control J_1 case. In the followings, the more details are discussed at $\Delta t_c/T = 0.75$.

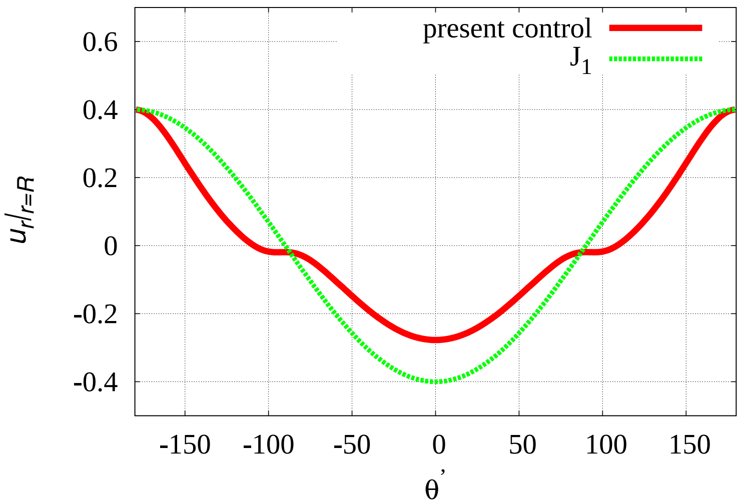

Fig 4.5: Velocity distribution on the wall (Re = 1000).

4.5.2 Details of control effects

Figure 4.5.2 shows the profile of control input, $\phi(\theta')$, i.e., the radial velocity on the cylinder surface, $u_r|_{r=R}$, where $\theta' = 180° - \theta$ denotes the angle from the front stagnation point. Although the velocity distribution in the present suboptimal control case is basically similar to that in the control J_1 case, we can observe that both the suction near the front stagnation point, $\theta' = 0°$ (where $\theta' = 180° - \theta$ denotes the angle from the front stagnation point), and the blowing in the rear half, $\theta' = 180°$, are weakened in different ways.

Figures 4.6 (a) and (b) show the time traces of the dissipation rate, ε, and the drag coefficient, C_D. In both cases, ε and C_D abruptly increase right after the control is turned on at $t/T = 15$ and monotonically decrease after that. As summarized in Table 4.1, the present suboptimal control results in higher reduction rates of drag and dissipation rate than those in the control of J_1 case.

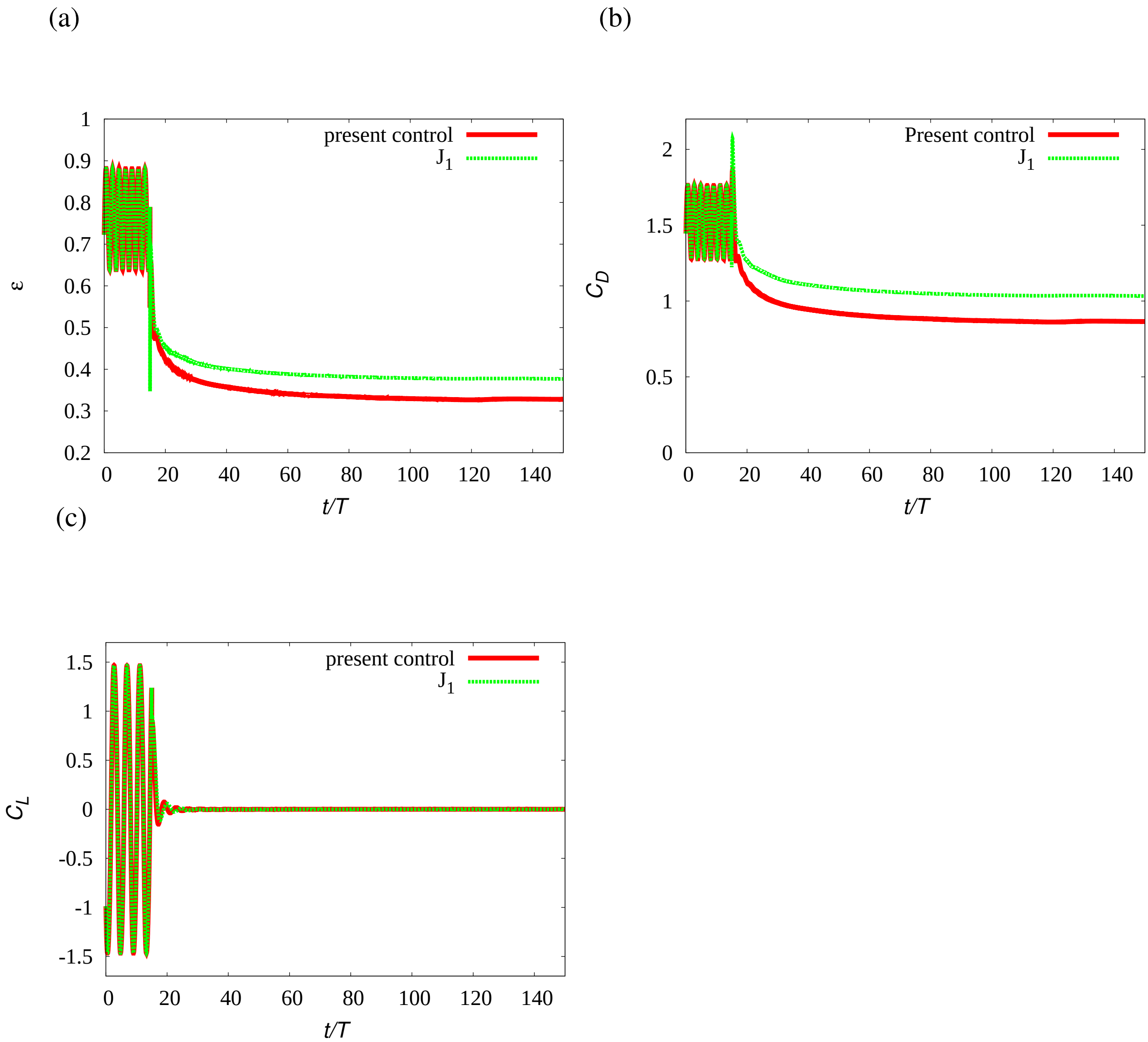

Fig 4.6: Time traces (Re = 1000): (a) energy dissipation, ε; (b) drag coefficient C_D; (c) lift coefficient C_L.

Figure 4.6 (c) shows the lift coefficient C_L. In both cases, oscillations immediately decay and eventually vanish, indicating that the flows become steady.

The mechanism of drag reduction can be explained by modifications of the pressure and the friction on the surface. Figures 4.7 (a) and (b) show distributions of the pressure coefficient, C_p, and the friction coefficient, C_f. The drag reduction is primarily due to the significant recovery of pressure in $20^\circ \leq \theta' \leq 180^\circ$, as compared to the uncontrolled case. As minor effects, the pressure coefficient near the front stagnation point is slightly decreased due to the non-zero velocity by the suction. A significant difference is also observed near 80°, although this difference contributes little to the pressure drag. As shown in Fig. 4.7 (b), in the controlled cases, the friction coefficient in the front half is increased due to the suction. The amount of increase is less in the present suboptimal control case due to a weaker suction.

The instantaneous energy dissipation rate fields are shown in Fig. 4.8. In the uncontrolled case, a large energy dissipation takes place in the shear layer involving vortex shedding. In the controlled cases, in contrast, the dissipation due to vortex shedding is disappeared. Although the dissipation fields in these the controlled cases are indistinguishable at a glance, the boundary layer in the present suboptimal control case is found to be slightly thicker than the control J_1 case due to the weaker suction.

(a)

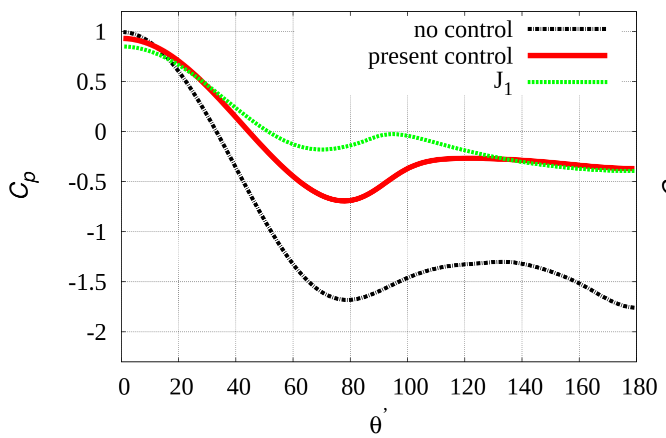

(b)

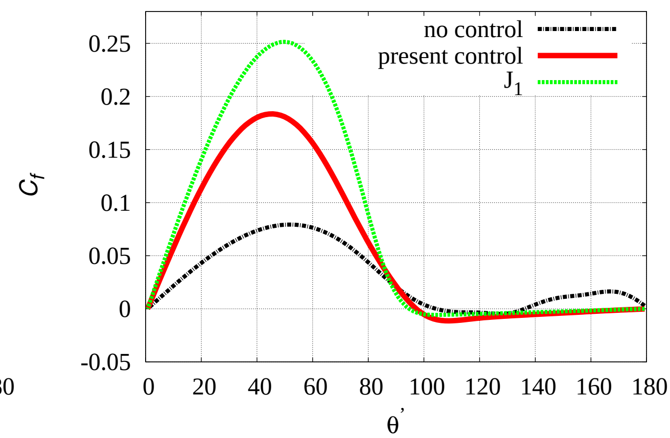

Fig 4.7: Pressure and friction coefficients on the cylinder surface (Re = 1000): (a) pressure coefficient, C_p; (b) friction coefficient, C_f.

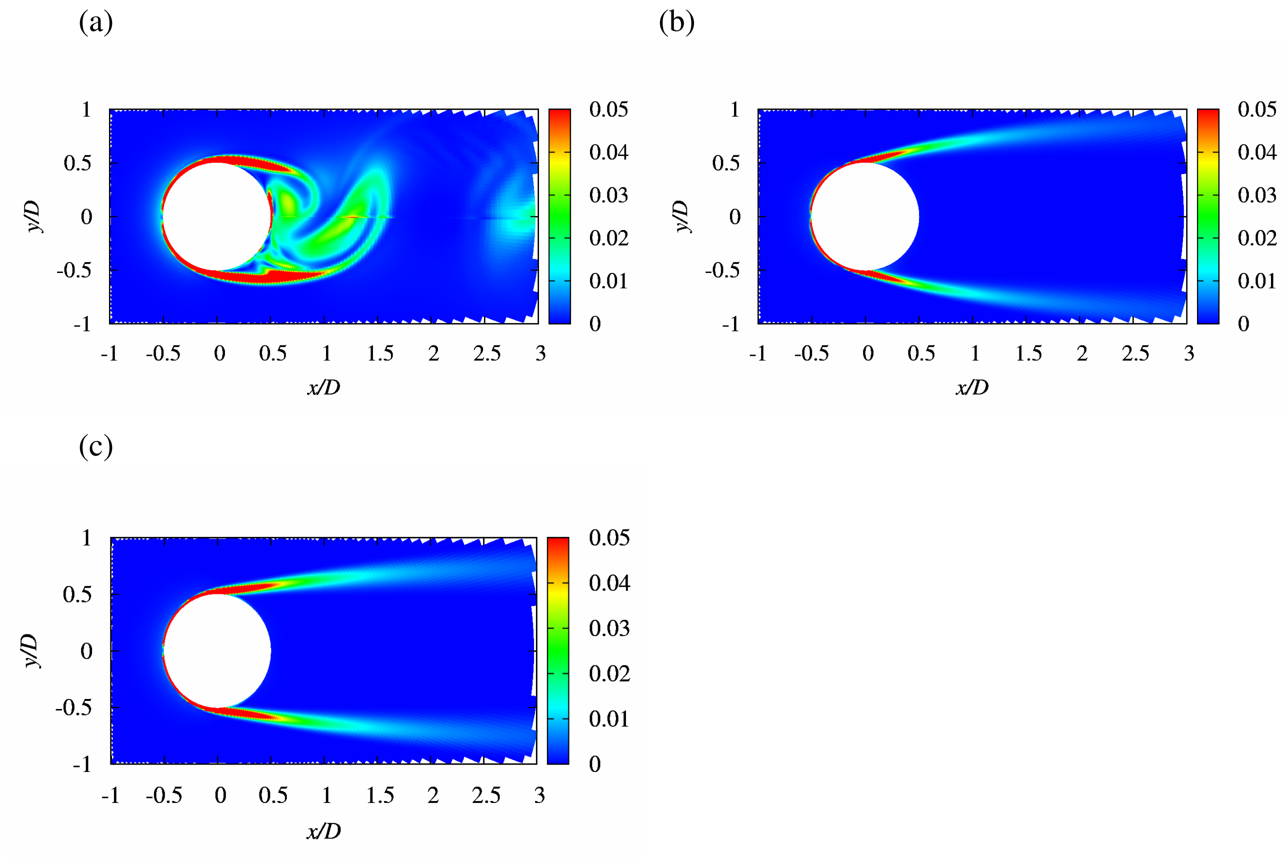

Fig 4.8: Instantaneous energy dissipation field (Re = 1000): (a) no control; (b) control J_1; (c) present suboptimal control.

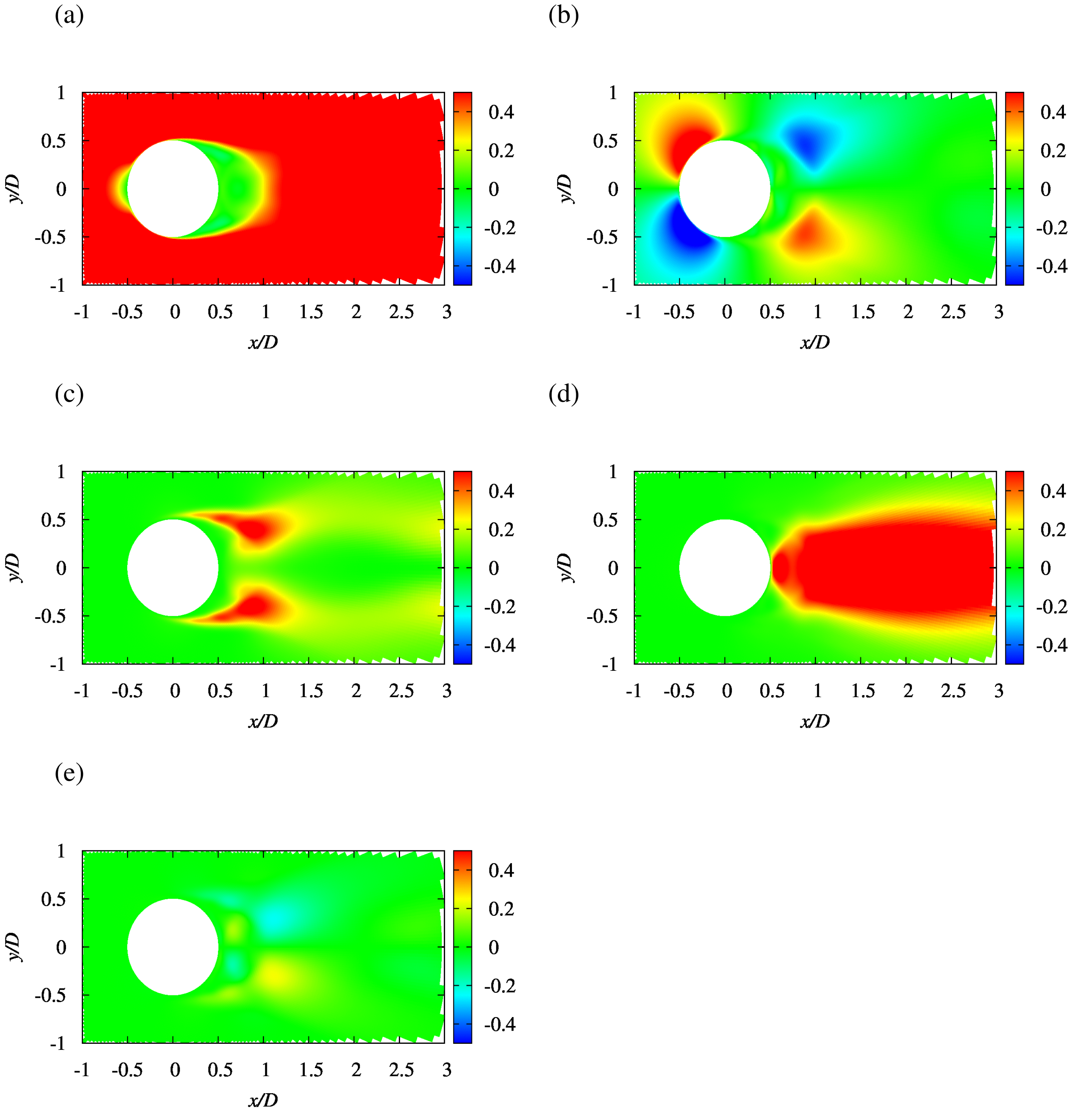

Fig 4.9: Mean velocity field (no control, Re = 1000): (a) $\overline{u}$; (b) $\overline{v}$; (c) $\overline{u'^2}$; (d) $\overline{v'^2}$; (e) $\overline{u'v'}$.

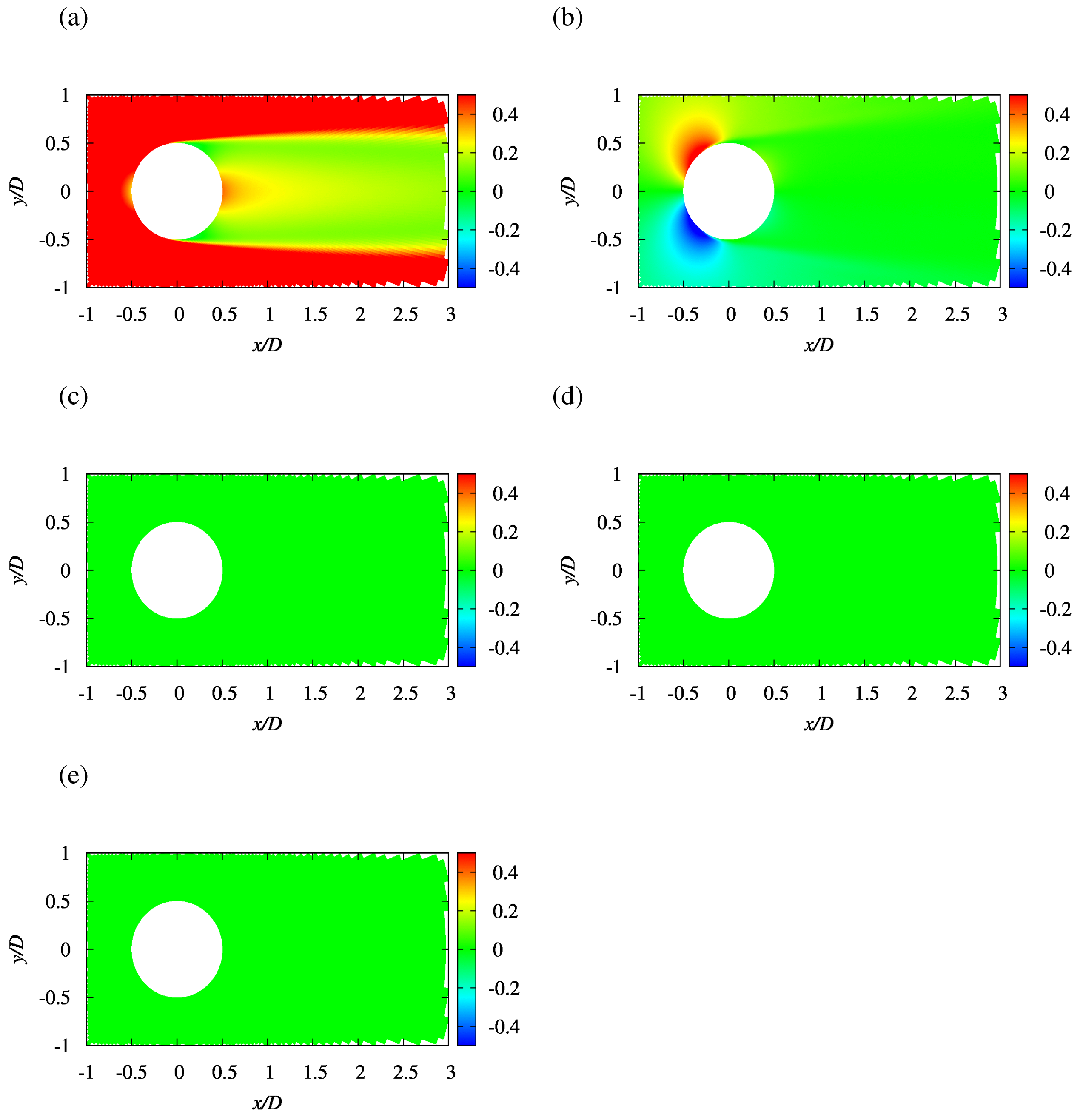

Fig 4.10: Mean velocity field (present suboptimal control, $Re = 1000$): (a) $\overline{u}$; (b) $\overline{v}$; (c) $\overline{u'^2}$; (d) $\overline{v'^2}$; (e) $\overline{u'v'}$.

Figures 4.9 (a)-(e) show mean streamwise velocity $\overline{u}$, mean lateral velocity $\overline{v}$, the components of the Reynolds stress, $\overline{u'^2}$, $\overline{v'^2}$, $\overline{u'v'}$, respectively and Figs.4.10 (a)-(e) are those of the controlled case. As shown in these, the controlled cases seem to be completely steady laminar flow. This state wold be maintained under special circumstances like this idealized computation. However, in practice, the inlet flow is not completely uniform and basically has arbitrary disturbances, and these disturbances may break the complete steady state in far downstream where control on the surface is no longer influenced.

Unsteady components of flow field are maintained only by mean velocity gradients. Figs. 4.10(a)(b) are mean streamwise and lateral velocity of the controlled case, respectively. Although all components of mean velocity gradients $\frac{\partial \overline{u_j}}{\partial x_i}$ are not zero, a component $\frac{\partial \overline{u}}{\partial y}$ is much greater than other components in the downstream shear layers. On the other hand, the production terms of unsteady components are respectively given as

$$P_{11} = -2\overline{u'u'}\frac{\partial \overline{u}}{\partial x} - 2\overline{u'v'}\frac{\partial \overline{u}}{\partial y}, \tag{4.47}$$

$$P_{22} = -2\overline{u'v'}\frac{\partial \overline{v}}{\partial x} - 2\overline{v'v'}\frac{\partial \overline{v}}{\partial y}, \tag{4.48}$$

$$P_{12} = -\overline{u'u'}\frac{\partial \overline{v}}{\partial x} - \overline{u'v'}\frac{\partial \overline{v}}{\partial y} - \overline{u'v'}\frac{\partial \overline{u}}{\partial x} - \overline{v'v'}\frac{\partial \overline{u}}{\partial y}. \tag{4.49}$$

P_{11} contains $\frac{\partial \overline{u}}{\partial y}$, and thus $\overline{u'^2}$ is developed in the downstream. While, P_{22} does not contain $\frac{\partial \overline{u}}{\partial y}$, therefore $\overline{v'^2}$ is not directly supplied energy from the mean shear $\frac{\partial \overline{u}}{\partial y}$. The component $\overline{v'^2}$ is developed by energy supply from $\overline{u'^2}$ via the redistribution term. As for P_{12}, $\frac{\partial \overline{u}}{\partial y}$ is included in the fourth term. $\overline{u'v'}$ is constantly supplied from $\frac{\partial \overline{u}}{\partial y}$ and developed in the downstream. An process of unsteadiness development holds. $\overline{v'^2}$ and $\overline{u'v'}$ are firstly developed by mean velocity gradient $\frac{\partial \overline{u}}{\partial y}$ with inlet disturbances and $\overline{u'^2}$ is developed by energy supply from $\overline{u'^2}$. From this supposition, It is considered that the order of energy is $\overline{u'v'} > \overline{u'^2} > \overline{v'^2}$.

4.5.3 Predetermined control

The results above imply that a similar control effect may also be achieved by a predetermined (i.e., open-loop) control, which does not require sensors. In this part, some of the

(a) (b)

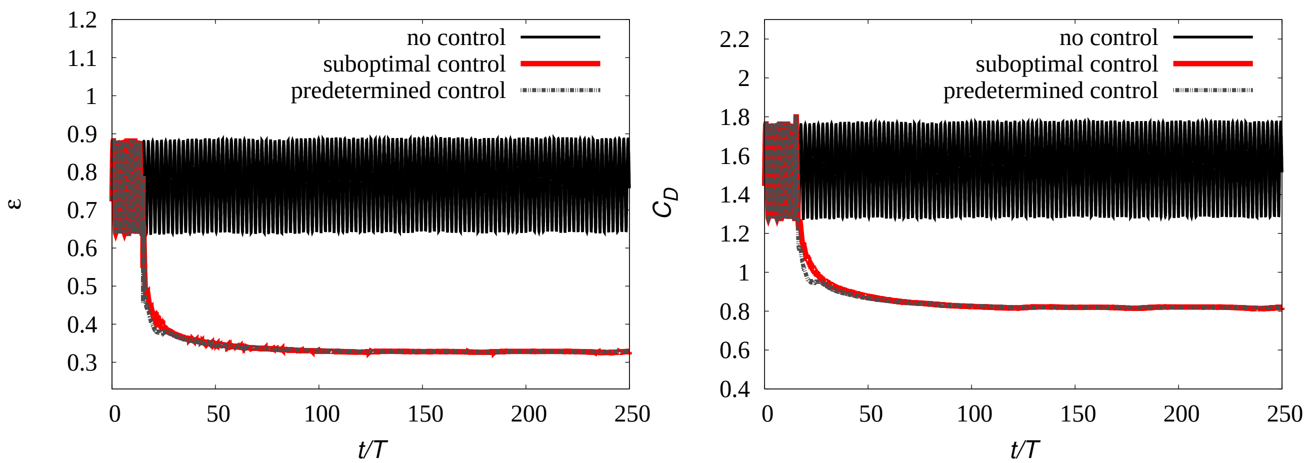

Fig 4.11: Time traces in the predetermined control case ($Re = 1000$): (a) energy dissipation, ε; (b) drag coefficient C_D.

results of a predetermined control are presented briefly. The steady control input is given by that obtained in the suboptimal control (Fig. 4.5.2).

In Fig. 4.11, the time traces of the energy dissipation rate and the drag coefficient are compared with those of the suboptimal control case. Although a small difference is observed immediately after the control is turned on, the variations in both cases are quite similar in the later period. An excellent agreement can also be observed in the mean surface pressure coefficients, as shown in Fig. 4.12.

These results conclude that a predetermined control minimizing the energy dissipation is possible and has almost the same effects as the suboptimal feedback control.

4.5.4 Energy efficiency

The ideal actuation power, W_{id}, is given by Eq. (4.15); thus, the upper bound of the actuation power (Min & Choi 1999) can be modified to read

$$W_a = \int_0^{2\pi} \left(\frac{1}{2}|\phi^3| + |p\phi| + \frac{2}{Re}\frac{1}{R}\phi^2 \right) R d\theta. \tag{4.50}$$

Denoting the drag in the uncontrolled case by F_{D0}, the ideal energy efficiency is given by

$$\eta_{id} = \frac{U_\infty \left(\overline{F_{D0}} - \overline{F_D} \right)}{\overline{W_{id}}}, \tag{4.51}$$

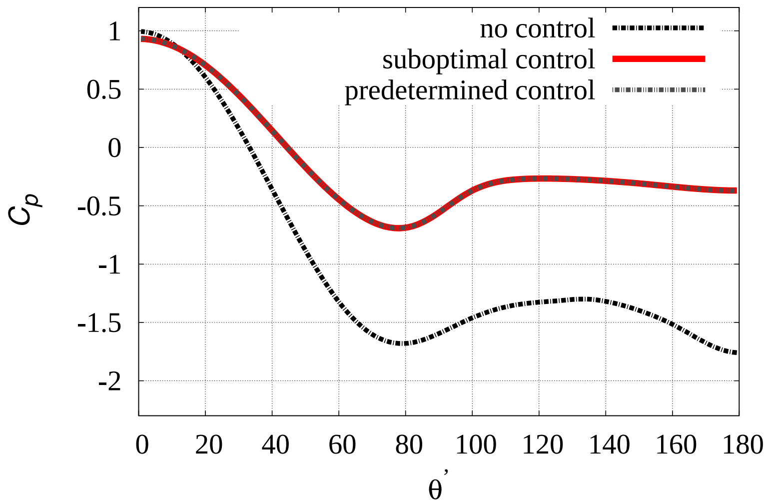

Fig 4.12: Surface pressure coefficient in the predetermined control case (Re = 1000).

where the overbar denotes the time average. Similarly, the lowest possible energy efficiency is

$$\eta_a = \frac{U_\infty\left(\overline{F_{D0}} - \overline{F_D}\right)}{\overline{W_a}}. \tag{4.52}$$

Note that the real energy efficiency takes a value between η_{id} and η_a (Min & Choi 1999). The mean drag coefficient, $\overline{C_D}$, the mean drag force, $\overline{F_D} = \overline{C_D}/2$ (since F_D is made dimensionless by U_∞ and D), the mean dissipation, $\overline{\varepsilon}$, the actuation powers $\overline{W_{id}}$, $\overline{W_a}$ and the energy efficiencies η_{id}, η_a are tabulated in Table 4.1.

The ideal power, $\overline{W_{id}}$, takes negative values in all cases, indicating that the control is achieved without an external power if the actuators themselves have a function that recycles the power received from the flow. This is what is meant by the negative values of ideal power and efficiency. In an energetic point of view, one gains profit if the energy efficiency is greater than unity. The lowest energy efficiency, η_a, is slightly greater than unity in the control J_1 case. In contrast, it is far greater than unity in the present suboptimal and predetermined controls.

Table 4.1: Drag, input power, and energy efficiencies

	$\overline{C_D}$	$\overline{F_D}$	$\overline{\epsilon}$	$\overline{W_{id}}$	$\overline{W_a}$	η_{id}	η_a
No control	1.545	0.773	0.773				
Suboptimal control laws of Min & Choi (1999) J_1	1.037	0.518	0.378	−0.140	0.195	−1.804	1.296
Present suboptimal control $\Delta t_c/T = 0.75$	0.820	0.410	0.328	−0.082	0.124	−4.419	2.928
Present predetermined control	0.820	0.410	0.328	−0.082	0.124	−4.419	2.928
Localized predetermined control (Sec. V E)	0.940	0.470	0.367	−0.103	0.122	−2.945	2.479

4.5.5 Dependency on the control amplitude

So far, the control amplitude has been fixed at $\phi_{\max} = 0.4$ (made dimensionless by U_∞). Here, we examine different values of control amplitude, $\phi_{\max} = 0.1$, 0.2, 0.3, and 0.5, to investigate its dependency on the control effect.

Figure 4.13(a) shows the total energy dissipation in the optimum cases (with respect to the parameter $\Delta t_c/T$) at different control amplitudes. The results of J_1-control are also plotted for comparison. Compared to J_1-control, the energy dissipation is reduced more with the present control at larger control amplitudes ($\phi_{\max} \geq 0.3$), while it takes similar values at smaller amplitudes ($\phi_{\max} \leq 0.2$). This tendency can be explained by Eqs. (4.12)–(4.16). When the control amplitude is smaller, the contribution of $F_{D\phi}$ and W_{id} to the present cost function become smaller. Moreover, since the contribution of the friction F_{DF} is small at this Reynolds number, the contribution of the pressure drag F_{DP} is dominant. Therefore, the present cost function approaches the cost function J_1 at smaller control amplitudes.

The lowest possible energy efficiencies η_a at different control amplitudes are plotted in Fig. 4.13(b). The tendency of the energy efficiency is similar to that of the energy

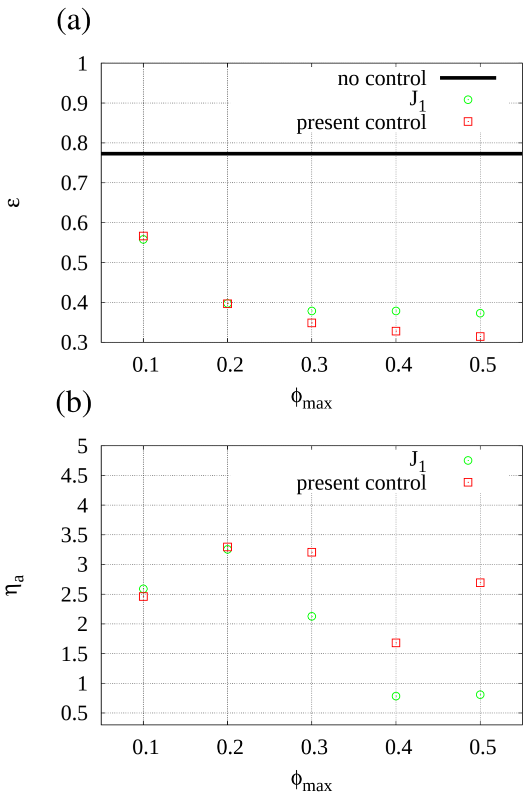

Fig 4.13: Dependency on the control amplitude $\phi_{\max}$ (Re = 1000): (a) energy dissipation $\overline{\varepsilon}$; (b) lowest possible efficiency η_a.

dissipation. When the control amplitude is small, η_a in the present control takes similar values to those in the J_1-control, while η_a in the present control takes higher values at $\phi_{\max} \geq 0.3$. Note that the present control guarantees the energy profit ($\eta_a > 1$) at any control amplitudes in contrast to the J_1-control at $\phi_{\max} = 0.4$ and 0.5.

4.5.6 Localized control

While the control was so far applied continuously on the entire cylinder surface, it is considered difficult to implement it in practice. Toward its practical implementation, here a predetermined control with localized actuation is considered.

The localized control profiles are obtained by fitting polynomials to the control input distribution shown in Fig. 4.15. The polynomial and its range are determined so that the zero net flux condition is satisfied. Here, as an example, a quadratic function, $\phi(\theta') = 0.4 - \theta'^2$, and a cubic function, $\phi(\theta') = -0.278 + 0.5252|\theta' - \pi|^3$, are chosen in the range of $-0.2\pi \leq \theta' \leq 0.2\pi$ and $0.77\pi \leq \theta' \leq 1.23\pi$, respectively.

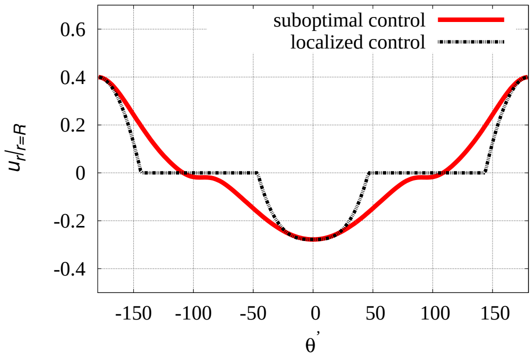

Fig 4.14: Velocity distribution on the wall (localized control, $Re = 1000$). The horizontal axis is the angle from the front stagnation point, i.e., $\theta' = 180° - \theta$.

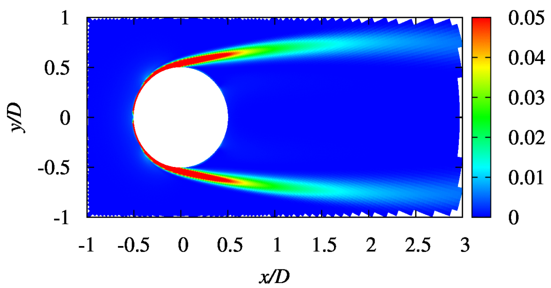

Fig 4.15: Instantaneous energy dissipation field (localized control, $Re = 1000$).

The instantaneous energy dissipation field is shown in Fig. 4.15. Even in the case where the actuation is applied locally (about 40% of the entire surface), the vortex shedding is found to disappear similarly to the continuous cases (Fig. 4.8).

The computed mean quantities are shown on the last line of Table I. The drag of the present localized control is found to be lower than those in the uncontrolled case and the J_1-control. Although the resultant energy dissipation of the localized control is higher than that of the present suboptimal and predetermined controls, the local control shows still better performance than the J_1-control on the entire surface. It is also found that the lowest energy efficiency η_a is higher than the present suboptimal and predetermined controls due to its lower actuation power $\overline{W_a}$. From above, it can be said that the present localized control works as efficiently as the continuous case.

Table 4.2: Drag, dissipation, input power, and energy efficiencies in three-dimensional flow (Re = 1000).

	$\overline{C_D}$	$\overline{F_D}$	$\overline{\varepsilon}$	$\overline{W_{id}}$	$\overline{W_a}$	η_{id}	η_a
No control	1.141	7.165	7.165				
J_1-control	1.037	6.512	4.748	−1.764	2.456	−0.370	0.266
Present predetermined control	0.820	4.121	3.092	−1.029	1.553	−1.959	1.298

4.5.7 Control effect in three-dimensional flow

Finally, the control effect in a three-dimensional flow around a circular cylinder at Re = 1000 is examined. To avoid the huge computational cost, the predetermined control input obtained in the two-dimensional flow is adopted. For comparison, the J_1-control.

Figure 4.16 shows the instantaneous energy dissipation fields. Similarly to the two-dimensional cases, both the J_1- and the present predetermined controls achieve complete suppression of vortex shedding, and the wake region of the J_1-control is found to be slightly wider in lateral direction than that of the present predetermined control.

The control effects are summarized in Table II. The present predetermined control results in a lower energy dissipation than the J_1-control. The drag $\overline{F_D}$ and the maximum possible power $\overline{W_a}$ of the present predetermined control are found to be lower than those of the J_1-control, which leads to a greater value of η_a. Note that η_a of the present predetermined control is greater than unity, while the J_1-control is less than unity; it indicates that the total power can be saved by the present predetermined control, while not by the J_1-control.

4.6 Summary

Blowing suction controls aiming at suppression of energy dissipation for flow around a circular cylinder have been conducted using two-dimensional numerical simulation.

To minimize the energy dissipation rate in an infinitely large volume, the proper cost function has been derived, which is expressed by the quantities on the surface. The cost function is then minimized by using the suboptimal control procedure of Min & Choi (1999).

Performance of the present suboptimal control has been assessed using two-dimensional numerical simulations at $Re = 100$ and $Re = 1000$. A parametric study for an arbitrary parameter contained in the suboptimal control law, Δt_c, has been conducted. Although no improvement is obtained at $Re = 100$, the present suboptimal control shows better performance at $Re = 1000$, than the suboptimal controls previously proposed. Suction near the front stagnation point and blowing in the rear half are weakened in different manners as compared to those in the suboptimal control targeting at pressure drag reduction.

A steady predetermined control based on the suboptimal control has also been performed. The results show that the energy dissipation and the drag can be reduced similarly to those in the suboptimal control.

In terms of the lowest possible efficiency, too, the present suboptimal and predetermined controls are shown to have much higher efficiency than the suboptimal control previously proposed.

The computations at different control amplitudes show that the advantage of the present control becomes clearer at higher control amplitudes, and this is explained by the form of the cost function. A similar control effect is also obtained with a localized control based on the obtained predetermined control. Finally, the present predetermined control is shown to work well in the three-dimensional flow at $Re = 1000$, too.

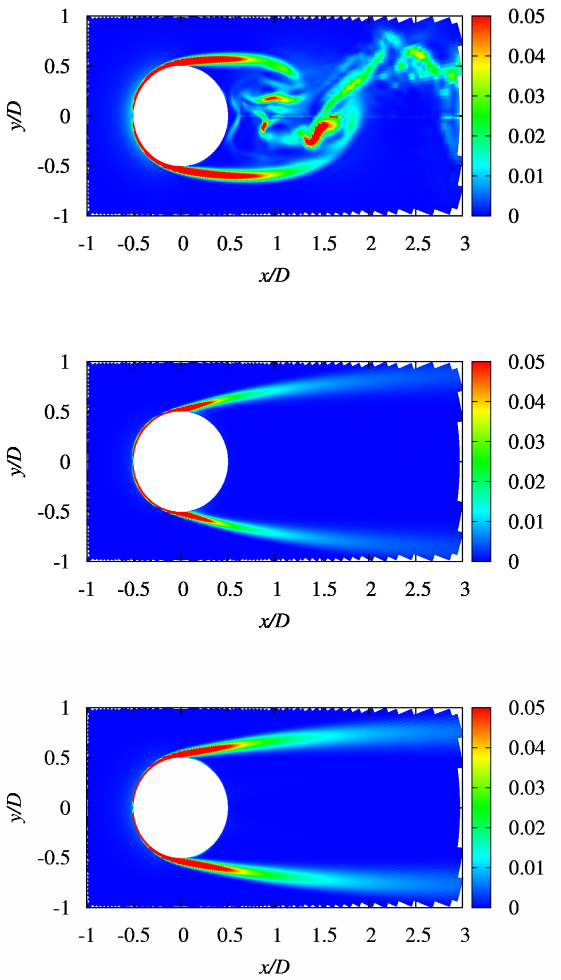

Fig 4.16: Instantaneous energy dissipation field (Re = 1000, three-dimensional): (a) no control; (b) J_1-control ; (c) present predetermined control.

Chapter 5

Summary and conclusions

The present thesis dealt with two numerical investigations about flow control around a circular cylinder, i.e., the passive flow control by porous surface, and the active flow control focusing on the energy dissipation by means of the suboptimal control theory. Throughout the both studies, a circular cylinder is chosen for the controlled object. The followings are the findings in each investigation, the summary and, the future prospects.

5.1 Passive control by porous surface

A numerical investigation of flow control by porous surface has been conducted using DNS and LES. The permeability and the porosity of porous surface were assumed to be uniform, and a macroscopic mean flow model was used for the flow inside the porous media. First, the best set of porosity and permeability was determined through a two-dimensional parametric test. In the three-dimensional simulation at $Re = 1000$, the porous surface suppressed the three-dimensionality and fluctuations near the surface in a case. The cases with different thickness of porous surface and different Reynolds numbers were also investigated, and it was found that the effect becomes more effective with thicker porous surfaces and at higher Reynolds numbers. Finally, the mechanism of the flow modification was explained by the slip velocity and the energy dissipation process from these dependencies.

5.2 Active control focusing on energy dissipation

Energy dissipation in the flow field was focused on. Introducing a deviation velocity from the uniform flow, a quantity identical to the energy dissipation in the flow field was derived through the energy balance equation about the deviation velocity. Energy dissipation was minimized through the minimization of the quantity given on the cylinder surface by suboptimal control theory. At $Re = 100$, the control inputs were relatively large, and the energy dissipation became larger than the previously proposed suboptimal control. In contrast, the control minimizing energy dissipation worked more effectively at $Re = 1000$, and the control reduced the energy dissipation more than previous suboptimal control scheme. The present control showed weaker suction in the front side and weaker blowing in the rear side. A open-loop predetermined control and its localized control were examined The predetermined control showed similar control effects to that of suboptimal control and the localized control also showed reasonable control effects. Furthermore the present suboptimal control is assessed with different control amplitudes and found that superiority of the present control becomes notable with larger control amplitudes. The control effects in three-dimensional flow is assessed using the predetermined control profile and it is shown that the present predetermined control still works better than previously proposed suboptimal control.

5.3 Remaining issues and prospects for general subjects

Use of porous media was a simple control method and had better situational adaptability. The porous surface suppressed the lift force fluctuations and the flow unsteadiness. These control effects are beneficial for various purposes, and future applications in various scenes are expected. However, this control increases the drag. It would be necessary to overcome this problem. In this thesis, the thickness, the permeability and the porosity of porous surface is assumed to be uniform. Variation of these properties inside the material and different configurations may be the way to overcome the drag increase. Further investigation for a more sophisticated control method is desired in the future.

The present investigation of control focusing on the energy dissipation dealt with only low Reynolds number cases. The present results shows the tendency that the control works more effectively at $Re = 1000$ than $Re = 100$; therefore, a better effect is expected at higher Reynolds numbers. The investigation at higher Reynolds numbers is desirable.

This thesis has treated a circular cylinder as the object to be controlled. As for the control by porous surface, how the porous media works in other geometries is an important concern. Throughout this thesis, we have seen that stabilization of wake is caused by stagnated low-energy fluid behind the cylinder. From this, it is presumed that wakes of objects having more complex geometries can be stabilized by creation of such a low energy fluid region. How to create such a low-energy fluid region would not be an easy problem, but the author is convinced that this control method is applicable for any objects.

In fact, the suboptimal control proposed in this thesis may not be a realizable control method. However, it was shown that some more practical versions (predetermined control and its localized version) were effective. The importance of investigation of feedback control is in this point: how to learn from the suggestion of feedback control. Keeping this point in mind, this thesis has provided the detailed informations of control method itself and flow modification. The author believes that the provided information will help future developments of passive and open-loop controls.

Appendix A

Appendix: Mathematical description of numerical model

A.1 Spatial descretization

The continuity equation (2.2) and the Navier-Stokes equation (2.1) are written using components of the cylindrical coordinate system as

$$\frac{1}{r}\frac{\partial(ru_r)}{\partial r} + \frac{1}{r}\frac{\partial(ru_\theta)}{\partial\theta} + \frac{\partial(ru_z)}{\partial z} = 0 \tag{A.1}$$

and

$$\frac{\partial u_r}{\partial t} = h_r + \frac{u_\theta^2}{r} - \frac{\partial p}{\partial r} + \frac{1}{Re}\left[\frac{1}{r}\frac{\partial}{\partial r}r\frac{\partial u_r}{\partial r} - \frac{u_r}{r^2} + \frac{1}{r^2}\frac{\partial^2 u_r}{\partial\theta^2} + \frac{\partial^2 u_r}{\partial z^2} - \frac{2}{r^2}\frac{\partial u_\theta}{\partial\theta}\right],$$

$$\frac{\partial u_\theta}{\partial t} = h_\theta + \frac{u_r u_\theta}{r} - \frac{\partial p}{\partial\theta} + \frac{1}{Re}\left[\frac{1}{r}\frac{\partial}{\partial r}r\frac{\partial u_\theta}{\partial r} - \frac{u_\theta}{r^2} + \frac{1}{r^2}\frac{\partial^2 u_\theta}{\partial\theta^2} + \frac{\partial^2 u_\theta}{\partial z^2} - \frac{2}{r^2}\frac{\partial u_r}{\partial\theta}\right], \tag{A.2}$$

$$\frac{\partial u_z}{\partial t} = h_z - \frac{\partial p}{\partial z} + \frac{1}{Re}\left[\frac{1}{r}\frac{\partial}{\partial r}r\frac{\partial u_z}{\partial r} + \frac{1}{r^2}\frac{\partial^2 u_z}{\partial\theta^2} + \frac{\partial^2 u_r}{\partial z^2}\right],$$

where the h_r, h_θ, h_z are convection terms:

$$h_r = -\frac{1}{r}\frac{\partial}{\partial r}(ru_r^2) - \frac{1}{r}\frac{\partial}{\partial\theta}(u_\theta u_r) - \frac{\partial}{\partial z}(u_z u_r),$$

$$h_\theta = -\frac{1}{r}\frac{\partial}{\partial r}(ru_r u_\theta) - \frac{1}{r}\frac{\partial}{\partial\theta}(u_\theta^2) - \frac{\partial}{\partial z}(u_z u_\theta), \tag{A.3}$$

$$h_z = -\frac{1}{r}\frac{\partial}{\partial r}(ru_r u_z) - \frac{1}{r}\frac{\partial}{\partial\theta}(u_\theta u_z) - \frac{\partial}{\partial z}(u_z^2).$$

Discretization scheme affects accuracy and instability of computations. The most important requirement for the spatial discretization of the convection terms is to conserve momentum and energy flux in the scheme. In the present simulations, the convection terms are discretized using the energy conservative second-order central differential which promises momentum conservation and higher energy conservations (Fukagata & Kasagi, 2002). The discretized convection terms are expressed as follows;

$$\begin{aligned}
h_{r,i+\frac{1}{2}jk} &= -\frac{1}{r_{i+\frac{1}{2}}\Delta r_{i+\frac{1}{2}}}\left[\frac{\overline{(ru_r)}^{i}_{i+1jk}\overline{u_r}^{i}_{i+1jk} - \overline{(ru_r)}^{i}_{ijk}\overline{u_r}^{i}_{ijk}}{\Delta r_{i+\frac{1}{2}}}\right] \\
&\quad -\left(\frac{\Delta r_{i+1}u_{\theta,i+1j-\frac{1}{2}k} + \Delta r_{i+1}u_{\theta,ij-\frac{1}{2}k}}{2\Delta r_{i+\frac{1}{2}}}\right)\overline{u_r}^{j}_{i+\frac{1}{2}j-\frac{1}{2}k}\Bigg] \\
&\quad -\frac{1}{\Delta z}\left[\left(\frac{r_{i+1}\Delta r_{i+1}u_{z,i+1jk+\frac{1}{2}} + r_i\Delta r_i u_{z,ijk+\frac{1}{2}}}{2\Delta r_{i+\frac{1}{2}}\Delta r_{i+\frac{1}{2}}}\right)\overline{u_r}^{k}_{i+\frac{1}{2}jk+\frac{1}{2}}\right. \\
&\quad \left. -\left(\frac{r_{i+1}\Delta r_{i+1}u_{z,i+1jk-\frac{1}{2}} + r_i\Delta r_i u_{z,ijk-\frac{1}{2}}}{2\Delta r_{i+\frac{1}{2}}\Delta r_{i+\frac{1}{2}}}\right)\overline{u_r}^{k}_{i+\frac{1}{2}jk-\frac{1}{2}}\right],
\end{aligned} \tag{A.4}$$

$$\begin{aligned}
h_{\theta,ij+\frac{1}{2}k} &= -\frac{1}{r_i\Delta r_i}\left[\overline{(ru_r)}^{j}_{i+\frac{1}{2}j+\frac{1}{2}k}\overline{u_\theta}^{i}_{i+\frac{1}{2}j+\frac{1}{2}k} - \overline{(ru_r)}^{j}_{i-\frac{1}{2}j+\frac{1}{2}k}\overline{u_r}^{i}_{i-\frac{1}{2}j+\frac{1}{2}k}\right] \\
&\quad -\frac{1}{r_i\Delta\theta}\left[\overline{(u_\theta)}^{j}_{i+\frac{1}{2}j+\frac{1}{2}k}\overline{u_\theta}^{j}_{ij+1k} - \overline{(u_\theta)}^{j}_{ijk}\overline{u_\theta}^{j}_{ijk}\right] \\
&\quad -\frac{1}{\Delta z}\left[\overline{(u_z)}^{j}_{ij+\frac{1}{2}k+\frac{1}{2}}\overline{u_\theta}^{k}_{ij+\frac{1}{2}k+\frac{1}{2}} - \overline{(u_z)}^{j}_{ij+\frac{1}{2}k-\frac{1}{2}}\overline{u_z}^{k}_{ij+\frac{1}{2}k-\frac{1}{2}}\right]
\end{aligned} \tag{A.5}$$

and

$$\begin{aligned}
h_{z,ijk+\frac{1}{2}} &= -\frac{1}{r_i\Delta r_i}\left[\overline{(ru_r)}^{k}_{i+\frac{1}{2}j+\frac{1}{2}k}\overline{u_\theta}^{i}_{i+\frac{1}{2}j+\frac{1}{2}k} - \overline{(ru_r)}^{k}_{i-\frac{1}{2}j+\frac{1}{2}k}\overline{u_r}^{i}_{i-\frac{1}{2}j+\frac{1}{2}k}\right] \\
&\quad -\frac{1}{r_i\Delta\theta}\left[\overline{(u_\theta)}^{k}_{i+\frac{1}{2}j+\frac{1}{2}k}\overline{u_\theta}^{j}_{ij+1k} - \overline{(u_\theta)}^{k}_{ijk}\overline{u_\theta}^{j}_{ijk}\right] \\
&\quad -\frac{1}{\Delta z}\left[\overline{(u_z)}^{k}_{ij+\frac{1}{2}k+\frac{1}{2}}\overline{u_z}^{k}_{ij+\frac{1}{2}k+\frac{1}{2}} - \overline{(u_z)}^{k}_{ij+\frac{1}{2}k-\frac{1}{2}}\overline{u_z}^{k}_{ij+\frac{1}{2}k-\frac{1}{2}}\right].
\end{aligned} \tag{A.6}$$

Where $\overline{\{\,\}}^{i}$, $\overline{\{\,\}}^{j}$ and $\overline{\{\,\}}^{k}$ are arithmetic averages for the radial, the circumferential and the spanwise directions, respectively.

Upstream differences are often used for stable computations. In the present study, the QUICK scheme (Leonard, 1979) is used to avoid early transition of the $Re = 1.0 \times 10^5$ cases caused by the dispersion error. The addition terms are described in the following expressions,

$$
\begin{aligned}
h_{r,i+\frac{1}{2}jk} = & -\frac{1}{r_{i+\frac{1}{2}}\Delta r_{i+\frac{1}{2}}}\left[-\overline{r_i u_{r_{ijk}}}^{i}\,\overline{\overline{u_{r_{ijk}}}}^{i} - \overline{|r_i u_{r_{ijk}}|}^{i}\,\overline{\overline{\overline{u_{r_{ijk}}}}}^{i}\right. \\
& \left. + \overline{r_{i+1} u_{r_{i+1jk}}}^{i}\,\overline{\overline{u_{r_{i+1jk}}}}^{i} + \overline{|r_{i+1} u_{r_{i+1jk}}|}^{i}\,\overline{\overline{\overline{u_{r_{i+1jk}}}}}^{i}\right] \\
& -\frac{1}{r_{i+\frac{1}{2}}\Delta\theta}\left[-\overline{u_{\theta_{ijk}}}^{i}\,\overline{\overline{u_{r_{ijk}}}}^{j} - \overline{|u_{\theta_{ijk}}|}^{i}\,\overline{\overline{\overline{u_{r_{ijk}}}}}^{j}\right. \\
& \left. + \overline{u_{\theta_{ij+1k}}}^{i}\,\overline{\overline{u_{r_{ij+1k}}}}^{j} + \overline{|u_{\theta_{ij+1k}}|}^{i}\,\overline{\overline{\overline{u_{r_{ij+1k}}}}}^{j}\right] \\
& -\frac{1}{\Delta z}\left[-\overline{u_{z_{ijk}}}^{i}\,\overline{\overline{u_{r_{ijk}}}}^{k} - \overline{|u_{z_{ijk}}|}^{i}\,\overline{\overline{\overline{u_{r_{ijk}}}}}^{k}\right. \\
& \left. + \overline{u_{z_{ijk+1}}}^{i}\,\overline{\overline{u_{r_{ijk+1}}}}^{k} + \overline{|u_{z_{ijk+1}}|}^{i}\,\overline{\overline{\overline{u_{r_{ijk+1}}}}}^{k}\right],
\end{aligned}
\tag{A.7}
$$

$$
\begin{aligned}
h_{\theta,ij+\frac{1}{2}k} = & -\frac{1}{r_i\Delta r_i}\left[-\overline{r_i u_{r_{ijk}}}^{j}\,\overline{\overline{u_{\theta_{ijk}}}}^{i} - \overline{|r_i u_{r_{ijk}}|}^{j}\,\overline{\overline{\overline{u_{\theta_{ijk}}}}}^{i}\right. \\
& \left. + \overline{r_{i+1} u_{r_{i+1jk}}}^{j}\,\overline{\overline{u_{\theta_{i+1jk}}}}^{i} + \overline{|r_{i+1} u_{r_{i+1jk}}|}^{j}\,\overline{\overline{\overline{u_{\theta_{i+1jk}}}}}^{i}\right] \\
& -\frac{1}{r_i\Delta\theta}\left[-\overline{u_{\theta_{ijk}}}^{j}\,\overline{\overline{u_{\theta_{ijk}}}}^{j} - \overline{|u_{\theta_{ijk}}|}^{j}\,\overline{\overline{\overline{u_{\theta_{ijk}}}}}^{j}\right. \\
& \left. + \overline{u_{\theta_{ij+1k}}}^{j}\,\overline{\overline{u_{\theta_{ij+1k}}}}^{j} + \overline{|u_{\theta_{ij+1k}}|}^{j}\,\overline{\overline{\overline{u_{\theta_{ij+1k}}}}}^{j}\right] \\
& -\frac{1}{\Delta z}\left[-\overline{u_{z_{ijk}}}^{j}\,\overline{\overline{u_{\theta_{ijk}}}}^{k} - \overline{|u_{z_{ijk}}|}^{j}\,\overline{\overline{\overline{u_{\theta_{ijk}}}}}^{k}\right. \\
& \left. + \overline{u_{z_{ijk+1}}}^{j}\,\overline{\overline{u_{\theta_{ijk+1}}}}^{k} + \overline{|u_{z_{ijk+1}}|}^{j}\,\overline{\overline{\overline{u_{\theta_{ijk+1}}}}}^{k}\right],
\end{aligned}
\tag{A.8}
$$

$$
\begin{aligned}
h_{z,ijk+\frac{1}{2}} \quad = \quad & -\frac{1}{r_i\Delta r_i}\Bigg[-\overline{r_i u_{r_{ijk}}}^{k}\,\overline{\overline{u_{z_{ijk}}}}^{i} - \overline{|r_i u_{r_{ijk}}|}^{k}\,\overline{\overline{\overline{u_{z_{ijk}}}}}^{i} \\
& +\overline{r_{i+1} u_{r_{i+1jk}}}^{k}\,\overline{\overline{u_{z_{i+1jk}}}}^{i} + \overline{|r_{i+1} u_{r_{i+1jk}}|}^{k}\,\overline{\overline{\overline{u_{z_{i+1jk}}}}}^{i}\Bigg] \\
& -\frac{1}{r_i\Delta\theta}\Bigg[-\overline{u_{\theta_{ijk}}}^{k}\,\overline{\overline{u_{z_{ijk}}}}^{j} - \overline{|u_{\theta_{ijk}}|}^{k}\,\overline{\overline{\overline{u_{z_{ijk}}}}}^{j} \\
& +\overline{u_{\theta_{ij+1k}}}^{k}\,\overline{\overline{u_{z_{ij+1k}}}}^{j} + \overline{|u_{\theta_{ij+1k}}|}^{k}\,\overline{\overline{\overline{u_{z_{ij+1k}}}}}^{j}\Bigg] \\
& -\frac{1}{\Delta z}\Bigg[-\overline{u_{z_{ijk}}}^{k}\,\overline{\overline{u_{z_{ijk}}}}^{k} - \overline{|u_{z_{ijk}}|}^{k}\,\overline{\overline{\overline{u_{z_{ijk}}}}}^{k} \\
& +\overline{u_{z_{ijk+1}}}^{k}\,\overline{\overline{u_{z_{ijk+1}}}}^{k} + \overline{|u_{z_{ijk+1}}|}^{k}\,\overline{\overline{\overline{u_{z_{ijk+1}}}}}^{k}\Bigg],
\end{aligned}
\tag{A.9}
$$

where double line $\overline{\overline{\{\}}}^{i}$ and $\overline{\overline{\overline{\{\}}}}^{i}$ denote weighted interpolation for each direction, i.e.,

$$
\overline{\overline{u_{r_{ijk}}}}^{i} = \frac{-u_{r_{i-\frac{3}{2}jk}} + 9u_{r_{i-\frac{1}{2}jk}} + 9u_{r_{i+\frac{1}{2}jk}} - u_{r_{i+\frac{3}{2}jk}}}{16} \tag{A.10}
$$

and

$$
\overline{\overline{\overline{u_{r_{ijk}}}}}^{i} = \frac{-u_{r_{i-\frac{3}{2}jk}} + 3u_{r_{i-\frac{1}{2}jk}} - 3u_{r_{i+\frac{1}{2}jk}} + u_{r_{i+\frac{3}{2}jk}}}{16}, \tag{A.11}
$$

respectively.

The body force terms are discretized by the ordinary second-order central differential as

$$
\left(\frac{u_\theta^2}{r}\right)_{i+\frac{1}{2}jk} = \frac{\Delta r_{i+1}\left(u^2_{\theta,i+1j+\frac{1}{2}k} + u^2_{\theta,i+1j-\frac{1}{2}k}\right) + \Delta r_i\left(u^2_{\theta,ij+\frac{1}{2}k} + u^2_{\theta,ij-\frac{1}{2}k}\right)}{4r_{i+1}\Delta r_{i+\frac{1}{2}}} \tag{A.12}
$$

and

$$
\left(\frac{u_r u_\theta}{r}\right)_{ij+\frac{1}{2}k} = \frac{\left(u_{r,i+\frac{1}{2}j+k} + u_{\theta,i+\frac{1}{2}jk} + u_{\theta,i-\frac{1}{2}j+1k} + u_{\theta,i-\frac{1}{2}jk}\right)u_{\theta,ij+\frac{1}{2}k}}{4r_i}. \tag{A.13}
$$

In a similar way, the diffusion terms are discretized by the second-order central differential;

$$
-\frac{2}{r^2}\frac{\partial u_\theta}{\partial\theta}\bigg|_{i+\frac{1}{2}jk} = -\frac{1}{r_{i+\frac{1}{2}}\Delta\theta}\left[\left(u_{\theta,i+1j+\frac{1}{2}k} - u_{\theta,i+1j-\frac{1}{2}k}\right) + \left(u_{\theta,ij+\frac{1}{2}k} - u_{\theta,ij-\frac{1}{2}k}\right)\right], \tag{A.14}
$$

$$-\frac{2}{r^2}\frac{\partial u_r}{\partial \theta}\bigg|_{ij+\frac{1}{2}k} = -\frac{1}{r_{i+\frac{1}{2}}\Delta\theta}\left[\left(u_{r,i+\frac{1}{2}j+1k} - u_{r,ij+\frac{1}{2}k}\right) + \left(u_{r,i-\frac{1}{2}j+1k} - u_{r,i-\frac{1}{2}jk}\right)\right], \tag{A.15}$$

$$\frac{1}{r}\frac{\partial}{\partial r}r\frac{\partial u_r}{\partial r}\bigg|_{i+\frac{1}{2}jk} = \frac{1}{r_{i+\frac{1}{2}}\Delta r_{i+\frac{1}{2}}}\left[r_{i+1}\frac{u_{r,i+\frac{3}{2}jk} - u_{r,i+\frac{1}{2}jk}}{\Delta r_{i+1}} - r_i\frac{u_{r,i+\frac{1}{2}jk} - u_{r,i-\frac{1}{2}jk}}{\Delta r_i}\right], \tag{A.16}$$

$$\frac{1}{r}\frac{\partial}{\partial r}r\frac{\partial u_\theta}{\partial r}\bigg|_{ij+\frac{1}{2}k} = \frac{1}{r_{i+\frac{1}{2}}\Delta r_i}\left[r_{i+\frac{1}{2}}\frac{u_{\theta,i+1j+\frac{1}{2}k} - u_{r,ij+\frac{1}{2}k}}{\Delta r_{i+\frac{1}{2}}} - r_{i-\frac{1}{2}}\frac{u_{\theta,ij+\frac{1}{2}k} - u_{\theta,i-1j+\frac{1}{2}k}}{\Delta r_{i-\frac{1}{2}}}\right], \tag{A.17}$$

$$\frac{1}{r}\frac{\partial}{\partial r}r\frac{\partial u_z}{\partial r}\bigg|_{ijk+\frac{1}{2}} = \frac{1}{r_{i+\frac{1}{2}}\Delta r_i}\left[r_{i+\frac{1}{2}}\frac{u_{\theta,i+1jk+\frac{1}{2}} - u_{r,ijk+\frac{1}{2}}}{\Delta r_{i+\frac{1}{2}}} - r_{i-\frac{1}{2}}\frac{u_{\theta,ijk+\frac{1}{2}} - u_{\theta,i-1jk+\frac{1}{2}}}{\Delta r_{i-\frac{1}{2}}}\right]. \tag{A.18}$$

A.2 Time integration

The time integration procedure and relevant solver are same as that used by Fukagata (2002). The accumulation of mass conservation error is avoided via the fractional step method. At each time step, the mass conservation error due to time integration is cancelled by solving appropriate pressure Poisson equation.

Denoting the spatially discretized continuity equation and Navier-Stokes equation in the symbolic form as

$$\vec{\mathcal{D}}\cdot\vec{u} = 0, \ \ \frac{\partial\vec{u}}{\partial t} = \vec{f} - \vec{\mathcal{G}}p + \frac{1}{Re}[\mathcal{V}\vec{u} + \vec{q}] \tag{A.19}$$

and

$$\frac{\partial\vec{u}}{\partial t} = \vec{f} - \vec{\mathcal{G}}p + \frac{1}{Re}[\mathcal{V}\vec{u} + \vec{q}], \tag{A.20}$$

where

$$\vec{u} = \begin{pmatrix} u_r \\ u_\theta \\ u_z \end{pmatrix}, \quad \vec{f} = \begin{pmatrix} h_r + \dfrac{u_\theta^2}{r} \\ h_\theta + \dfrac{u_r u_\theta}{r} \\ h_z \end{pmatrix}, \quad \vec{q} = \begin{pmatrix} -\dfrac{2}{r^2}\dfrac{\partial u_\theta}{\partial \theta} - \dfrac{u_r}{r^2} \\ +\dfrac{2}{r^2}\dfrac{\partial u_r}{\partial \theta} - \dfrac{u_\theta}{r^2} \\ 0 \end{pmatrix} \tag{A.21}$$

(A.22)

$$\vec{\mathcal{D}} = \begin{pmatrix} \dfrac{1}{r}\dfrac{\partial}{\partial r}r \\ \dfrac{1}{r}\dfrac{\partial}{\partial \theta} \\ \dfrac{\partial}{\partial z} \end{pmatrix}, \quad \vec{\mathcal{G}} = \begin{pmatrix} \dfrac{\partial}{\partial r} \\ \dfrac{1}{r}\dfrac{\partial}{\partial \theta} \\ \dfrac{\partial}{\partial z} \end{pmatrix}, \quad \mathcal{V} = \vec{\mathcal{D}} \cdot \vec{\mathcal{G}}, \quad \mathcal{L} = \vec{\mathcal{D}} \cdot \vec{\mathcal{G}}\cdot \tag{A.23}$$

The Crank-Nicolson method is applied to the diffusion terms and the low-storage third-order Runge-Kutta scheme is used for other terms (Ducowicz & Dvinsky 1992). The quantity as the next sub-time step is formally expressed as

$$\vec{u}^{\ell+1} = \vec{u}^{\ell} + \Delta t \left[\gamma^{\ell}(\vec{f} + \frac{1}{Re}\vec{q})^{\ell} + \zeta^{\ell}(\vec{f} + \frac{1}{Re}\vec{q})^{\ell-1} - \alpha^{\ell}\vec{\mathcal{G}}p^{\ell+1} + \alpha^{\ell}\frac{1}{Re}\frac{\mathcal{V}\vec{u}^{\ell} + \mathcal{V}\vec{u}^{\ell+1}}{2} \right], \tag{A.24}$$

where γ^{ℓ}, ζ^{ℓ} and α^{ℓ} are integration coefficients at ℓ-th time step (see Table. A.1). In the actual computation, an SMAC-like velocity-pressure coupling method is used as follows.

In the first step, a provisional velocity is calculated using the pressure at the present time step, n, by

$$\vec{u}^{*} = \vec{u}^{\ell} + \Delta t \left[\gamma^{\ell}(\vec{f} + \frac{1}{Re}\vec{q})^{\ell} + \zeta^{\ell}(\vec{f} + \frac{1}{Re}\vec{q})^{\ell-1} - \alpha^{\ell}\vec{\mathcal{G}}p^{\ell+1} + \alpha^{\ell}\frac{1}{Re}\frac{\mathcal{V}\vec{u}^{\ell} + \mathcal{V}\vec{u}^{*}}{2} \right]. \tag{A.25}$$

In the second step, the provisional velocity is corrected as

$$\vec{u}^{\ell+1} = \vec{u}^{*} - \alpha^{\ell}\Delta t\vec{\mathcal{G}}\Phi, \tag{A.26}$$

where Φ is the solution of the poisson equation

$$\mathcal{L}\Phi = \frac{1}{\alpha^{\ell}\Delta t}\mathcal{D} \cdot \vec{u}^{*}, \tag{A.27}$$

so that the corrected velocity satisfies the continuity equation.

Table A.1: Integration coefficients of Runge-Kutta/Crank-Nicolson scheme

substep, ℓ	1	2	3
γ	$8/15$	$5/12$	$3/4$
ζ	0	$-17/60$	$-5/12$
α	$8/15$	$2/15$	$1/3$

Since the residual between the desired velocity and the provisional velocity is

$$\vec{u}^{\ell+1} = \vec{u}^{*} - \alpha^{\ell}\Delta t\vec{\mathcal{G}}(p^{\ell+1} - p^{\ell}) + \frac{\alpha^{\ell}\Delta t}{2}\frac{1}{Re}\mathcal{V}(\vec{u}^{\ell+1} - \vec{u}^{*}), \tag{A.28}$$

the pressure gradient in the next substep is given by

$$\vec{\mathcal{G}}p^{\ell+1} = \vec{\mathcal{G}}p^{*} + \vec{\mathcal{G}}\Phi + \frac{\alpha^{\ell}\Delta t}{2}\frac{1}{Re}\mathcal{V}\vec{\mathcal{G}}\Phi. \tag{A.29}$$

If we use this pressure gradient for the correction, another Poisson equation has to be solved. But here, a first order approximation in time

$$p^{\ell+1} - p^{\ell} = \Phi. \tag{A.30}$$

is adopted to avoid the extra computation.

A.2.1 Solution for diffusion term

Since the Crank-Nicolson scheme is used for the time integration, athe matrix equation of (A.25) needs to be solved. In the present study an approximate factorization technique is used to reduce the computational cost.

The radial component of (A.25) is written using $\Delta u_r = u_r^{*} - u_r^{\ell}$ as

$$[\mathbf{I} - \beta(\mathbf{V}_{rr} + \mathbf{V}_{r\theta} + \mathbf{V}_{rz})]\Delta\mathbf{u_r} = \mathbf{e}_r, \tag{A.31}$$

where

$$\beta = \frac{\alpha^{\ell}\Delta t}{2}, \tag{A.32}$$

and

$$V_{rr,i+\frac{1}{2}jk} = \left.\frac{1}{r}\frac{\partial}{\partial r}r\frac{\partial}{\partial r}\right|_{i+\frac{1}{2}jk}, \quad V_{r\theta,i+\frac{1}{2}jk} = \left.\frac{1}{r^2}\frac{\partial^2}{\partial\theta^2}\right|_{i+\frac{1}{2}jk}, \quad V_{rz,i+\frac{1}{2}jk} = \left.\frac{1}{r^2}\frac{\partial^2}{\partial z^2}\right|_{i+\frac{1}{2}jk}, \tag{A.33}$$

$$e_{r,i+\frac{1}{2}jk} = \Delta t \left[\gamma^\ell (f_r + \frac{1}{Re} q_r)^\ell + \zeta^\ell (f_r + \frac{1}{Re} q_r)^{\ell-1} - \alpha^\ell \mathcal{G}_r p^{\ell+1} + \alpha^\ell \frac{1}{Re} \mathcal{V} u_r^\ell \right] \Bigg|_{i+\frac{1}{2}jk}. \quad \text{(A.34)}$$

(A.31) is approximated by

$$(\mathbf{I} - \beta \mathbf{V}_{rr})(\mathbf{I} - \mathbf{V}_{r\theta})(\mathbf{I} - \mathbf{V}_{rz}) \Delta u_r = \mathbf{e}_r, \quad \text{(A.35)}$$

and this matrix equation is solved with the tri-diagonal matrix algorithm (TDMA).

Due to the cyclic boundary condition in the radial and the circumferential directions, $(\mathbf{I} - \beta \mathbf{V}_{rr})$ and $(\mathbf{I} - \mathbf{V}_{r\theta})$ in the factorized matrix equation (A.35) has the form of cyclic tridiagonal matrix and is represented as

$$\mathbf{A} \equiv \mathbf{I} - \beta \mathbf{V} = \begin{bmatrix} b_1 & c_1 & & & a_1 \\ a_2 & b_2 & c_2 & & \\ & \ddots & \ddots & \ddots & \\ & & a_{N-1} & b_{N-1} & c_{N-1} \\ c_N & & & a_N & b_N \end{bmatrix}. \quad \text{(A.36)}$$

A tridiagonal matrix equation,

$$\mathbf{A}\mathbf{x} = \mathbf{b}, \quad \text{(A.37)}$$

can be solved in the following process. Compute two tridiagonal matrix equations,

$$\begin{aligned} \mathbf{A^{(0)}} \mathbf{x^{(0)}} &= \mathbf{b^{(0)}} \\ \mathbf{A^{(0)}} \mathbf{x^{(1)}} &= \mathbf{b^{(1)}}, \end{aligned} \quad \text{(A.38)}$$

where

$$\mathbf{A^{(0)}} \equiv \mathbf{A} - \mathbf{b^{(1)}} \mathbf{b^{(0)T}} = \begin{bmatrix} 2b_1 & c_1 & & & a_1 \\ a_2 & b_2 & c_2 & & \\ & \ddots & \ddots & \ddots & \\ & & a_{N-1} & b_{N-1} & c_{N-1} \\ c_N & & & a_N & b_N + \dfrac{a_1 c_N}{b_1} \end{bmatrix} \quad \text{(A.39)}$$

and

$$\mathbf{b^{(0)}} = \begin{bmatrix} -b_1 \\ 0 \\ \vdots \\ 0 \\ c_N \end{bmatrix}, \quad \mathbf{b^{(1)}} = \begin{bmatrix} 1 \\ 0 \\ \vdots \\ 0 \\ -a_1/b_1 \end{bmatrix}. \quad \text{(A.40)}$$

Then, the solution of (A.37) is solved using Sherman-Morrison formula, as

$$\mathbf{x} = \mathbf{x^{(0)}} - \left[\frac{\mathbf{b^0} \cdot \mathbf{x^0}}{1 + \mathbf{b^0} \cdot \mathbf{x^0}} \right] \mathbf{x^{(1)}}. \quad \text{(A.41)}$$

The remaining equation having a form,

$$a_r \Delta u_{r,i-\frac{1}{2}\ j\ k} + b_r \Delta u_{r,i+\frac{1}{2}\ j\ k} + c_r \Delta u_{r,i-\frac{3}{2}\ j\ k} = e_r \Delta u_{r,i+\frac{1}{2}\ j\ k}, \tag{A.42}$$

has to be solved for the radial direction. Here a_r, b_r and c_r are the components of the matrix $(\mathbf{I} - \beta \mathbf{V_{rr}})$. Sine the boundary condition is given as

$$\Delta u_{r,\ N_r+\frac{1}{2}\ j\ k} = \Delta v_r, \tag{A.43}$$

the equation at the first point from the wall is written as

$$b_r \Delta u_{r,\frac{3}{2}\ j\ k} + c_r \Delta u_{r,\frac{5}{2}\ j\ k} = e_r \Delta u_{r,\frac{3}{2}\ j\ k}. - a_r \Delta u_{r,\frac{1}{2}\ j\ k}. \tag{A.44}$$

And using defined external boundary condition (i.e., uniform velocity at the inlet boundary and the convective velocity condition at the outlet boundary), the equation of $N - \frac{1}{2}$th component becomes

$$a_r \Delta u_{r,N-\frac{3}{2}\ j\ k} + b_r \Delta u_{r,N-\frac{1}{2}\ j\ k} = e_r \Delta u_{r,i+\frac{1}{2}\ j\ k} - c_r \Delta u_{r,i+\frac{1}{2}\ j\ k}. \tag{A.45}$$

A.2.2 Poisson equation solver

The three-dimensional problem of Poisson equation (A.27) is simplified to the one-dimensional problem by using the Fourier transform for the circumferential direction and the spanwise direction,

$$\Phi(r, \theta, z) = \sum_{m=0}^{N_\theta - 1} \sum_{n=0}^{N_z - 1} \hat{\Phi}_{mn}(r) \exp[m\theta + k_z z], \tag{A.46}$$

where

$$k_z = \frac{2\pi n}{L_z}. \tag{A.47}$$

The Poisson equation simplified to become

$$\frac{1}{r_i \Delta r_i} \left[r_{i+\frac{1}{2}} \frac{\hat{\Phi}_{i+1mn} - \hat{\Phi}_{imn}}{\Delta r_{1+\frac{1}{2}}} - r_{i-\frac{1}{2}} \frac{\hat{\Phi}_{imn} - \hat{\Phi}_{i-1mn}}{\Delta r_{1-\frac{1}{2}}} \right] - (k_\theta^2 + k_z^2)\hat{\Phi}_{imn} = \frac{1}{\alpha \Delta t} \widehat{\mathscr{D} \cdot \vec{u}^*_{imn}}, \tag{A.48}$$

where k_θ and k_z are the wave numbers of each component,

$$\begin{aligned} k_\theta^2 &= \frac{2[1 - \cos(m\Delta\theta)]}{(r\Delta\theta)^2}, \\ k_z^2 &= \frac{2[1 - \cos(k_z \Delta z)]}{(r\Delta z)^2}. \end{aligned} \tag{A.49}$$

The $(m,n) \neq (0,0)$ can be solved by a tridiagonal matrix solver. The singularity of $(m,n) = (0,0)$,

$$\frac{1}{r_i \Delta r_i}\left[r_{i+\frac{1}{2}}\frac{\hat{\Phi}_{i+100} - \hat{\Phi}_{i00}}{\Delta r_{1+\frac{1}{2}}} - r_{i-\frac{1}{2}}\frac{\hat{\Phi}_{i00} - \hat{\Phi}_{i-100}}{\Delta r_{1-\frac{1}{2}}}\right] = \frac{1}{\alpha \Delta t}\widehat{\mathscr{D} \cdot \vec{u}^{*}_{i00}}, \tag{A.50}$$

is removed by setting a "ground" pressure Φ_c.

A.3 Large eddy simulation

The flow structures at higher Reynolds number flows become extremely small as expressed by Kolmogorov length scale $l_k = \left(\nu^3 L/U^3\right)^{1/4}$. The grid numbers to resolve this fine scale structure increase in the order of $O(Re^{9/4})$, and it is impossible to conduct accurate DNS at $Re = 3900$ and $Re = 1.0 \times 10^5$. This problem is dealt with by using turbulence modeling. Although there are two main categories, the Reynolds average modeling (RANS) and the the large eddy simulation (LES), LES is adopted in the present thesis to realize instantaneous three-dimensional structures of controlled flow field.

Although there are various models for the sub-grid scale modeling, we adopt the Smagorinsky model (Smagorinsky 1963) for the case of $Re = 3900$ and the dynamic Smagorinsky model (Germano *et al.* 1991, lilly 1991) for the case of $Re = 1.0 \times 10^5$ which have shown good consistencies with experiments.

A.3.1 Governing equations and eddy viscosity assumption

LES models small scale structures of fluid motion and takes it into account to the large scale motion. The large scale motion computed on given grids is called grid scale (GS) component, while small scale motion to be modeled is called sub-grid scale (SGS) component. Grid scale component in a flow field is given by a filtering operation,

$$\overline{f}(x) = \int f(x')\overline{G}(x,x')dx', \tag{A.51}$$

where $\overline{G}(x,x')$ is a filtering function for spatial smoothing such as the box filter, the spectral cutoff filter and the Gaussian filter. The filtering operation to the continuity equation and the Navier-Stokes equations yield the filtered continuity equation and the filtered Navier-Stokes equations, which are written in tensor form, as

$$\frac{\partial \bar{u}_i}{\partial x_i} = 0, \tag{A.52}$$

$$\frac{\partial \overline{u}_i}{\partial t} + \frac{\partial}{\partial x_j}\overline{u}_i\overline{u}_j = -\frac{\partial \overline{p}}{\partial x_i} - \frac{\partial \tau_{ij}}{\partial x_j} + \frac{1}{Re}\frac{\partial \overline{S_{ij}}}{\partial x_j}. \tag{A.53}$$

Here $\overline{S}_{ij}$ is grid scale component of strain rate tensor written by

$$\overline{S}_{ij} = \frac{1}{2}\left(\frac{\partial \overline{u}_i}{\partial x_j} + \frac{\partial \overline{u}_j}{\partial x_i}\right), \tag{A.54}$$

and τ_{ij} is the SGS stress

$$\tau_{ij} = \overline{u_i u_j} - \overline{u}_i\overline{u}_j. \tag{A.55}$$

By the similarity to the molecular viscosity, the SGS stress is modeled using the eddy viscous assumption, by which the SGS stress is given by

$$\tau_{ij}^a = -2\nu_e \overline{S}_{ij}, \tag{A.56}$$

where

$$\nu_e = (C_s\Delta)^2|\overline{\mathbf{S}}| \tag{A.57}$$

and $|\overline{\mathbf{S}}|$ is norm of the GS strain rate tensor.

For the Smagorinsky model, the Smagorinsky coefficient C_s is an invariant. In the present simulations $C_s = 0.1$ is used, which is a common value used for the external flow. Since the boundary layers of the flows under consideration are laminar state, the sub-grid scale (SGS) turbulent stress should be zero near the cylinder surface. Therefore the van Driest damping function

$$f_s = 1 - \exp\frac{-y^+}{A^+} \tag{A.58}$$

is used to avoid undesirable estimation of SGS stresses, where $A^+ = 25$ is non dimensional constant, and y^+ is obtained from spatial average of friction on the cylinder surface.

A.3.2 Dynamic Smagorinsky model

Germano *et al.* (1991) focused on that the best Smagorinsky constant varies for different flow problems. Taking it into account, they invented the dynamic Smagorinsky model in which the Smagorinsky coefficient is optimized dynamically using information of the flow field.

The dynamic Smagorinsky model utilizes the test filtering,

$$\tilde{f}(x) = \int f(x')\widetilde{G}(x, x')dx', \tag{A.59}$$

which is defined in larger space than the grid filter. The test filter leads the filtered Navier-Stokes equation (A.53) to

$$\frac{\partial \widetilde{\overline{u}}_i}{\partial t} + \frac{\partial}{\partial x_j}\widetilde{\overline{u}}_i\widetilde{\overline{u}}_j = -\frac{\partial \widetilde{\overline{p}}}{\partial x_i} - \frac{\partial T_{ij}}{\partial x_j} + \frac{1}{Re}\frac{\partial \widetilde{\overline{S}}_{ij}}{\partial x_j}, \tag{A.60}$$

where T_{ij} is residual stress from the test filter given by

$$T_{ij} = \widetilde{\overline{u_i u_j}} - \widetilde{\overline{u}}_i\widetilde{\overline{u}}_j. \tag{A.61}$$

We introduce the Germano identity, L_{ij}, which reads

$$L_{ij} = \widetilde{\overline{u}_i\overline{u}_j} - \widetilde{\overline{u}}_i\widetilde{\overline{u}}_j. \tag{A.62}$$

From eq. (A.55) (A.61), L_{ij} is written by

$$L_{ij} = T_{ij} - \overline{\tau}_{ij}. \tag{A.63}$$

The eddy viscosity approximation leads τ_{ij} and T_{ij} to

$$\tau_{ij} - (\delta_{ij}/3)\tau_{kk} = -2C\overline{\Delta}^2|\overline{S}|\overline{S}_{ij} \tag{A.64}$$

and

$$T_{ij} - (\delta_{ij}/3)T_{kk} = -2C\widetilde{\overline{\Delta}}^2|\tilde{\overline{S}}|\tilde{\overline{S}}_{ij}. \tag{A.65}$$

Substitution eq. (A.65) into eq. (A.63), and multiplication of S_{ij} give a scalar quantity

$$L_{ij}\overline{S_{ij}} = -2C(\widetilde{\overline{\Delta}}^2|\tilde{\overline{S}}|\tilde{\overline{S}}_{ij}\overline{S_{ij}} - \overline{\Delta}^2\widetilde{|\overline{S}|\overline{S}_{ij}}\overline{S_{ij}}), \tag{A.66}$$

which yields the dynamic Smagorinsky coefficient

$$C(x_{ij}, t) = -\frac{1}{2} \frac{L_{kl}\overline{S}_{kl}}{\tilde{\overline{\Delta}}^2 |\tilde{\overline{S}}|\tilde{\overline{S}}_{mn}\overline{S}_{mn} - \overline{\Delta}^2 \widetilde{|\overline{S}|\overline{S}_{pq}}\overline{S}_{pq}}. \tag{A.67}$$

Then, the SGS stress is given by

$$\tau_{ij} = \frac{L_{kl}\overline{S}_{kl}}{(\tilde{\overline{\Delta}}/\overline{\Delta})^2 |\tilde{\overline{S}}|\tilde{\overline{S}}_{mn}\overline{S}_{mn} - \widetilde{|\overline{S}|\overline{S}_{pq}}\overline{S}_{pq}} |\overline{S}|\overline{S}_{ij}. \tag{A.68}$$

A.3.3 Lilly's modification

Introduce a second-order tensor M_{ij}

$$M_{ij} = \tilde{\overline{\Delta}}^2 |\tilde{\overline{S}}|\tilde{\overline{S}}_{ij} - \overline{\Delta}^2 \widetilde{|\overline{S}|\overline{S}_{ij}}. \tag{A.69}$$

Then, L_{ij} is rewritten as

$$L_{ij} = 2CM_{ij}. \tag{A.70}$$

Since L_{ij} has 5 independent components, it is impossible to determine one coefficient satisfying 5 different values. Lilly overcame this problem by introducing the least square method (Lilly 1991). Define a residual Q as

$$Q = (L_{ij} - 2CM_{ij})^2. \tag{A.71}$$

Lilly determined the coefficient C so as Q to be the local minimum;

$$C = \frac{1}{2} \frac{L_{ij}M_{ij}}{M_{ij}M_{ij}}. \tag{A.72}$$

The uncertainty of Germano's procedure is removed by this modification, but there still remains problem of numerical instability due to spatial variation of the value C.

A.3.4 Clipping treatments

In order to mitigate the problem of numerical instability, two additional treatments are used. The first treatment is an averaging of the dynamic coefficient for the spanwise direction

$$C = \frac{1}{2} \frac{\langle L_{ij}M_{ij} \rangle}{\langle M_{ij}M_{ij} \rangle}. \tag{A.73}$$

As the second treatment, a limit for the dynamic turbulent viscosity is used;

$$0 \leq \nu_e + \nu \leq 100\nu. \tag{A.74}$$

Here the computed eddy viscosity is limited so that the sum of kinematic viscosity and the eddy viscosity is positive and smaller than 100 times of the kinematic viscosity.

References

Anderson, E., Szewczyk, A., 1997. ”Effects of a splitter plate on the near wake of a circular cylinder in 2 and 3-dimensional flow configurations,” *Exp. Fluids* **23**, 161.

Arcas, A., Redekopp, L., 2004. ”Aspects of wake vortex control through base blowing/suction,” *Phys. Fluids* **16**, 452.

Baek, S., Sung, H. J., 1998. ”Numerical simulation of the flow behind a rotary oscillating circular cylinder,” *Phys. Fluids* **10**, 869.

Bearman, P. W., 1965. ”Investigation of the flow behind a two-dimensional model with a blunt trailing edge and fitted with splitter plates,” *J. Fluid Mech.* **21**, 241.

Bearman, P. W., Harve, J. K., 1993. ”Control of circular cylinder flow by the use of dimples,” *AIAA J.* **31**, 1753.

Bearman, P. W., Owen, J. C., 1998. ”Reduction of bluff-body drag and suppression of vortex shedding by the introduction of wavy separation lines,” *J. Fluids Struct.* **12**, 123.

Berger, E., 1967. ”Suppression of vortex shedding and turbulence behind oscillating cylinders,” *Phys. Fluids* **10**, 191.

Bergmann, M., Cordier, L., Brancher, J., 2005. ”Optimal rotary control of the cylinder wake using proper orthogonal decomposition reduced-order model,” *Phys. Fluids* **17**, 97.

Breuer, M., 2000. “A challenging test case for large eddy simulation: high Reynolds number circular cylinder flow,” *Int. J. Heat Fluid Flow* **21**, 648.

Bruneau, C. H., Mortazavi, I., 2004. “Passive control of the flow around a square cylinder using porous media,” *Int. J. Numer. Meth. Fluids* **46**, 415.

Bruneau, C., H., Mortazavi, I., 2006. “Control of vortex shedding around a pipe section using a porous sheath,” *Int. J. Offshore Polar Eng*. **16**, 90.

Choi, H., Temam, R., Moin, P., Kim, J., 1993. “Feedback control for unsteady flow and its application to the stochastic Burgers equation,” *J. Fluid. Mech*. **253**, 509.

Choi, H., Jeon, W.-P., Kim, J., 2008. ”Control of flow over a bluff body,” *Annu. Rev. Fluid Mech*. **40**, 113.

Choi, S., Choi, H., Kang, S., 2002. ”Characteristics of flow over a rotationally oscillating cylinder at low Reynolds number,” *Phys. Fluids* **14**, 2767.

Dalton. C., Xu, Y., Owen. J. C., 2001. ”The suppression of lift on a circular cylinder due to vortex shedding at moderate Reynolds numbers,” *J. Fluids Struct.* **15**, 617.

Delaunay, Y., Kaiktsis, L., 2001. ”Control of circular cylinder wakes using base mass transpiration,” *Phys. Fluids* **13**, 3285.

Dennis, S., Nguyen, P., Kocabiyik, S., 2000. ”The flow induced by a rotationally oscillating and translating circular cylinder,” *J. Fluid Mech.* **407**, 123.

Dukowicz, J. K., Dvinsky, A. S., 1992. “Approximate factorization as a higher order splitting for the implicit incompressible flow equations,” *J. Comput. Phys*. **102**, 336.

Ergun, S., 1952. “Fluid flow through packed columns ,” *Chem. Eng. Prog*. **48**, 89.

Ffowcs Williams, J., Zhao, B., 1989. ”The active control of vortex shedding,” *J. Fluids Struct.* **3**, 115.

Filler, J., Marston, J. P., Mih, W., 1991. ”Response of the shear layers separating from a circular cylinder to small-amplitude rotational oscillations,” *J. Fluid Mech.* **231**, 481.

Fujisawa, N., Takeda, G., Ike, N., 2004. ”Phase-averaged characteristics of flow around a circular cylinder under acoustic excitation control,” *J. Fluids Struct.* **19**, 151.

Fukagata, K., Kasagi, N., 2002. “Highly energy-conservative finite difference method for the cylindrical coordinate system,” *J. Comput. Phys*. **181**, 478.

Fukagata, K., “Development of DNS code for turbulent pipe flow,” THTLAB Internal Report, No. ILR-0104(Turbulence and Heat Transfer Laboratory, The Univ. of Tokyo, 2001), 62 pp.

Fukagata, K., Sugiyama, K., Kasagi, N., 2009. ”On the lower bound of net driving power in controlled duct flows,” *Physica D* **238**, 1082.

Germano, M., Piomelli, U., Moin, P., William, C. H., 1991. “A dynamic subgrid-scale eddy viscosity model,” *Phys. Fluids A* **3**, 1760.

Gerrard, J. H., 1965. “A disturbance-sensitive Reynolds number range of the flow past a circular cylinder,” *J. Fluid. Mech*. **22**, 187.

Gillies, E., 1998. ”Low-dimensional control of the circular cylinder wake,” *J. Fluid Mech.* **371**, 157.

Graham, W. R., Peraire, J., Tang, K. Y., 1999. ”Optimal control of vortex shedding using low-order models. Part II: model-based control,” *Int. J. Numer. Meth Eng*. **44**, 973.

He, J-W., Glowinski, R., Metcalfe, R., Nordlander, A., Periaux, J., 2000. ”Active control and drag optimization for flow past a circular cylinder. 1: oscillatory cylinder rotation,” *J. Comput. Phys.* **163**, 83.

Henderson, R. D., Karniadakis, G., 1995. “Unstructured Spectral Element Methods for Simulation of Turbulent Flows,” *J. Comput. Phys*. **7**, 2102.

Henderson, R. D., 1995. “Details of the drag curve near the onset of vortex shedding,” *Phys. Fluids* **122**, 191.

Hsu, C. T., Cheng, P., 1990. “Thermal dispersion in porous medium,” *Int. J. Heat Mass Transfer* **33**, 1587.

Huang, X., 1996. ”Feedback control of vortex shedding from a circular cylinder,” *Exp. Fluids* **20**, 218.

Hwang, J. Y., Yang, K. S., Sun. D. H., 2003. ”Reduction of flow-induced forces on a circular cylinder using a detached splitter plate,” *Phys. Fluids* **15**, 2433.

Jeon, S., Choi, J., Jeon, W-P., Choi, H., Park, J., 2004. ”Active control of flow over a sphere for drag reduction at a subcritical Reynolds number,” *J. Fluid Mech.* **517**, 113.

Jeon, S., Choi, H., 2010. ”Suboptimal feedback control of flow over a sphere,” *Int. J. Heat Fluid Flow* **31**, 208.

Jiménez, J., Uhlmann, M., Pinelli, A., Kawahara, G., 2001. “Turbulent shear flow over active and passive porous surfaces,” *J. Fluid Mech*. **442**, 89.

Kametani, Y., Fukagata, K., 2011. ”Direct numerical simulation of spatially developing turbulent boundary layer with uniform blowing or suction,” *J. Fluid Mech.* **681**,154.

Kametani, Y., Fukagata, K., 2012. ”Direct numerical simulation of spatially developing turbulent boundary layer for skin friction drag reduction by wall surface-heating or cooling,” *J. Turbulence* **13**, N34, 1.

Kasagi, N., Suzuki, Y., Fukagata, K., 2009. ”Microelectromechanical system-based feedback control of turbulence for skin friction reduction,” *Annu. Rev. Fluid Mech.* **41**, 231.

Kim, J. Choi, H., 2005. “Distributed forcing of flow over a circular cylinder,” *Phys. Fluids* **17**, 033103.

Kim, J., Bewley, Thomas R., 2007. ”A Linear Systems Approach to Flow Control,” *Annu. Rev. Fluid Mech* **39**,389.

Konstantinidis, E., Balabani, S., Yianneskis, M., 2005. ”The timing of vortex shedding in a cylinder wake imposed by periodic inflow perturbations,” *J. Fluid Mech.* **543**, 45.

Kravchenko, A. G., Moin, P., 2000. “Numerical studies of flow over a circular cylinder at $Re_D = 3900$,” *Phys. Fluids* **12**, 403.

Kwon, K., Choi, H., 1996. ”Control of laminar vortex shedding behind a circular cylinder using splitter plates,” *Phys. Fluids* **8**, 479.

Lee, S., Kim, H., 1997. ”The effect of surface protrusions on the near wake of a circular cylinder,” *J. Wind Eng. Ind. AeroDyn.* **69-71**, 351.

Leonard, B. P., 1979. “A stable and accurate convective modelling procedure based on quadratic upstream interpolation,” *Comput. Meth. Appl. Mech. Eng.*, **19**, 59.

Leu, T. S., Ho, C. M., 2000. ”Control of global instability in a nonparallel near wake,” *J. Fluid Mech.* **404**, 345.

Li, F., Aubry, N., 1991. ”Feedback control of a flow past a cylinder via transverse motion,” *Phys. Fluids* **15**, 2163.

Lilly, D. K., 1991. “A proposed modification of the Germano subgrid-scale closure method,” *Phys. Fluids A* **4**, 633.

Lin, J., Towfighi, J., Rockwell, D., 1995. ”Near-wake of a circular cylinder: control by steady and unsteady surface injection,” *J. Fluids Struct.* **9**, 659.

Martys, N. S., Chen, H., 1996. “Simulation of multicomponent fluids in complex three-dimensional geometries by the lattice Boltzmann method,” *Phys. Rev. E* **53**, 743.

Min, C., Choi, H., 1999. ”Suboptimal feedback control of vortex shedding at low Reynolds numbers,” *J. Fluid Mech*. **401**, 123.

Nehari, D., Armenio, V., Ballio, F., 2004. ”Three-dimensional analysis of the unidirec-tional oscillatory flow around a circular cylinder at low Keulegan-Carpenter and β numbers,” *J. Fluid Mech.* **520**, 157.

Norberg, C., 1987a. “Turbulence and Reynolds number effects on the flow and fluid forces on a single cylinder in cross flow,” *J. Fluids Struct*. **1**, 337.

Norberg, C., 1987b. “Effects of Reynolds number and a low-intensity freestream turbulence on the flow around a circular cylinder,” *Chalmers Univ. Technol. Publ*. **87**, 412.

Norberg, C., 2001. “Flow around a circular cylinder: Aspects of fluctuating lift,” *J. Fluids Struct*. **15**, 459.

Norberg, C., 2003. “Fluctuating lift on a circular cylinder: Review and new measurements,” *J. Fluids Struct*. **17**, 57.

Ozono, S., 1999. ”Flow control of vortex shedding by a short splitter plate asymmetrically arranged downstream of a cylinder,” *Phys Fluids* **11**, 2928.

Park, D. S., Ladd, D. M., Hendricks, E. W., 1994. ”Feedback control of von Karman vor- tex shedding behind a circular cylinder at low Reynolds numbers,” *Phys. Fluids* **6**, 2390.

Petrusma, M. S., Gai, S. L., 1994. ”The effect of geometry on the base pressure recoveryof the segmented blunt trailing edge,” *Aeronaut. J.* **98**, 267.

Poncet, P., 2002. ”Vanishing of mode B in the wake behind a rotationally oscillating circular cylinder,” *Phys. Fluids* **14**, 2021.

Poncet, P., 2004. ”Topological aspects of three-dimensional wakes behind rotary oscillating cylinders,” *J. Fluid Mech.* **517**, 27.

Protas, B., Styczek, A., 2002. ”Optimal rotary control of the cylinder wake in the laminar regime,” *Phys. Fluids* **14**, 2073.

Protas, B., 2004. ”Linear feedback stabilization of laminar vortex shedding based on a point vortex model,” *Phys. Fluids* **16**, 4473.

Rodriguez, O., 1991. ”Base drag reduction by the control of three-dimensional unsteady vortical structures,” *Exp. Fluids* **11**, 218.

Roshko, A., 1955. ”On the wake and drag of bluff bodies,” *J. Aeronaut. Sci.* **22**, 124.

Roussopoulos, K., 1993. ”Feedback control of vortex shedding at low Reynolds numbers,” *J. Fluid Mech* **248**, 267.

Sakamoto, H., Haniu, H., 1994. ”Optimum suppression of fluid forces acting on a circular cylinder,” *J. Fluids Struct.* **116**, 221.

Sevilla, A., Martinez-Bazán, C., 2004. ”Vortex shedding in high Reynolds number ax- isymmetric bluff-body wakes,” *Phys. Fluids* **16**, 3460.

Schewe, G., 1983. “On the force fluctuations acting on a circular cylinder in crossflow from subcritical up to transcritical Reynolds numbers,” *J. Fluid. Mech*. **133**, 265.

Shiels, D., Leonard, A., 2001. ”Investigation of a drag reduction on a circular cylinder in rotary oscillation,” *J. Fluid Mech.* **43**, 297.

Shih, W. C. L., Wang, C., Coles, D., Roshko, A., 1993. ”Experiments on flow past rough circular cylinders at large Reynolds numbers,” *J. Wind Eng. Ind. Aero-Dyn.* **49**, 351.

Siegel, S., Cohen, K., McLaughlin, T., 2006. ”Numerical simulations of a feedback-controlled circular cylinder wake,” *AIAA J.* **44**, 1266.

Strykowski, P. J., Sreenivasan, K. R., 1990. ”On the formation and suppression of vortex “ shedding ” at low Reynolds numbers,” *J. Fluids Struct.* **218**, 71.

Sueki, K., Takaishi, T., Ikeda, M., 2010. “Application of porous material to reduce aerodynamic sound from bluff bodies,” *Fluid Dyn. Res*. **42**, 015004 (14pp).

Smagorinsky, J., 1963. “General circulation experiments with the primitive equations,” *Monthly Weather Rev*. **91**, 99.

Spalart, P. R., Moser, R. D., Rogers, M. M., 1991. “Spectral methods for the Navier-Stokes equations with one infinite and two periodic directions,” *J. Comput. Phys*. **96**, 297.

Tang. S., Aubry, N., 2000. ”Suppression of vortexx shedding inspired by a low-dimensional model,” *J. Fluids Struct.* **14**, 443.

Tanner, M., 1972. ”A method of reducing the base drag of wings with blunt trailing edges,” *Aeronaut. Q.* **23**, 15.

Tokumaru, P. T., Dimotakis, P. E., 1991. ”Rotary oscillatory control of a cylinder wake,” *J. Fluid Mech.* **224**, 77.

Tombazis, N., Bearman, P. W., 1997. ”A study of three-dimensional aspects of vortex shedding from a bluff body with a mild geometric disturbance,” *J. Fluid Mech.* **330**, 85.

Zdravkovich, M. M., 1981. ”Review and classification of various aerodynamic and hydrodynamic means for suppressing vortex shedding,” *J. Wind Emg. Ind. Aero-Dyn.* **7**, 145.

Zhang, M., Cheng, L., Zhou, Y., 2004. ”Closed-loop-controlled vortex shedding and vibration of a flexibly supported square cylinder under different schemes,” *Phys. Fluids* **16**, 1439.